

Interaction of nanoparticles with peristaltic transport of fluid



By

Mohsin Raza

11-FBAS/PHDMA/S-12



Department of Mathematics and Statistics

Faculty of Basic and Applied Sciences

International Islamic University,

Islamabad, Pakistan

2016

Handwritten mark

Accession No TH-16736

PhD
620.11
MOI

1. Nanofluids

Interaction of nanoparticles with peristaltic transport of fluid



By

Mohsin Raza

Supervised by

Dr. Rahmat Ellahi

&

Co Supervisor

Dr. Noreen Sher Akbar

Department of Mathematics and Statistics

Faculty of Basic and Applied Sciences

International Islamic University,

Islamabad, Pakistan

2016

Interaction of nanoparticles with peristaltic transport of fluid

By

Mohsin Raza

A Thesis

Submitted in the Partial Fulfillment of the

Requirements for the Degree of

DOCTOR OF PHILOSOPHY

IN

MATHEMATICS

Supervised by

Dr. Rahmat Ellahi

&

Co Supervisor

Dr. Noreen Sher Akbar

Department of Mathematics and Statistics

Faculty of Basic and Applied Sciences

International Islamic University,

Islamabad, Pakistan

2016

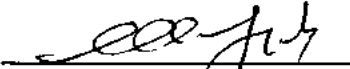
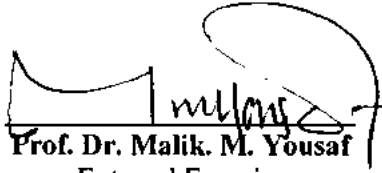



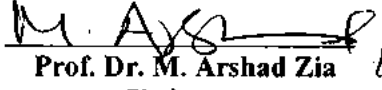
Certificate

Interaction of nanoparticles with peristaltic transport of fluid

By
Mohsin Raza

A THESIS SUBMITTED IN THE PARTIAL FULFILLMENT OF THE
REQUIREMENTS FOR THE DEGREE OF THE
DOCTOR OF PHILOSOPHY IN MATHEMATICS

We accept this thesis as conforming to the required standard

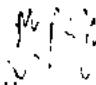
1. 
Prof. Dr. Muhammad Ayub
External Examiner
2. 
Prof. Dr. Malik. M. Yousaf
External Examiner
3. 
Prof. Dr. M. Sajid, TI
Internal Examiner
4. 
Dr. Rahmat Ellahi
Supervisor
5. 
Dr. Noreen Sher Akbar
Co-Supervisor
6. 
Prof. Dr. M. Arshad Zia
Chairman

Department of Mathematics and Statistics
Faculty of Basic and Applied Sciences
International Islamic University, Islamabad
Pakistan
2016

Declaration

Hereby I declare and affirm that this research work neither as whole nor as a part has been copied out from any source. It is further declaring that I have developed this research work entirely on the basis of my personal efforts. If any part of this thesis is proven to be copied out of some other, I shall stand by the consequences.

Moreover, no portion of the work presented in this thesis has been submitted to obtain other degree or qualification in this other university or institute of learning.

Signature: -----

Mohsin Raza

PhD Scholar
(Mathematics)

Dedication

This thesis is dedicated to my father

Mr. Muhammad Boota (Late)

&

my mother

Mrs. Shehnaz Akhtar

Acknowledgements

I thank Almighty Allah for providing me courage, strength and brain to complete my thesis. It is really all his blessings and nothing else.

I acknowledge with deep reverence and sincerity and feel much pleasure in expressing my heartiest gratitude to my respected supervisor **Dr. Rahmat Ellahi** for his dynamic and affectionate supervision whose inspiring attitude made it very easy to undertake this research. His kind advice and polite behavior encouraged and motivated me to finally complete my work. He has been a source of motivation and encouragement to me during this research.

I would like to thank to my co-supervisor **Dr. Noreen Sher Akber**, who extended her scholarly guidance and valuable support throughout the course of the thesis. She supported me with her knowledge and learning, I am indebted to her help and guidance throughout the research process.

I would like to thank my friends Mr. Mohsan Hassan and Captain Adil Butt who remained there to assist me and to help me during my studies in all respects. I would also mention my two sincere friends Mr. Iftikhar Ahmad and Dr. Asad Zaighum who have constantly been asking me one question “haven’t you done yet?” and affectionately mentioned me as their friend the “professional student”. Thank you both for your encouragement, support and most of all your humor. You both kept things light and keep me smiling.

I pay my special thanks to my parents and my other family members for being always there on my side and for praying my success and records. I am also very thankful to Higher Education Commission Pakistan, for providing me a scholarship under Indigenous 5000 Ph.D Fellowship Program without which it would not be possible for me to complete my higher studies.

Mohsin Raza

Preface

It is well recognized that the peristaltic motion is the basis of peristaltic pumps that move fluids through tubes without direct contact with pump components. The complicated relationship occurs in peristaltic when the effects of nanoparticles along with heat and mass transfer are considered simultaneously. The courtesy in exploring the interaction of different nanoparticles in peristaltic transport is a motivating factor for this thesis. In fact we intend to strengthen our efforts to understand the problems having more complicated nature, especially in the modeling of peristaltic flows of viscous fluids contain different nanomaterial such as carbon tubes, metal oxides and metal base nanoparticles with different sizes of particles under Brownian motion effects in diverse geometries. The basic equations governing the flow are first modelled and then reduced to a set of ordinary differential equation by using appropriate transformation for variables under the well-established long wavelength and low Reynolds number approximations. The solutions of non-dimensional liner equations are presented exactly whereas the nonlinear partial differential equations are solved by homotopy analysis method. The physical interpretations of sundry parameters such as Hartmann number, Grashof number, local and magnetic Reynolds numbers, Stommer's number, heat generation parameter, heat flux parameter, porosity parameter, Brickman number, nanoparticle volume fraction, thermal and viscous slip parameters for pressure rise, pressure gradient, velocity profile, temperature profile, axial induced magnetic field and current density are illustrated in graphical and tabular forms. In addition, irreversible process is graphical presented in term of entropy generation as well as Bejan number. The effect of various physical parameters on important trapping phenomenon is also shown in the form of streamlines. It is observed that different nanoparticles play significant role in peristaltic. The results show that, in the presence of small concentration, the effects of physical parameters such as MHD, porosity and slip for pressure gradient, pressure rise, velocity and temperature profiles are qualitatively larger than that of zero concentration.

This thesis contain seven chapters. First chapter provides some essential definitions, governing equations and methodology used in the subsequent chapters. The detailed description of each chapter is given in motivation, the subsection of introduction.

Contents

1	Introduction.....	1
1.1	Motivation.....	1
1.2	Analytical models for physical properties of nanofluid.....	9
1.2.1	Density of nanofluid.....	9
1.2.2	Heat capacity of nanofluid.....	9
1.2.3	Thermal expansion coefficient of nanofluid.....	10
1.2.4	Viscosity and thermal conductivity of nanofluid.....	10
1.3	Governing equations.....	16
1.3.1	Conservation of mass.....	16
1.3.2	Conservation of momentum.....	17
1.3.3	Conservation of energy.....	18
1.3.3	Induction equation.....	18
1.5	Methods of solutions.....	19
1.5.1	HAM Bpvh2 package.....	19
2	Influence of heat generation and heat flux in peristalsis with interaction of nanoparticles.....	20
2.1	Mathematical formulation.....	20
2.2	Solution of the problem.....	24
2.3	Results and discussion.....	27
2.4	Concluding remarks.....	42
3	Porosity effect in peristalsis flow of nanofluid with entropy generation.....	43
3.1	Mathematical formulation.....	43
3.2	Solution of the problem.....	45
3.3	Results and discussion.....	45
3.4	Concluding remarks.....	58
4	Interaction of nanoparticles for the peristaltic flow in an asymmetric channel with the induced magnetic field.....	59
4.1	Mathematical formulation.....	59
4.2	Solution of the problem.....	60
4.3	Results and discussion.....	65

4.4	Concluding remarks	81
5	Influence of induced magnetic field and heat flux with the suspension of carbon nanotubes for the peristaltic flow in a permeable channel	82
5.1	Mathematical formulation	82
5.2	Solution of the problem.....	84
5.3	Results and discussion.....	85
5.4	Concluding remarks	101
6	Anti-Bacterial applications for new thermal conductivity model in arteries with CNT suspended nanofluid.....	102
6.1	Mathematical formulation	102
6.2	Solution of the problem.....	104
6.3	Results and discussion.....	104
6.4	Concluding remarks	114
7	Endoscopic effects with entropy generation analysis in peristalsis for the thermal conductivity of H₂O+Cu nanofluid	115
7.1	Mathematical formulation	115
7.2	Solution of the problem.....	117
7.3	Results and discussion.....	118
7.4	Concluding remarks	131
	References.....	132
	Nomenclature.....	139

Chapter 1

Introduction

1.1 Motivation

A mechanism of fluid flow by means of moving contraction on the tubes/channels walls is called peristaltic. The mechanism of peristaltic phenomenon has been utilized for industrial applications like sanitary fluid transport, chemical processing, mining, paint and coating dairy processing. Also, peristaltic transport occurs in biomechanical apparatus such as roller and finger pumps. Complete understanding of peristaltic flows with various geometries demands the basic concepts of mechanics of fluid. Fluids we deal within our daily life can be broadly known in literature as viscous fluid. Typically, a gear, lobe, vane, screw, peristaltic or progressive cavity pump is ideal for viscous fluid applications. Thus, it is widely exploited in industrial peristaltic pumping. This mechanism is mainly used in the mechanical roller pumps using viscous fluids in the printing industry and for transporting blood in heart lung machine. Probably, Latham [1] was the first who investigated the mechanism of peristalsis in relation to mechanical pumping. Initial studies of peristaltic transport for Newtonian fluids were conducted by Shapiro et al. [2] in wave frame and then by Fung and Yih [3] in laboratory frame. Radhakrishnamacharya [4] studied the peristaltic flow of a power-law fluid in a channel under long wavelength approximation. Mishra and Ramachandra [5] reported the peristaltic flow in asymmetric channels with asymmetry generated by different amplitudes of the peristaltic waves in addition to different phases.

Recently, the concept of nanofluid has been expressed as a way for increasing the concert of the heat transfer rates in the liquids. With the prompt development of modern nanotechnology particles of nanometre-size (normally less than 100 nm) are used rather than of micrometer-size for colloidal suspensions in base fluid such as water etc. The term nanofluid was first introduced by Choi [6] in 1995 and since then it has gained lots of popularity among the researchers. The materials with nanometers sizes also possess unique physical and chemical properties. Without clogging they can flow smoothly through micro channels since they are very small, consequently they behave

like molecules of liquid [7]. As a matter of fact, it has grabbed more research into the investigation of the heat transfer characteristics in nanofluids. It was found that in the presence of nanoparticles within the fluid can appreciably increase the effective thermal conductivity of the fluid which ultimately increases the heat transfer characteristics. Some superb articles in this area are presented in [8].

Making the fluid slip along the wall, the fluid losses some adhesion at the wetted wall. Tretheway and Meinhart [9] have experimentally shown slip-flows. The slip condition plays an important role in shear skin, spurt, and hysteresis effects. The boundary conditions relevant to flowing fluids are very important in predicting fluid flows in many applications. The fluids that exhibit boundary slip have important technological applications such as in polishing valves of artificial heart and internal cavities [10]. In 2003, Choi et al. [11] examined apparent slip flows in hydrophilic and hydrophobic micro channels. Lauga and Cossu [12] have analyzed the stability of slip channel flow. The slip effects on the peristaltic flow of a non-Newtonian Maxwellian fluid have been investigated by Eldesoky [13]. Moreover, flow through a porous medium has several practical applications, especially in geophysical fluid dynamics. Examples of natural porous media are beach sand, sandstone, limestone, the human lung, bile duct, gall bladder with stones in small blood vessels. The influence of slip condition on peristaltic transport of a compressible Maxwell fluid through porous medium in a tube has been studied by Chu and Fang [14]. Comprehensive literature studies on porous media can be seen in the latest books [15 – 18].

Furthermore the magnetohydrodynamic character of fluid has a significant role in solidification processes of metal alloys and metal, study of nuclear fuel debris, control of underground spreading of chemical wastes and pollution, design of MHD power generators, blood pump machines and treatment of cancer tumor etc. Srinivas et al. [19] studied the influence of both heat transfer and wall slip conditions on the peristaltic flow of MHD Newtonian fluid in a porous channel with elastic wall properties. Mekheimer and Al-Arabi [20] found the nonlinear peristaltic transport of MHD flow through a porous medium in non-uniform channels. Further analysis could be seen through [21 – 23].

In view of all above, chapter two aims to examine the peristaltic flow with three different nanoparticles having the base fluid water with slip boundary condition through

a vertical asymmetric porous channel in the presence of MHD. The selected nanoparticles are titanium dioxide (TiO_2), copper oxide (CuO) and silicon dioxide (SiO_2). We have also considered thermal conductivity model with Brownian motion for nanofluids. This gains the effects of particle size, particle volume fraction and temperature dependence. The analysis is performed under the well-established long wavelength and low Reynolds number approximations. The exact solutions for the stream function, temperature and pressure gradient are given. All the physical features of the problems have been described with the help of graphs. **The results of this chapter (two) are published in the European Physical Journal Plus, 129 (2014) 185.**

Many researchers have investigated the heat transfer performance and flow characteristics of various nanofluids with different nanoparticles and base fluid materials. The thermal and physical properties of nanofluids were calculated using the Brinkman equation [24] for viscosity, the Xuan and Roetzel equation [25] for specific heat and the Hamilton and Crosser model [26] for thermal conductivity. The results showed that the presence of nanoparticles creates greater energy absorption than pure water at a low flow rate and that there is no contribution from heat absorption when the flow rate is high.

A change in the thermodynamic state of a system and all of its surroundings cannot be precisely restored to its initial state by infinitesimal changes in some property of the system without expenditure of energy. A system that undergoes an irreversible process may still be capable of returning to its initial state. However, the impossibility occurs in restoring the environment to its own initial conditions. The entropy generation is associated with the thermodynamic irreversibility taking place in the system. Consequently, thermodynamic irreversibility can be quantified through entropy calculations. Some important irreversible processes are heat flow through a thermal resistance, fluid flow through a flow resistance such as in the Joule expansion or the Joule-Thomson effect, diffusion, chemical reactions, Joule heating, friction between solid surfaces and fluid viscosity within a system. Many biological processes that were once thought to be reversible have been found to actually be a pairing of two irreversible processes whereas a single enzyme was once believed to catalyze both the forward and reverse chemical changes. It is found that two separate enzymes of similar structure are

typically needed to perform what results in a pair of thermodynamically irreversible processes. Bejan [27] presented the mechanisms involving with the entropy generation in applied thermal engineering. Bejan [28] introduced the concept of entropy generation and minimization in thermal systems. Very recently Ellahi et al. [29] studied the shape effects of nano size particles in $Cu-H_2O$ nanofluid on entropy generation, they found that increase percentage in friction of nanoparticles leads to increase in entropy generation rate.

With the above discussion in mind, chapter three investigated the effect of peristaltic flow with entropy generation and heat conducting nanofluids in the presence of porous medium in an asymmetric vertical channel. Suitable transformation is employed to achieve the system of ordinary differential equation. Arising nonlinear problems are solved analytically for the stream function, temperature and pressure gradient by mean of HAM base Bvph2 package. Characteristics of various pertinent parameters on the velocity, temperature, pressure rise, pressure gradient, entropy generation and Bejan number are examined and have been described with the help of graphs. This study (chapter three) is accepted for publication in **Journal of Porous Media (2016)**.

The study of MHD flow of electrically conducting fluids on peristaltic motion has become a subject of growing interest for researchers and clinicians. This is due to the fact that such studies are useful particularly for pumping of blood and magnetic resonance imaging (MRI). Theoretical work of Agarwal and Anwaruddin [30] explored the effect of magnetic field on the flow of blood in atherosclerotic vessels of blood pump during cardiac operations. Li et al. [31] observed that an impulsive magnetic field can be used for a therapeutic treatment of patients who have stone fragments in their urinary tract. Elshahed and Harun [32] made an observation on the peristaltic transport of Johnson -Segalman fluid by means of an infinite train of sinusoidal waves in a flexible channel under the effect of a magnetic field. However, all of these three studies have neglected the effect of induced magnetic field. Vishnyakov and Pavlov [33] are the first who considered the effect of induced magnetic field on peristaltic flow of an electrically conducting Newtonian fluid. Lately, Makheimer [34, 35] carried out the study of peristaltic transport of an incompressible conducting micropolar fluid in a symmetric channel and another for a couple stress fluid by considering the effect of induced magnetic field.

In view of all the aforesaid observations, the present analytical study has been designed

in such a manner that it can explore variation of information to study the effect of induced magnetic field on peristaltic flow of a viscous fluid in an asymmetric channel. The peristaltic wave train on the channel wall has been considered to have different amplitudes and phase difference. The theme of chapter four is to describe the effect of induced magnetic field and heat generation on peristaltic flow of water and Cu-water nanofluid in an asymmetric channel. At the same time, an exact solution of dimensionless governing equations for water and Cu-water nanofluid will be suggested. The effect on different parameters on both fluids is presented in form of graphs. Thus, the results presented here will find an important clinical application such as in magnetic resonance imaging (MRI) as well as in the gastrointestinal tract and small blood vessels. This analysis (chapter four) is published in **European Physical Journal Plus, 129 (2014) 155.**

Fluid movements in a channel of varying gap with permeable walls covered by a layer of porous material is discussed in next chapter. The motivation of this investigation comes from the study of abnormal flow in the arterial system caused by the presence of occlusion or stenosis. At various locations in the arterial system, stenosis may develop due to abnormal intravascular growth [36]. It may also be due to the abnormal accumulation of fluid in the tissue bounding the artery. Arteries may also be narrowed by the development of atherosclerotic plaques which are closely connected with the blood flow through the artery bounded by a thin layer of tissue, idealized into a porous medium, which separates the blood flow from the flow of other physiological fluids (is called PF). The stenosis developed in the artery causing the abnormal flow is an important factor in the development and progression of arterial diseases. Thus, the subject area of movement and accumulation of PF in the tissue and their result on blood flow in the artery is an important problem because the flow features in the locality of the resulting protuberance may significantly be altered. The results of the present study throw light on the understanding of the important flow characteristics in the arterial system, namely, the pressure, shear stress and possible changes in them. These in turn are related, respectively, to the physiologically important problems involving (i) increase in resistance to the blood flow, (ii) possible damages to the red and endothelial cells due to the existence of high shear zones, and (iii) possible transition from a laminar to turbulent flow inside the blood vessel creating high intensity shear zones unfavorable to the blood flow and arterial wall. The flow in a channel of varying gap bounded by

rigid walls has been investigated by many authors [37 – 40]. The results obtained from these analyses using rigid boundaries are not of much use in understanding the characteristics of flow in arteries, because they are bounded by tissues which are idealized into a porous medium where one has to use a slip condition at the bounding surface similar to the one postulated by Beavers and Joseph [41] (hereafter called BJ condition). Hence, it requires to investigate flow in two dimensional channel of varying gap bounded on both sides by a porous layer.

Carbon nanotubes (CNTs) were discovered by Iijima and Baughman [42, 43]. They showed exceptional strength and distinguished electrical properties, and are efficient conductors of heat. Their figure is deduced from their size, as the diameter of a nanotube is on the orderliness of a few nanometers (about 50,000 times smaller than the breadth of a human hair), whereas they may be higher to several millimeters in length. Nanotubes are of two principal kinds: single-walled nanotubes (SWNTs) and multi-walled nanotubes (MWNTs). The single CNT, which is one or multiple layers of graphene sheets which roll up. SWCNTs' diameter is close to 1 nm with a varied length from nanometer to centimeters whereas the interlayer of distance for MWCNTs is approximately 0.34 nm [44]. Owing to CNTs' extraordinary thermo conductivity, electro conductivity and mechanical property, CNTs find their applications in the form of additives in structural materials such like golf stub, boat, aircraft, bicycles etc. By mixing it in the solid [45 – 48] or fluid [49 – 52], the mixture can effectively enhance the thermal performance and mechanical properties of the base materials. So, the CNTs employed in the field are examined with great potential for the heat transfer applications. Choi and co-workers conducted initial observation of thermal conductivity increase using cylindrical structures, namely multi-walled nanotubes (MWCNT) [53]. The outstanding properties of carbon nanotubes (CNTs) help in biological engineering applications. CNTs can be used to tune cellular fate through both extracellular pathway and intracellular pathway. CNT based biomaterials are applied into bone, nerves, and cardiovascular system. There has also been improvement in the use of CNTs in controlling cellular alignment, to increase tissue regeneration, growth factor delivery and gene delivery.

Motivated by above discussion, chapter five addresses the peristaltic flow in a symmetric channel with permeable wall. The effect of induced magnetic field, heat generation and heat flux on peristaltic flow of water and CNTs nanofluid is also

analyzed. An exact solution of dimensionless governing equations for water and CNTs nanofluid is obtained and role of physical parameters is discussed through graphs. Content of this chapter (chapter five) is published in the **Journal of Magnetism and Magnetic Materials**, 381 (2015) 405 – 415.

It is well recognized that the peristaltic motion is now an important research subject due to its vast applications in physiology. This type of rhythmic contraction is the basis of peristaltic pumps that move fluids through tubes without direct contact with pump components. A peristaltic pump is a type of positive displacement pump used for pumping a variation of fluids. The fluid is contained within a flexible tube fitted inside a circular pump casing. A rotor with a number of "rollers", "shoes", "wipers", or "lobes" attached to the external circumference of the rotor compresses the flexible tube. As the rotor turns, the part of the tube under compression is pinched closed (or "occludes") thus forcing the fluid to be pumped to move through the tube. Additionally, as the tube opens to its natural state after the passing of the cam ("restitution" or "resilience") fluid flow is induced to the pump. Peristaltic pumps are typically used to pump clean/sterile or aggressive fluids because cross contamination with exposed pump components cannot occur. Some common applications include pumping IV fluids through an infusion device, aggressive chemicals, high solids slurries and other materials where isolation of the product from the environment and the environment from the product, is critical. It is also used in heart-lung machines to circulate blood during a bypass surgery as the pump does not cause significant hemolysis. Their unique design makes them especially suitable to pumping abrasives and viscous fluids.

Heat transfer in cooling processes is quite popular area of industrial research. Conventional methods for increasing cooling rates include the extended surfaces such as fins and enhancing flow rates. These conventional methods have their own limitations such as undesirable increase in the thermal management system's size and increasing pumping power respectively. The thermal conductivity characteristics of ordinary heat transfer fluids like oil, water and ethylene glycol mixture are not adequate to meet today's requirements. The thermal conductivity of these fluids has key role in heat transfer coefficient between the heat transfer medium and heat transfer surface. Many techniques have been proposed for improvement in thermal conductivity of ordinary fluids, one of them is suspending nanoparticles in liquids.

By motivation of said applications of peristaltic flow in tube chapter six looks at the peristaltic transport of SWCNT and MWCNT containing nanofluid in permeable tube. The related partial differential system is reduced first into ordinary differential equation and then the exact solutions for the stream function, temperature and pressure gradient are successfully obtained. Influence of various physical parameters on velocity, temperature, pressure gradient and pressure rise is scrutinized graphically. The investigation of this chapter (chapter six) is accepted for publication in the **Journal of Mechanics in Medicine and Biology 16 (2016) 1 – 14**.

The flow of bio-fluids such as urine through ureters, passage of chyme in intestines, swallowing of food bolus in esophagus, blood flow through blood vessels takes place due to the propagation of electrochemically generated waves along the vessels containing fluids. Biomechanical pumps have been fabricated deriving ideas from this peristaltic mechanism that preserves the purity of the contents from machinery parts such as piston during operation. Recently, several mechanical pumps are prepared on the basis of peristalsis to save energy. These types of pumps play an important role in engineering. An endoscopic effect on peristaltic motion of a fluid is very important for medical diagnosis and it has many clinical applications. Now the endoscope is a very important tool used for determining real reasons responsible for many problems in the human organs in which the fluid is transported by peristaltic pumping such as, stomach and small intestine, etc.

Biomagnetic fluid dynamics is a relatively new area that deals with the fluid dynamics of MHD biological fluids. During the last few decades, extensive literature is available on the MHD flows of biological fluids. Such flows have numerous applications in bioengineering and medical sciences, specifically, magnetic wound or cancer tumor treatment causing magnetic hyperthermia, bleeding reduction during surgeries and targeted transport of drugs using magnetic particles as drug carriers are few such examples. In fact, a biomagnetic fluid exists in a living creature and its flow is affected through a magnetic field. Blood is a biomagnetic fluid. It behaves as a magnetic fluid due to the complex interaction of the intercellular protein, cell membrane and the hemoglobin. It is also known that blood possesses the property of diamagnetic material when oxygenated and paramagnetic when deoxygenated.

With the importance of above discussion in mind, the fluid mechanics effects of peristaltic transport in a gap between two coaxial tubes, filled with nanofluid are proposed in this chapter seven. The inner tube is rigid and the outer one has wave trains moving independently under the effect of MHD. The exact solutions for the stream function, temperature and pressure gradient are given. All physical features of the problems have been described with the help of graphs. The outcomes of this chapter (chapter seven) are published in **Journal of Applied Fluid Mechanics 9 (2016) 1721 – 1730**.

1.2 Analytical models for physical properties of nanofluids

1.2.1 Density of nanofluid

The density of nanofluid is based on the physical principle of the mixture rule. As such it can be represented as

$$\rho_{nf} = \left(\frac{M^*}{V^*} \right)_{nf} = \frac{M_f^* + M_s^*}{V_f^* + V_s^*} = \frac{\rho_f V_f^* + \rho_s V_s^*}{V_f^* + V_s^*}, \quad (1.1)$$

$$\rho_{nf} = \left(1 - \frac{V_s^*}{V_f^* + V_s^*} \right) \rho_f + \left(\frac{V_s^*}{V_f^* + V_s^*} \right) \rho_s, \quad (1.2)$$

$$\rho_{nf} = (1 - \phi) \rho_f + (\phi) \rho_s, \quad (1.3)$$

here M^* is mass and V^* is volume respectively. The f and s in subscripts respectively refer to the fluid and nanoparticle while ϕ is the volume fraction of the nanoparticles. To examine the validity of Eq. (1.3), Pak and Cho [54] and Ho et al. [55] conducted experimental studies to measure the density of Al_2O_3 -water nanofluids at room temperature as shows an excellent agreement between the experimental results and the predictions using Eq. (1.3).

1.2.2 Heat capacity of nanofluid

The specific heat of nanofluid can be determined by assuming thermal equilibrium between the nanoparticles and the base fluid phase as follows:

$$(\rho C_p)_{nf} = \rho_{nf} \frac{(M^* C_p)_f \Delta T + (M^* C_p)_s \Delta T}{(M_f^* + M_s^*) \Delta T}, \quad (1.4)$$

$$(\rho C_p)_{nf} = \rho_{nf} \frac{(M^* C_p)_f \Delta T + (M^* C_p)_s \Delta T}{(M_f^* + M_s^*) \Delta T}, \quad (1.5)$$

$$(\rho C_p)_{nf} = \rho_{nf} \frac{(V^* \rho C_p)_f + (V^* \rho C_p)_s}{\frac{(M_f^* + M_s^*)}{(V_f^* + V_s^*)} \times (V_f^* + V_s^*)}, \quad (1.6)$$

$$(\rho C_p)_{nf} = (1 - \phi)(\rho C_p)_f + \phi(\rho C_p)_s, \quad (1.7)$$

in which ρ_s is the density of the nanoparticle, ρ_f is the density of the base fluid, ρ_{nf} is the density of the nanofluid, $(C_p)_s$ is the heat capacity of the nanoparticle and $(C_p)_f$ is heat capacity of the base fluid. The nanofluid based on the models given in Eq. (1.7) decreases with an increase in the volume fraction of nanoparticles. The experimental results were compared with the predictions obtained from the models compares very well with the experimental data of Zhou and Ni [56].

1.2.3 Thermal expansion coefficient of nanofluid

The thermal expansion coefficient of nanofluids can be estimated utilizing the volume fraction of the nanoparticles on a weight basis as follows [57]:

$$(\rho \beta^*)_{nf} = (1 - \phi)(\rho \beta^*)_f + \phi(\rho \beta^*)_s, \quad (1.8)$$

where β_f^* and β_s^* are the thermal expansion coefficients of the base fluid and the nanoparticle, respectively.

1.2.4 Viscosity and thermal conductivity of nanofluid

The viscosity of nanofluid is of great significance as the application of nanofluids is always associated with their flow. A few studies have addressed the viscous properties of nanofluid [58–60]. In general, the viscosity of nanofluids is much higher than that of their base fluids. The viscosity is a strong function of temperature and the volumetric concentration. Furthermore, a particle-size effect seems to be important only for sufficiently high particle fractions. In 1956, Einstein [61] was determined the effective viscosity of a suspension of spherical solids as a function of volume fraction (volume

concentration lower than 5%) using the phenomenological hydrodynamic equations. This equation was expressed by

$$\mu_{nf} = (1 - 2.5\phi)\mu_f, \quad (1.9)$$

where μ_{nf} is the viscosity of the nanofluid and μ_f is the viscosity of the base fluid. Later, Einstein's equation was extended by Brinkman [62] to suspensions with moderate particle volume fraction, typically less than 4% as defined as:

$$\mu_{nf} = \frac{\mu_f}{(1 - \phi)^{2.5}}. \quad (1.10)$$

Considering the Brownian motion of nanoparticles and the interaction between a pair of particles, Batchelor [63] proposed the following equation.

$$\mu_{nf} = (1 - A_1^* \phi + A_2^* \phi^2 + \dots)\mu_f. \quad (1.11)$$

In Eq. (1.11), A_1^* is the intrinsic viscosity and A_2^* is the Huggins' coefficient, for spherical particles Batchelor considered the values of $A_1^* = 2.5$ and $A_2^* = 6.5$ respectively.

The thermal conductivities of different particles in liquid suspensions with spherical and non-spherical particles are of great interest in various engineering applications because of their high effective thermal conductivities over base liquids at very low particle volume concentrations of nanoparticles [64 – 67]. The simplest model based on the macroscopic effective medium theory was first developed by Maxwell for a dilute suspension of non-interacting spherical particles [68] as follow:

$$\frac{k_{nf}}{k_f} = \frac{k_s + 2k_f + 2(k_s - k_f)\phi}{k_s + 2k_f - (k_s - k_f)\phi}. \quad (1.12)$$

This model shows that the effective thermal conductivity of nanofluids depends on the thermal conductivities of the spherical particle, thermal conductivity of base fluid and the volume fraction of the solid particles. Further developments in non-spherical particle shapes with introducing a shape factor can be expressed as

$$\frac{k_{nf}}{k_f} = \frac{k_s + (n^* - 1)k_f - (n^* - 1)\phi(k_f - k_s)}{k_s + (n^* - 1)k_f + \phi(k_f - k_s)}, \quad (1.13)$$

in which k_s and k_f are the conductivities of the particle material and the base fluid. In

this Hamilton-Crosser model, $n^* = 3/\Psi$ is the empirical shape factor (Ψ) is the sphericity defined as a ratio between the surface area of the sphere and the surface area of the real particle with equal volumes). When one choose shape factor $n^* = 3$, then the Hamilton-Crosser model reduces to the Maxwell model for spherical particle mixtures.

It is observed that above mentioned literature properties of Eqs. (1.3), (1.7) and (1.8) are considered to be independent of the movement of nanoparticles. When a small size particles are adjoined in a fluid, they just behave like the impacts of gases or liquid molecules. For nanoparticles colloids with each other, the instantaneous momentum reported to the particle varies random which causes the particle to move on an erotic path which is known as Brownian motion. The Brownian motion is claimed to play an important role in modifying the thermal conductivity and viscosity of nanofluid. There are two ways form which the Brownian motion of nanoparticles enhance the thermal conduction firstly the direct contribution due to the motion of the nanoparticles that transport heat *i.e.*, solid – solid transport of heat from one to another secondly the indirect contribution due to nanoconvection of the fluid surrounding individual nanoparticles. Among the existing models that predict the thermal conductivity and viscosity of nanofluids with considering the Brownian motion, the models proposed by Koo and Kleinstreuer [69, 70] are utilized in the present thesis. These models have successfully been used by Ghasemi and Aminossadati [71] to study the effects of Brownian motion on laminar steady-state natural convection in a right triangular enclosure with localized heating on the vertical side. Note that these models were proposed based on water with copper oxide nanoparticles. Although the extension to other combinations of base liquids and nanoparticles may be justified. In these models, it is assumed that the thermal conductivity and viscosity of nanofluids consist of two parts. One is referred to as the static part (k_s, μ_s) that is evaluated by mixture models *i.e.*, the Maxwell model Eq. (1.12) for thermal conductivity and the Brinkman model Eq. (1.10) for viscosity, and the other part (k_B, μ_B) is attributed to the Brownian motion. The expression for predicting the effective thermal conductivity of nanofluids appears as

$$k_{nf} = k_f + k_B, \quad (1.14)$$

where k_f is given in Eq. (1.12) and k_B is expressed as

$$k_B = 5 \times 10^4 \gamma_1 \phi (\rho C_p)_f \sqrt{\frac{\tilde{k} T_{env}}{\rho_s d_s}} F^*(T_{env}, \phi), \quad (1.15)$$

here \tilde{k} is the Boltzmann constant, It has the dimension energy at the individual particle level divided by temperature and its accepted value in system international units is $\tilde{k} \approx 1.38 \times 10^{23}$ (joule per kelvin), d_s is the diameter of nanoparticles by assuming that these nanoparticles have a uniform size and are perfectly spherical *i.e.*, $d_s = 30$ nm, T_{env} is a environment temperature that is chosen as T_0 in the current study, γ_1 is a function of the volume fraction ϕ of nanoparticles, which is given by

$$\gamma_1 = \begin{cases} 0.137(100\phi)^{-0.8229} & \text{for } \phi < 0.01 \\ 0.0011(100\phi)^{-0.7272} & \text{for } \phi > 0.01 \end{cases} \quad (1.16)$$

and the function $F^*(T_{env}, \phi)$ is given by

$$F^*(T_{env}, \phi) = (-6.04\phi + 0.4705)T_{env} + (1722.3\phi - 134.63), \quad (1.17)$$

which is valid for $0.01 \leq \phi \leq 0.04$ and 300 (kelvin) $\leq T_{env} \leq 325$ (kelvin). It is important to note that $T_{env} = 300$ (kelvin) chosen for the present study for the expression of thermal conductivity, the thermal diffusivity of nanofluids is then defined by

$$\alpha_{nf} = \frac{k_{nf}}{(\rho C_p)_{nf}}. \quad (1.18)$$

Likewise the effective viscosity of nanofluids is

$$\mu_{nf} = \mu_c + \mu_B, \quad (1.19)$$

where μ_c is evaluated by Brinkman model Eq. (1.10) and μ_B is expressed as:

$$\mu_B = 5 \times 10^4 \gamma_1 \phi \rho_{nf} \sqrt{\frac{\tilde{k} T_{env}}{\rho_s d_s}} F^*(T_{env}, \phi). \quad (1.20)$$

The relation developed by Corcione [72] is based on existing experimental data available in the literature as:

$$\frac{\mu_{nf}}{\mu_f} = \frac{1}{1 - 34.87 \left(\frac{d_s}{d_f}\right)^{-0.3} (\phi)^{1.03}}, \quad (1.21)$$

where d_f is the equivalent diameter of a base fluid molecule, given by

$$d_f = 0.1 \left(\frac{6M^{**}}{N^{**} \pi \rho_{f0}} \right)^{1/3}, \quad (1.22)$$

in which M^{**} is the molecular weight of the base fluid, N^* is the Avogadro number ($\approx 6.023 \times 10^{23}$). For the thermal conductivity of the nanofluid, the following Chon et al. [73] model is chosen

$$\frac{k_{nf}}{k_f} = 1 + 64.7(\phi)^{0.746} \left(\frac{d_f}{d_s}\right)^{0.369} \left(\frac{k_s}{k_f}\right) (Pr^*)^{0.9955} (Re^*)^{1.2321}, \quad (1.23)$$

here d_f and d_s are diameter of the molecule of the base fluid and nanoparticles,

respectively. $Pr^* = \frac{\mu_f}{\rho_f \alpha_f}$ and $Re^* = \frac{\rho_f k_b T}{3\pi \mu_f^2 l_f}$ are respectively specific Prandtl

number and Reynolds number. For water l_f is the mean free path of the base fluid which has been considered equal to 0.17 nm.

Considering the effect of thermal dispersion

$$k_{eff} = k_{nf} + k_d, \quad (1.24)$$

where k_d is the thermal conductivity due to thermal dispersion and is obtained as

$$k_d = C^*(\rho C_p)_{nf} \sqrt{u^2 + v^2} + \phi d_p, \quad (1.25)$$

where C^* is an empirical constant obtained from experimental results [74]. Value of k_d is neglecting where comparing with the value of k_{nf} for the case under consideration.

The thermal conductive model for nanofluid proposed by Yu and Choi [75] is used for carbon nanotubes which is defined by

$$\frac{k_{nf}}{k_f} = \left(1 + \frac{m\phi A^*}{1 - \phi A^*}\right), \quad (1.26)$$

in Eq. (1.26) the parameter A^* is given by

$$A^* = \frac{1}{3} \sum_{j=a,b,c} \frac{k_{pj} - k_f}{k_{pj} + (n-1)k_f}, \quad (1.27)$$

where n is the empirical shape factor and k_{pj} thermal conductivities along the axes of the tubes which is reported by Bilboul [76]:

$$k_{pj} = \left[1 + \frac{k_p - k_s}{k_p \{rd(j,0) - d(j,t)\} - k_s \{rd(j,0) - d(j,t) - r\}}\right] k_s, \quad (1.28)$$

where $j(= \tilde{a}, \tilde{b} \text{ and } \tilde{c})$ is along the semiaxis directions of the carbon tube as shown in Fig. 1.1, k_p and k_s are the thermal conductivities of the solid ellipsoid and its surrounding layer respectively.

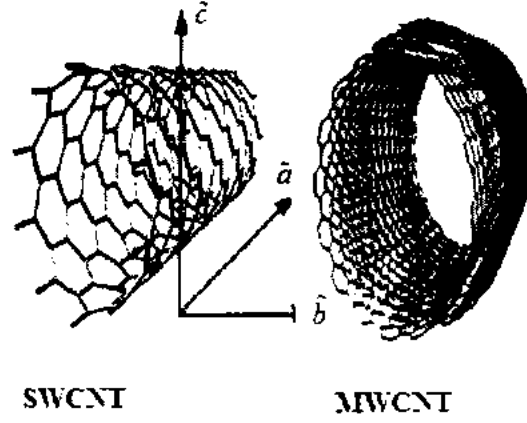


Fig. 1.1. Geometry for SWCNT and MWCNT.

The volume ratio r^* and $d(j, \nu)$ are depolarization factors defined by Landau et al. [77]:

$$r^* = \frac{\sqrt{(\tilde{a}^2 + t)(\tilde{b}^2 + t)(\tilde{c}^2 + t)}}{\tilde{a}\tilde{b}\tilde{c}}, \quad (1.29)$$

$$d(j, \nu) = \frac{\sqrt{(\tilde{a}^2 + \nu)(\tilde{b}^2 + \nu)(\tilde{c}^2 + \nu)}}{2} \times \int_0^\infty \frac{dw}{(j^2 + \nu + w)\sqrt{(\tilde{a}^2 + \nu + w)(\tilde{b}^2 + \nu + w)(\tilde{c}^2 + \nu + w)}}, \quad (1.30)$$

with $\nu = 0$ for outside of solid ellipsoid and $\nu = t$ for outside surface of its surrounding layer.

The effective viscosity models Yu and Choi for nanotube is given by

$$\mu_{nf} = \left(1 - \frac{\phi_a}{\phi_m}\right)^{-\eta^* \phi_m} \quad (1.31)$$

with

$$\eta^* = \frac{0.312r^*}{\ln 2r^* - 1.5} + 2 - \frac{0.5}{\ln 2r^* - 1.5} - \frac{1.872}{r^*} \quad (1.32)$$

and ϕ_a is effective volume fraction of nanoparticles written it as:

$$\phi_a = \phi \left(\frac{a_a}{a^*}\right)^{3-D}, \quad (1.33)$$

where a_a and a^* are the aggregate and primary nanoparticles radii respectively. D is the fractal index which depends on the type of aggregation, particle size and shape and

shear flow condition. Here we consider the radius 12.5 nm and length 25000 nm of single-wall and multi wall carbon nanotube. The thickness of nanolayer around tubes is considered 2 nm and thermal conductive of this layer is $2k_c$. For this assumption about nanotube, apply the carbon nanotubes suspensions in 15% mixture of salt in water, the parameters $\tilde{a} = 25000$ nm, $\tilde{b} = \tilde{c} = 12.5$ nm and the value of the parameter t is chosen to be 54 nm, which corresponds to a 2 nm layer thickness $\sqrt{12.5^2 + 54} - 12.5 = 2$ nm along \tilde{b} -axis and \tilde{c} -axis but a negligible layer thickness $\sqrt{25000^2 + 54} - 25000 = 0.001$ nm is taken along \tilde{a} -axis.

1.3 Governing equations

The fundamental equations of fluid dynamics are based on the following universal laws of conservation.

1.3.1 Conservation of mass

The equation that results from applying the conservation of mass law to a fluid flow is called the continuity equation and mathematically can be defined as

$$\frac{\partial \rho}{\partial t} + \nabla \cdot (\rho \mathbf{V}) = 0, \quad (1.34)$$

where \mathbf{V} is the fluid velocity. The first term in this equation represents the rate of increase of the density in the control volume and the second term represents the rate of mass flux passing out of the control surface (which surrounds the control volume) per unit volume. The Eq. (1.34) can be write in following form

$$\frac{D\rho}{Dt} + \rho \nabla \cdot \mathbf{V} = 0, \quad (1.35)$$

where

$$\frac{D(\)}{Dt} \equiv \frac{\partial(\)}{\partial t} + \mathbf{V} \cdot \nabla(\). \quad (1.36)$$

Eq. (1.34) was derived using the Eulerian approach. In this approach, a fixed control volume is utilized, and the changes to the fluid are recorded as the fluid passes through the control volume. In the alternative Lagrangian approach, the changes to the properties of a fluid element are recorded by an observer moving with the fluid element. The Eulerian viewpoint is commonly used in fluid mechanics. The Eq. (1.35) in Cartesian coordinate system is as follows

$$\frac{\partial \rho}{\partial t} + \frac{\partial}{\partial x}(\rho u) + \frac{\partial}{\partial y}(\rho v) + \frac{\partial}{\partial z}(\rho w) = 0, \quad (1.37)$$

where u, v, w represent components of the velocity vector. A flow in which the density of each fluid element remains constant is called incompressible. Mathematically, this implies that

$$\frac{D\rho}{Dt} = 0, \quad (1.38)$$

that reduces Eq. (1.34) to

$$\nabla \cdot \mathbf{V} = 0, \quad (1.39)$$

or in component form

$$\frac{\partial u}{\partial x} + \frac{\partial v}{\partial y} + \frac{\partial w}{\partial z} = 0. \quad (1.40)$$

1.3.2 Conservation of momentum

Equation for the conservation of linear momentum is also known as the Navier-Stokes equation. It is possible to write it in many different forms. One possibility is

$$\rho_{nf} \left[\frac{\partial \mathbf{V}}{\partial t} + (\mathbf{V} \cdot \nabla) \mathbf{V} \right] = \nabla \cdot \boldsymbol{\tau} + \mathbf{F}. \quad (1.41)$$

The stress tensor for Newtonian nanofluid is defined as

$$\boldsymbol{\tau} = -p\mathbf{I} + \mu_{nf} \mathbf{A}_1, \quad (1.42)$$

where \mathbf{A}_1 is first Rivlin Ericksen tensor.

The body force \mathbf{F} can be defined under the effects of MHD and porosity as follow

$$\mathbf{F} = -\frac{\mu_{nf}}{K_1} \mathbf{V} + \mathbf{J} \times \mathbf{B}, \quad (1.43)$$

where K_1 is the permeability of the medium having dimensions $(length)^2$ and \mathbf{J} is current density force which is the combination of electric and magnetic force on a point charge due to electromagnetic fields and defined as

$$\mathbf{J} = \sigma (\mathbf{E} + \mathbf{V} \times \mathbf{B}), \quad (1.44)$$

here \mathbf{B} is magnetic field, \mathbf{E} is electric field and σ is electrical conductivity.

1.3.3 Conservation of energy

Energy equation can be written in many different ways, such as the one given below

$$\rho C_p \left[\frac{\partial T}{\partial t} + (\mathbf{V} \cdot \nabla) T \right] = k \nabla^2 T + \Phi^*, \quad (1.45)$$

Eq. (1.47) is based on the following assumptions: (i) continuum, (ii) Newtonian fluid and (iii) negligible nuclear, electromagnetic and radiation energy transfer, if the effect of thermal radiation, heat generation and viscous dissipations are dominated then the Eq. (1.45) can be written in following form

$$(\rho C_p)_{eff} \left[\frac{\partial T}{\partial t} + (\mathbf{V} \cdot \nabla) T \right] = \nabla^2 \left(k_{eff} T + \frac{4\sigma^*}{3k^*} (T^4 - T_m^4) \right) + Q(T - T_m) + \Phi^*, \quad (1.46)$$

here Φ^* is the dissipation function representing the work done against viscous force and is defined by

$$\Phi^* = 2\mu_{eff} \left[\left(\frac{\partial u}{\partial x} \right)^2 + \left(\frac{\partial v}{\partial y} \right)^2 \right] + \left(\frac{\partial u}{\partial y} + \frac{\partial v}{\partial x} \right)^2. \quad (1.47)$$

1.3.4 Induction equation

Induction equation is one of the magnetohydrodynamics equations, is a partial differential equation with spatial and time variables that relates the magnetic and velocity fields of an electrically conductive fluid such as a plasma. This equation can be derived using the Maxwell's equations along with the Ohm's law.

Maxwell's equations can be described by the following expressions.

Solenoidal nature of magnetic field \mathbf{B}

$$\nabla \cdot \mathbf{B} = 0. \quad (1.48)$$

$$\mathbf{B} = \mu_e \mathbf{H}. \quad (1.49)$$

Faraday's law

$$\nabla \times \mathbf{E} = -\mu_e \frac{\partial \mathbf{H}}{\partial t}. \quad (1.50)$$

Ampere equation

$$\nabla \times \mathbf{H} = \mathbf{J}. \quad (1.51)$$

Charge conservation

$$\nabla \cdot \mathbf{J} = 0. \quad (1.52)$$

Using the Eqs. (1.44), (1.49) – (1.52), we obtain the induction equation.

$$\frac{\partial \mathbf{H}}{\partial t} = \nabla \times (\mathbf{V} \times \mathbf{H}) + \frac{1}{\xi} \nabla^2 \mathbf{H}, \quad (1.53)$$

where $\xi = \sigma \mu_0$ is the magnetic diffusivity.

1.5 Methods of solutions

The nonlinear differential equations, along with nonlinear boundary conditions the coupled differential equations have rare chance of getting exact solutions or even semi analytical solutions that is why some numerical techniques have been developed.

1.5.1 HAM Bvph2 package

In 2013, Liao [78] developed a homotopy analysis method based package “Bvh2” that can deal with many systems of ordinary differential equations. It can solve different kinds of systems of ODEs, including a system of coupled ODEs in finite interval, a system of coupled ODEs in semi-infinite interval, a system of coupled ODEs with algebraic property at infinity, a system of ODEs with an unknown parameter to be determined and a system of ODEs in different intervals. For simplicity, the BVPh 2.0 needs to input the governing equations along with corresponding boundary conditions and choose proper initial guess of solutions and auxiliary linear operators for under consideration linear sub-problems. In this package, one has great freedom to choose the auxiliary linear operator and initial guess. To run the package, need to define all the inputs of problem properly, except the convergence-control parameters. Usually, the optimal values of the convergence-control parameters are obtained by minimizing the squared residual error.

Chapter 2

Influence of heat generation and heat flux in peristalsis with interaction of nanoparticles

In this chapter, the peristaltic flow of three distinctive nanoparticles with water as base fluid under influence of MHD and slip boundary condition through a vertical asymmetric porous channel is analyzed. The titanium dioxide(TiO_2), copper oxide (CuO) and silicon dioxide (SiO_2) nanoparticles are taken into account. For the nanofluid, the thermal physical properties models are taken under the impacts of molecule size, molecule volume fraction and temperature dependence. The basic governing equations are reduced to non – dimensional form by using appropriate transformation and long wavelength approximation. Exact solutions are acquired from the subsequent equations. The acquired expressions for pressure gradient, temperature and velocity profile are depicted through graphs for different relevant parameters. The streamlines are drawn for some physical quantities to discuss trapping phenomenon.

2.1 Mathematical formulation

Here considers an incompressible peristaltic flow of nanofluid in an irregular channel with channel width $d_1 + d_2$. Asymmetry in the flow is because of propagation of peristaltic waves of different amplitudes and phases on the channel walls. The fluid occupying the porous space in the channel wave propagating beside the walls of the channel with continuous speed c_1 .

$$Y = H_1 = d_1 + a_1 \cos\left(\frac{2\pi}{\lambda}(X - c_1 t)\right), \quad (2.1)$$

$$Y = H_2 = -d_2 - b_1 \cos\left(\frac{2\pi}{\lambda}(X - c_1 t) + \omega\right). \quad (2.2)$$

In the above equations a_1 and b_1 denote the waves amplitudes, λ is the wave length, c_1 is the wave speed, t is the time, X is the direction of wave propagation and Y is perpendicular to X . ω ($0 \leq \omega \leq \pi$) is the phase difference. It should be noted that $\omega =$

0 corresponds to symmetric channel with waves in phase, $\omega = \pi$, the waves are out of phase and the condition $a_1^2 + b_1^2 + 2a_1b_1\cos(\omega) \leq (d_1 + d_2)^2$ holds. Further in Cartesian coordinate system, X is taken in the direction of wave propagation and Y in the direction normal to the mean position of the channel walls. The geometry of the walls is visualized in Fig. 2.1.

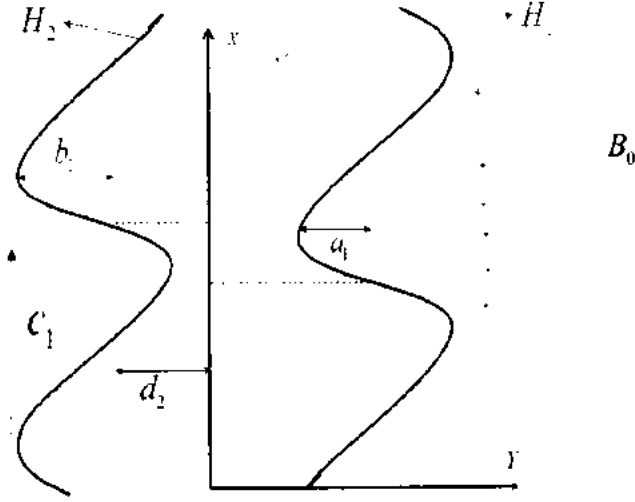


Fig. 2.1: Geometry of the problem.

In the presence of MHD and porosity, the governing Eqs. (1.39), (1.41) and (1.45) in component notation are

$$\frac{\partial U}{\partial X} + \frac{\partial V}{\partial Y} = 0, \quad (2.3)$$

$$\rho_{nf} \left(\frac{\partial U}{\partial t} + U \frac{\partial U}{\partial X} + V \frac{\partial U}{\partial Y} \right) = -\frac{\partial P}{\partial X} + \mu_{nf} \left(\frac{\partial^2 U}{\partial X^2} + \frac{\partial^2 U}{\partial Y^2} \right) - \frac{\mu_{nf}}{K_1} U - \sigma B_0^2 U + (\rho\beta^*)_{nf} g_c (T - T_0), \quad (2.4)$$

$$\rho_{nf} \left(\frac{\partial V}{\partial t} + U \frac{\partial V}{\partial X} + V \frac{\partial V}{\partial Y} \right) = -\frac{\partial P}{\partial Y} + \mu_{nf} \left(\frac{\partial^2 V}{\partial X^2} + \frac{\partial^2 V}{\partial Y^2} \right) - \frac{\mu_{nf}}{K_1} V, \quad (2.5)$$

$$(\rho C_p)_{nf} \left(U \frac{\partial T}{\partial X} + V \frac{\partial T}{\partial Y} \right) = k_{nf} \left(\frac{\partial^2 T}{\partial X^2} + \frac{\partial^2 T}{\partial Y^2} \right) - \left(\frac{\partial q_x}{\partial X} + \frac{\partial q_y}{\partial Y} \right) + Q_0^* (T - T_0). \quad (2.6)$$

Here, P is the pressure, B_0 is the uniform magnetic field strength, Q_0^* is amount of heat absorbed or generated per unit volume σ^* is the Stefan-Boltzmann constant and

k^* is the mean absorption coefficient. For the flow under consideration, the velocity field is $V = (U, V, 0)$. It is assumed that the temperature differences within the flow are small, so that the term T^4 may be expressed as a linear function of temperature. Hence by expanding T^4 in a Taylor's series about T_x and neglecting higher-order terms:

$$T^4 \approx 4T_x^3 T - 3T_x^4. \quad (2.7)$$

The appearance for static and wave structures are connected by the subsequent associations

$$x = X - c_1 t, \quad y = Y, \quad u = U - c_1, \quad v = V, \quad p = P. \quad (2.8)$$

After using the transformation given in Eq. (2.8) in Eqs. (2.3) – (2.6) reduce to

$$\frac{\partial u}{\partial x} + \frac{\partial v}{\partial y} = 0, \quad (2.9)$$

$$\rho_{nf} \left(u \frac{\partial u}{\partial x} + v \frac{\partial v}{\partial y} \right) = -\frac{\partial p}{\partial x} + \mu_{nf} \left(\frac{\partial^2 u}{\partial x^2} + \frac{\partial^2 u}{\partial y^2} \right) - \frac{\mu_{nf}}{K_1} (u + c_1) - \sigma B_0^2 (u + c_1) + (\rho \beta^*)_{nf} g (T - T_0), \quad (2.10)$$

$$\rho_{nf} \left(u \frac{\partial v}{\partial x} + v \frac{\partial v}{\partial y} \right) = -\frac{\partial p}{\partial y} + \mu_{nf} \left(\frac{\partial^2 v}{\partial x^2} + \frac{\partial^2 v}{\partial y^2} \right) - \frac{\mu_{nf}}{K_1} v, \quad (2.11)$$

$$(\rho C_p)_{nf} \left(u \frac{\partial T}{\partial x} + v \frac{\partial T}{\partial y} \right) = k_{nf} \left(\frac{\partial^2 T}{\partial x^2} + \frac{\partial^2 T}{\partial y^2} \right) - \frac{\partial q_r}{\partial y} + Q_0^* (T - T_0). \quad (2.12)$$

Introducing the dimensionless parameters as follows:

$$\begin{aligned} \bar{p} &= \frac{d_1^2}{\mu_f c_1 \lambda} p, \quad \bar{u} = \frac{u}{c_1}, \quad \bar{v} = \frac{v}{c_1 \delta}, \quad \bar{y} = \frac{y}{d_1}, \quad \bar{x} = \frac{x}{\lambda}, \quad \bar{t} = \frac{c_1}{\lambda} t, \quad \omega = \frac{b}{a}, \quad Q_0 = Q_0^* d_1^2 \\ \text{Re} &= \frac{c_1 d_1}{\nu_f}, \quad \delta = \frac{d_1}{\lambda}, \quad \bar{\theta} = \frac{T - T_0}{T_1 - T_0}, \quad \bar{\psi} = \frac{\psi}{c a}, \quad h_1 = \frac{H_1}{d_1}, \quad h_2 = \frac{H_2}{d_1}, \quad K = \frac{d_1^2}{K_1}, \\ a &= \frac{a_1}{d_1}, \quad b = \frac{b_1}{d_1}, \quad Gr = \frac{\beta^* g d_1^3}{\nu_f^2} (T_1 - T_0), \quad M^2 = \frac{\sigma_0 B_0^2 d_1^2}{\mu_f}, \quad N = \frac{16 \sigma^* T_0}{3 k^* k_f}, \end{aligned} \quad (2.13)$$

After using the above non-dimensional parameters and employing the assumptions of long wavelength ($\delta \rightarrow 0$), the dimensionless governing equations (without using bars) for nanofluid in the wave frame take the following form:

$$\frac{\partial u}{\partial x} + \frac{\partial v}{\partial y} = 0, \quad (2.14)$$

$$\frac{dp}{dx} = \frac{\mu_{nf}}{\mu_f} \frac{\partial^3 \psi}{\partial y^3} - K \frac{\mu_{nf}}{\mu_f} \left(\frac{\partial \psi}{\partial y} + 1 \right) - M \left(\frac{\partial \psi}{\partial y} + 1 \right) + Gr \frac{(\rho\beta^*)_{nf}}{(\rho\beta^*)_f} \theta, \quad (2.15)$$

$$\frac{dp}{dy} = 0, \quad (2.16)$$

$$\left(\frac{k_{nf}}{k_f} + N \right) \frac{\partial^2 \theta}{\partial y^2} + Q_0 \theta = 0. \quad (2.17)$$

Taking derivative of Eq. (2.15) with respect to y obtain

$$\frac{\mu_{nf}}{\mu_f} \frac{\partial^4 \psi}{\partial y^4} - K \frac{\mu_{nf}}{\mu_f} \left(\frac{\partial^2 \psi}{\partial y^2} \right) - M \left(\frac{\partial^2 \psi}{\partial y^2} \right) + Gr \frac{(\rho\beta^*)_{nf}}{(\rho\beta^*)_f} \frac{\partial \theta}{\partial y} = 0, \quad (2.18)$$

where $\psi(x, y)$ satisfies the continuity equation and the stream function defined as

$u = \partial \psi / \partial y$ and $v = -\partial \psi / \partial x$ The non-dimensional boundaries will take the form as

$$\psi = \frac{F}{2}, \quad \frac{\partial \psi}{\partial y} + \beta \frac{\partial^2 \psi}{\partial y^2} = -1 \quad \text{at } y = h_1, \quad (2.19)$$

$$\psi = -\frac{F}{2}, \quad \frac{\partial \psi}{\partial y} - \beta \frac{\partial^2 \psi}{\partial y^2} = -1, \quad \text{at } y = h_2, \quad (2.20)$$

$$\theta + \gamma \frac{\partial \theta}{\partial y} = 0 \quad \text{at } y = h_1, \quad \theta - \gamma \frac{\partial \theta}{\partial y} = 1 \quad \text{at } y = h_2. \quad (2.21)$$

Where $h_1 = 1 + a \cos(2\pi x)$, $h_2 = -d + b \cos(2\pi x + \omega)$. The thermo physical properties, for pure water, titanium dioxide, copper oxide and silicon dioxides are listed in table 2.1. In this chapter conductivity of nanofluids Eq. (1.14) and the effective viscosity of nanofluids Eq. (1.19) are considered.

Table 2.1. Thermal-physical properties of water and nanoparticles.

Physical Properties	Water (H_2O)	Titanium dioxide (TiO_2)	Copper oxide (CuO)	Silicon dioxide (SiO_2)
ρ (kgm^{-3})	997.1	4250.0	6500.0	3970.0
C_p ($Jkg^{-1}K^{-1}$)	4179	686.2	540.0	765.0
k ($W/m-K$)	0.613	0.90	0.85	0.63
β (K^{-1}) $\times 10^{-5}$	21	8.9538	18.0	36.0

2.2 Solution of the problem

The exact solutions of the Eqs. (2.17) and (2.18) along with boundary conditions Eqs. (2.19) – (2.21) are found as follows:

Integrating twice Eq. (2.17) with respect to y

$$\theta(y) = (C_2) \cosh[C_1 y] + (C_3) \sinh[C_1 y], \quad (2.22)$$

Here for simplicity we choose $C_1 = \frac{\sqrt{k_f} \sqrt{Q_0}}{\sqrt{Nk_f - k_{nf}}}$

Using the boundary conditions (2.19) in Eq. (2.22) the values of constants are as

$$C_2 = \frac{\sinh[C_1 h_1] + \gamma \cosh[C_1 h_1] C_1}{2\gamma \cosh[C_1 (h_1 - h_2)] C_1 + \sinh[C_1 (h_1 - h_2)] (1 + \gamma^2 C_1^2)}, \quad (2.23)$$

$$C_3 = -\frac{\cosh[C_1 h_1] + \gamma \sinh[C_1 h_1] C_1}{2\gamma \cosh[C_1 (h_1 - h_2)] C_1 + \sinh[C_1 (h_1 - h_2)] (1 + \gamma^2 C_1^2)}, \quad (2.24)$$

Integrating Eq. (2.18) with respect to y obtain

$$\psi = (-\sinh[yC_3] C_1 - \cosh[yC_3] C_2) C_8 + \frac{(\cosh[yC_7] - \sinh[yC_7]) C_9 + (\cosh[yC_7] + \sinh[yC_7]) C_{10}}{C_7^2} + C_{11} + yC_{12}, \quad (2.25)$$

where the constants $C_4 - C_8$ are defined as

$$C_4 = \frac{\mu_{nf}}{\mu_f}, C_5 = K \frac{\mu_{nf}}{\mu_f} + M, C_6 = Gr \frac{(\rho\beta^*)_{nf}}{(\rho\beta^*)_f}, C_7 = \frac{\sqrt{C_5}}{\sqrt{C_4}}, C_8 = \frac{C_6}{C_3^3 C_4 - C_5 C_5}. \quad (2.26)$$

Now using the boundary conditions (2.19) – (2.20) we obtain the constants of integration

$$\begin{aligned}
& \left(\begin{array}{l} \left(\begin{array}{l} \sinh \left[\frac{1}{2} C_3 (h_1 + h_2) \right] C_1 + \\ \cosh \left[\frac{1}{2} C_3 (h_1 + h_2) \right] C_2 \end{array} \right) C_3 \left(\begin{array}{l} \sinh \left[\frac{1}{2} C_3 (h_1 - h_2) \right] + \\ \beta \cosh \left[\frac{1}{2} C_3 (h_1 - h_2) \right] C_3 \end{array} \right) C_8 \\ - \cosh [C_7 h_1] + \cosh [C_7 h_2] - \\ \sinh [C_7 h_1] + \sinh [C_7 h_2] + \left(\frac{\cosh [C_7 h_1] +}{\sinh [C_7 h_1]} \right) C_7 (h_1 - h_2) + C_7^2 \\ \beta (\cosh [C_7 h_1] + \sinh [C_7 h_1]) C_7^2 (h_1 - h_2) \\ \left(\cosh [C_7 h_1] - \cosh [C_7 h_2] + \sinh [C_7 h_1] - \sinh [C_7 h_2] + \right) \\ \beta (\cosh [C_7 h_1] + \cosh [C_7 h_2] + \sinh [C_7 h_1] + \sinh [C_7 h_2]) \\ \left(-F - h_1 + C_2 C_8 (-\cosh [C_3 h_1] + \cosh [C_3 h_2] + \right. \\ \sinh [C_3 h_1] C_3 (h_1 - h_2) + \beta \cosh [C_3 h_1] C_3^2 (h_1 - h_2) + \\ C_1 C_8 (-\sinh [C_3 h_1] + \sinh [C_3 h_2] + \cosh [C_3 h_1] C_3 (h_1 - h_2) + \\ \left. + \beta \sinh [C_3 h_1] C_3^2 (h_1 - h_2)) + h_2 \right) \end{array} \right) \quad (2.27) \\
C_9 = \frac{\left(\begin{array}{l} \left(\begin{array}{l} \sinh \left[\frac{1}{2} C_7 (h_1 - h_2) \right] + \\ \beta \cosh \left[\frac{1}{2} C_7 (h_1 - h_2) \right] C_7 \end{array} \right) \left(\begin{array}{l} -2 \sinh \left[\frac{1}{2} C_7 (h_1 - h_2) \right] + \\ \cosh \left[\frac{1}{2} C_7 (h_1 - h_2) \right] C_7 (h_1 - h_2) + \\ \beta \sinh \left[\frac{1}{2} C_7 (h_1 - h_2) \right] C_7^2 (h_1 - h_2) \end{array} \right) \end{array} \right)}{
\end{aligned}$$

$$\begin{aligned}
& \left(\begin{array}{l} \left(\begin{array}{l} \sinh \left[\frac{1}{2} C_3 (h_1 + h_2) \right] C_1 + \\ \cosh \left[\frac{1}{2} C_3 (h_1 + h_2) \right] C_2 \end{array} \right) C_3 \left(\begin{array}{l} \sinh \left[\frac{1}{2} C_3 (h_1 - h_2) \right] + \\ \beta \cosh \left[\frac{1}{2} C_3 (h_1 - h_2) \right] C_3 \end{array} \right) C_7 C_8 \\ \cosh [C_7 h_1] - \cosh [C_7 h_2] + \sinh [C_7 h_1] - \\ \sinh [C_7 h_2] + \beta \left(\frac{\cosh [C_7 h_1] + \cosh [C_7 h_2] +}{\sinh [C_7 h_1] + \sinh [C_7 h_2]} \right) C_7 \end{array} \right) \quad (2.28) \\
C_{10} = \frac{\left(\begin{array}{l} \left(\begin{array}{l} \sinh \left[\frac{1}{2} C_3 (h_1 + h_2) \right] C_1 + \\ \cosh \left[\frac{1}{2} C_3 (h_1 + h_2) \right] C_2 \end{array} \right) C_3 \left(\begin{array}{l} \sinh \left[\frac{1}{2} C_3 (h_1 - h_2) \right] + \\ \beta \cosh \left[\frac{1}{2} C_3 (h_1 - h_2) \right] C_3 \end{array} \right) C_7 C_8 \end{array} \right)}{
\end{aligned}$$

$$C_{11} = \frac{1}{2} \left(\frac{F + 2 \sinh [C_3 h_1] C_1 C_8 + 2 \cosh [C_3 h_1] C_2 C_8 + \left(4 \left(\cosh [C_7 h_1] + \sinh [C_7 h_1] \right) \left(\sinh \left[\frac{1}{2} C_3 (h_1 + h_2) \right] C_1 + \cosh \left[\frac{1}{2} C_3 (h_1 + h_2) \right] C_2 \right) C_3 \left(\sinh \left[\frac{1}{2} C_3 (h_1 - h_2) \right] + \beta \cosh \left[\frac{1}{2} C_3 (h_1 - h_2) \right] C_3 \right) C_8 (-1 + C_7 h_1 + \beta C_7^2 h_1)}{\left(C_7 \left(\cosh [C_7 h_1] - \cosh [C_7 h_2] + \sinh [C_7 h_1] - \sinh [C_7 h_2] \right) + \beta \left(\cosh [C_7 h_1] + \cosh [C_7 h_2] + \sinh [C_7 h_1] + \sinh [C_7 h_2] \right) C_7 \right)} \right), \quad (2.29)$$

$$C_{12} = \frac{\left(\cosh \left[\frac{1}{2} C_7 (h_1 - h_2) \right] C_7 \left(F + \frac{\sinh [C_3 h_1] - \sinh [C_3 h_2]}{\sinh [C_3 h_2]} C_1 C_8 + \frac{\cosh [C_3 h_1] - \cosh [C_3 h_2]}{\cosh [C_3 h_2]} C_2 C_8 \right) + \beta \sinh \left[\frac{1}{2} C_7 (h_1 - h_2) \right] C_7^2 \left(F + \frac{\sinh [C_3 h_1] - \sinh [C_3 h_2]}{\sinh [C_3 h_2]} C_1 C_8 + \frac{\cosh [C_3 h_1] - \cosh [C_3 h_2]}{\cosh [C_3 h_2]} C_2 C_3 - \sinh \left[\frac{1}{2} C_7 (h_1 - h_2) \right] \right) - 2 + C_2 C_3 \left(\frac{\sinh [C_3 h_1] + \sinh [C_3 h_2] + \beta \left(\cosh [C_3 h_1] - \cosh [C_3 h_2] \right) C_3}{\beta \left(\sinh [C_3 h_1] - \sinh [C_3 h_2] \right) C_3} \right) C_8 + C_1 C_3 \left(\frac{\cosh [C_3 h_1] + \cosh [C_3 h_2] + \beta \left(\sinh [C_3 h_1] - \sinh [C_3 h_2] \right) C_3}{\beta \left(\sinh [C_3 h_1] - \sinh [C_3 h_2] \right) C_3} \right) C_8 \right)}{\left(2 \sinh \left[\frac{1}{2} C_7 (h_1 - h_2) \right] - \cosh \left[\frac{1}{2} C_7 (h_1 - h_2) \right] C_7 (h_1 - h_2) - \beta \sinh \left[\frac{1}{2} C_7 (h_1 - h_2) \right] C_7^2 (h_1 - h_2) \right)}, \quad (2.30)$$

The mean volume flow rate Q over one period is given as

$$Q = F + 1 + d. \quad (2.31)$$

Pressure gradient dp/dx ,

$$\frac{dp}{dx} = \left[\begin{array}{l} C_2 + (\cosh(C_{10}h_1) - C_{14} \sinh(C_{10}h_1)) + 2C_{10}(\beta C_9 - 1)(\cosh(C_9h_1)) \\ -\sin(C_9h_1) \left(\begin{array}{l} \beta C_{10} \cosh\left(\frac{1}{2}C_{10}(h_1 - h_2)\right) + \\ \sinh\left(\frac{1}{2}C_{10}(h_1 - h_2)\right) \end{array} \right) \left(\begin{array}{l} (C_5 + C_6) \cosh\left(\frac{1}{2}C_{10}(h_1 + h_2)\right) - \\ (C_7 + C_8) \sinh\left(\frac{1}{2}C_{10}(h_1 + h_2)\right) \end{array} \right) \end{array} \right] \quad (2.32)$$

The pressure rise Δp in non-dimensional form is defined as

$$\Delta p = \int_0^1 \frac{dp}{dx} dx, \quad (2.33)$$

2.3 Results and discussion

In this section our consideration is around understanding the impacts of different parameters on velocity and temperature distributions, pumping qualities, pressure gradient, and trapping phenomena for nanofluid that contain three types of particles copper oxide, titanium dioxide and silicon dioxide with water as a base fluid. Extraordinary importance is given to the nanoparticle concentrations, velocity and thermal slip parameters, heat generation and flux parameters, the Hartmann number as well as porosity parameter. The consequences of heat and mass flow along with pressure gradient and pressure rise are shown in Figs. 2.2(a) – 2.5(f). The trapping bolus phenomena is also with the help of streamlines as shown in the Figs. 2.6(a) – 2.9(f).

In order to analyze pumping characteristics, numerical study is done and results are displayed in Figs. 2.2(a) – 2.2(f), which demonstrates the variation of pressure rise per wavelength for different estimations of ϕ , Q_0 , β , γ , M and K along time average flux Q . Fig. 2.2 shows three unique locales as per the marks of Δp and Q . The quarter ($\Delta p > 0$, $Q < 0$) is notorious as retrograde pumping area. The area ($\Delta p > 0$, $Q > 0$) is known as peristaltic pumping quarter. The highest pressure is meant by P_0 in peristalsis fills for $Q = 0$. The corresponding time-average flux is represented as Q_0' which is acknowledged as free pumping at $\Delta p = 0$. The quarter ($\Delta p < 0$, $Q > 0$) is notorious as copumping region in pressure difference assists the flow as a result of peristalsis at the wall. Fig. 2.2(a) illustrates the impacts of volume fraction of the pressure rise Δp . Here, it is seen that pressure rise is increased with the increase of ϕ all through in the retrograde pumping area. This is due to fact that nanoparticle makes the walls more adaptable and liquid can easily pass, so that the pressure rise increases quickly when nanoparticles fraction increases. Fig. 2.2(b) describes that pressure rise

increases in the whole region for all three types of nanofluid as influence of Q_0 is dominated. In addition, least pressure rise is observed in case of $(SiO_2 + H_2O)$ whereas, pressure rise is noted when we choose $(CuO + H_2O)$. Fig. 2.2(c) exhibits the impact of slip parameter on pressure rise, it is watched that in the co-pumping area pressure rise increases by increase in β for each of the three types of fluid. Fig. 2.2(d) shows that pressure rise thrive with an expansion in thermal slip parameter all through the area for every one of the three types of fluid, however γ does not put extensive impact on $(SiO_2 + H_2O)$. Figs. 2.2(e) – 2.2(f) demonstrate the impact of Hartmann number and porosity parameter on pressure rise, it is watched that pressure rise increases by increase in M and K , in the locale where $\Delta p < 0$ however inverse conduct is seen in the retrograde pumping area.

From Fig. 2.3(a), one can see that pressure gradient dp/dx is decreased as increase of ϕ for every one of the three types of fluid. The variation of Q_0 on pressure gradient is appeared in Fig. 2.3(b), it demonstrates that dp/dx is falling down on an increase in Q_0 . Figs. 2.3(c) – 2.3(d) portray the impact of velocity and thermal slip parameter separately. It can be seen that dp/dx is increasing by increase in β , however inverse behavior is appeared on account of γ . Figs 2.3(e) - 2.3(f) are attracted to see the effect of parameters M and K on the variation of dp/dx from figures it is noticed that pressure gradient increases with increase in M and K , here portrayed Figs. 2.4(a) – 2.4(d) to understand the variation of temperature distribution over a cross area for various approximations of ϕ , Q_0 , N and γ .

Fig. 2.4(a) demonstrates that θ increases as increase in ϕ for all the three type of fluid, It is interesting to note that extreme variation happens $(TiO_2 + H_2O)$ while, generally less variation is appeared in $(CuO + H_2O)$ and the minimum variation is appeared in $(SiO_2 + H_2O)$. When it is watched in Figs. 2.4(b) and 2.4(c), the same pattern is observed for heat generation parameter Q_0 and heat flux parameter N individually, as it can be found in Fig. 2.4(a). An imperative part of current study is to break down the heat transfer in peristalsis with thermal slip parameter γ . With a specific end goal to see the effect of imperative thermal slip parameter γ on temperature profile, have drawn the Fig. 2.4(d) it is watched that by increasing γ , θ increases. It is of hobby that the most extreme variation happens in the event of $(CuO + H_2O)$, though generally low measure of variation is seen if there should be an occurrence of $(TiO_2 + H_2O)$ and least

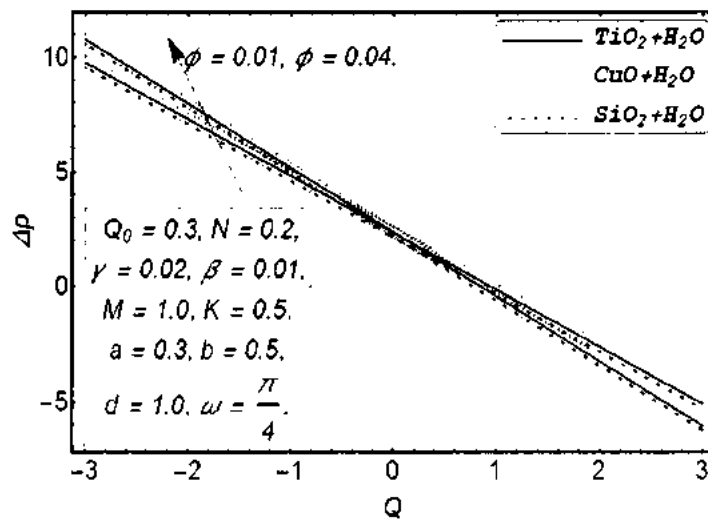
variation is seen in $(SiO_2 + H_2O)$. Figs. 2.5(a) – 2.5(f) are plotted to describe the impacts of related parameters on velocity profile u . It is seen from Fig. 2.5(a) that velocity profile increases alongside the right wall h_1 however decrease on the left wall h_2 of the channel with expanding the value of ϕ . It is shown in the Fig. 2.5(b) to acquire the variation of velocity profile u for different values of parameter Q_0 for every one of the three type of fluid. It portrays that velocity is increasing with increase of Q_0 at the center of channel however inverse conduct is seen along the left and right walls of channel. To see the conduct of N on velocity profile u , showed the Fig. 2.5(c). It is watched that close to the walls, velocity profile is increasing yet at the center of the channel velocity profile decreases by increase in N for all the three type of fluids, an inverse conduct is seen in the Fig. 2.5(b).

Fig. 2.5(d) determines the impact of β on velocity profile it is watched that close to one side and right wall velocity profile is increasing by increase of β , however at center of wall, it has seen the inverse conduct of velocity profile. To watch the conduct of Hartman number and porosity parameter with velocity profile, showed in the Figs. 2.5(e) and 2.5(f) these figures demonstrate that close to one side walls h_1 velocity is decreasing by increase of M and K individually, however close to the right wall, velocity increases.

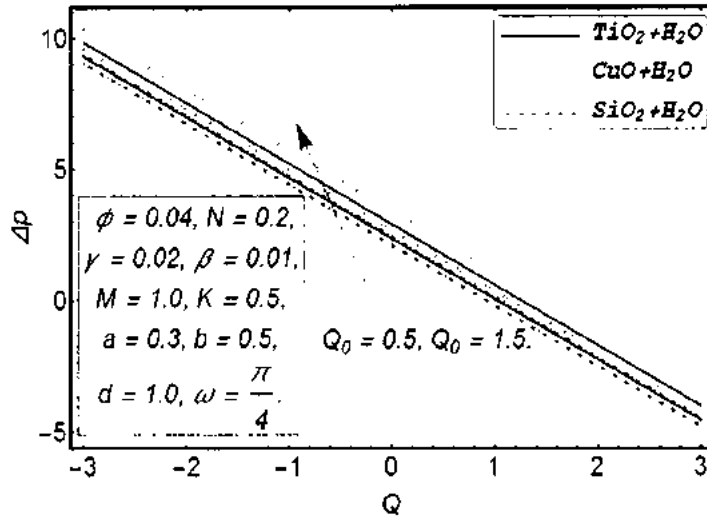
An extremely intriguing phenomena in the fluid transport is trapping. The development of an inside circling bolus of the fluid by closed streamlines is called trapping and this caught bolus is pushed ahead along the peristaltic wave with the velocity of wave. The bolus depicted as a volume of fluid limited by a closed streamline in the wave frame is moved at the wave pattern. Figs. 2.6(a) – 2.6(f) show typical contour maps for the streamlines with two estimations of ϕ ($\phi = 0.01$, $\phi = 0.04$), Figs. 2.7(a) – 2.7(f) show contour maps for the streamlines with two estimations of β ($\beta = 2.0$, $\beta = 4.0$), Figs. 2.8(a) – 2.8(f) show contours for the streamlines with two estimations of M ($M = 2.0$, $M = 2.1$) and Figs. 2.9(a) – 2.9(f) show contours for the streamlines with two estimations of K ($K = 2.0$, $K = 2.1$), for every one of the four kind of fluids ($TiO_2 + H_2O$, $CuO + H_2O$, $SiO_2 + H_2O$). Figs. 2.6(a) and 2.6(b) demonstrate the streamlines for $(TiO_2 + H_2O)$, it is seen that bolus turns out to be expansive when give more noteworthy qualities to the ϕ .

Figs. 2.6(c) and 2.6(d) demonstrate the streamlines for $(CuO + H_2O)$, it is noticed

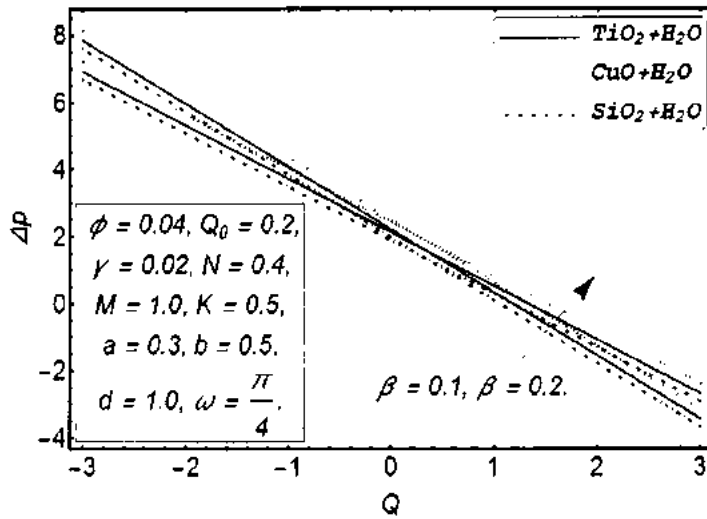
that number of bolus increments for higher estimations of ϕ , Figs. 2.6(e) and 2.6(f) demonstrate the streamlines for $(SiO_2 + H_2O)$. it is demonstrate that bolus turns out to be expansive as bigger estimations of ϕ . Figs. 2.7(a) and 2.7(b) demonstrate the streamlines for $(TiO_2 + H_2O)$. It is watched bolus gets to be smaller with the more noteworthy estimations of slip parameter β , Figs. 2.7(c) and 2.7(d) demonstrate the streamlines for $(CuO + H_2O)$, it is size of bolus is diminished for higher estimations of β , Figs. 2.7(e) and 2.7(f) demonstrate the streamlines for $(SiO_2 + H_2O)$, it is shown that bolus turns out to be small as bigger estimations of β . Figs. 2.8(a) and 2.8(b) demonstrate the streamlines for $(TiO_2 + H_2O)$, Figs. 2.8(c) and 2.8(d) demonstrate the streamlines for $(CuO + H_2O)$, Figs. 2.8(e) and 2.8(f) demonstrate the streamlines for $(SiO_2 + H_2O)$ and it is noticed that bolus turns out to be huge when it had given more noteworthy qualities to the Hartmann number M . Figs. 2.9(a) and 2.9(b) demonstrate the streamline for $(TiO_2 + H_2O)$, Figs. 2.9(c) and 2.9(d) demonstrates the streamlines for $(CuO + H_2O)$, Figs. 2.9(e) and 2.9(f) demonstrates the streamline for $(SiO_2 + H_2O)$ and it is noticed bolus turns out to be small when it had given more prominent qualities to the porosity parameter.



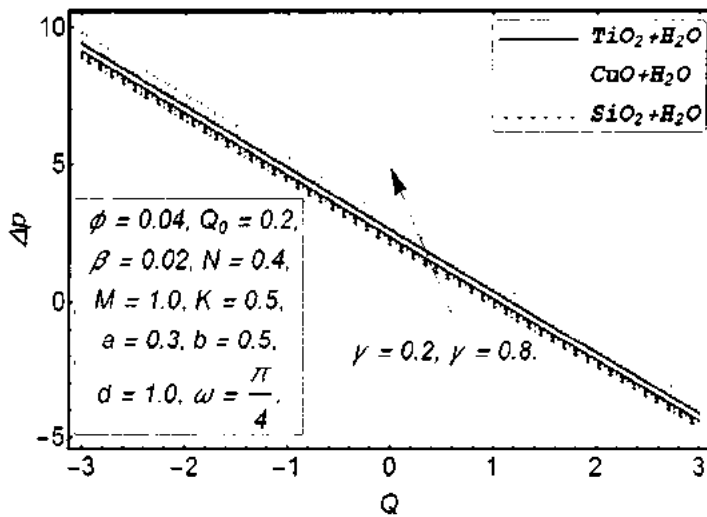
Figs. 2. 2(a). Variation of pressure rise Δp for flow parameter ϕ .



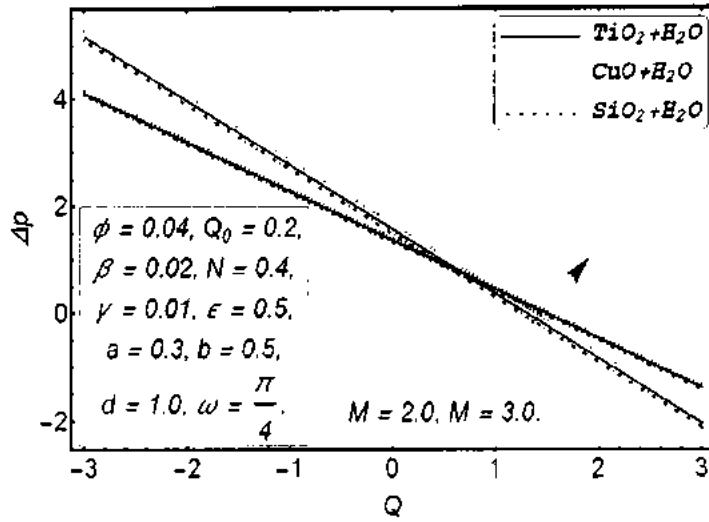
Figs. 2.2(b). Variation of pressure rise Δp for flow parameter Q_0 .



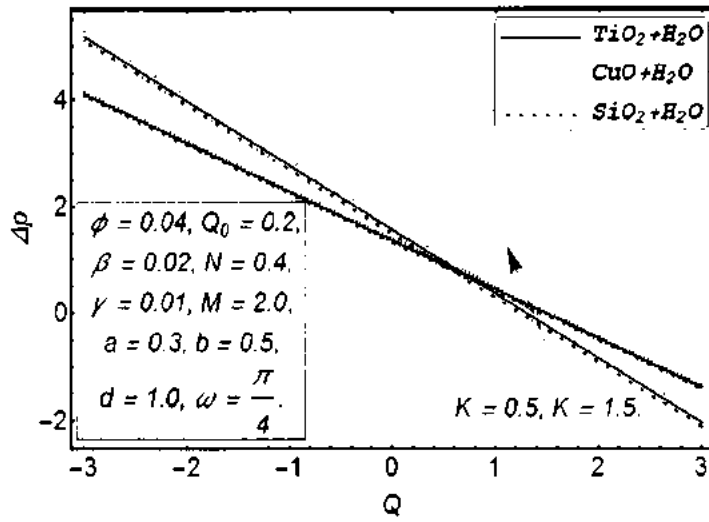
Figs. 2.2(c). Variation of pressure rise Δp for flow parameter β .



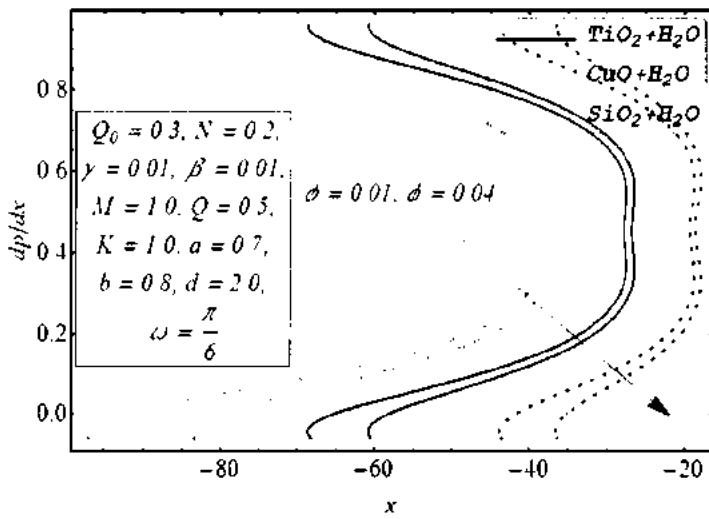
Figs. 2.2(d). Variation of pressure rise Δp for flow parameter γ .



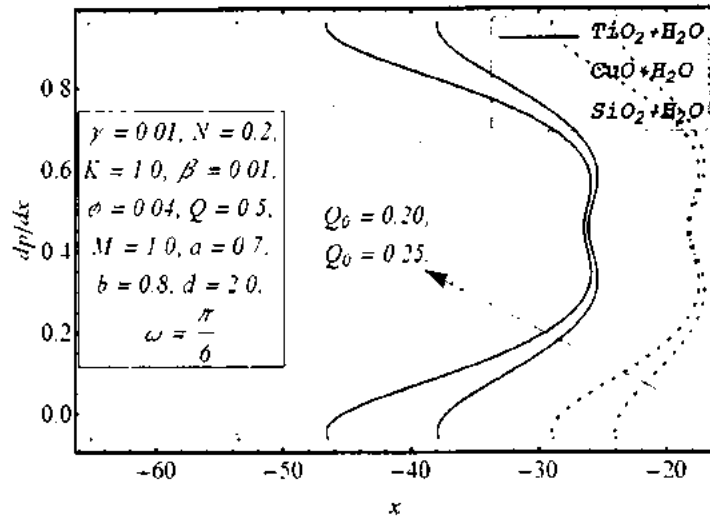
Figs. 2.2(e). Variation of pressure rise Δp for flow parameter M .



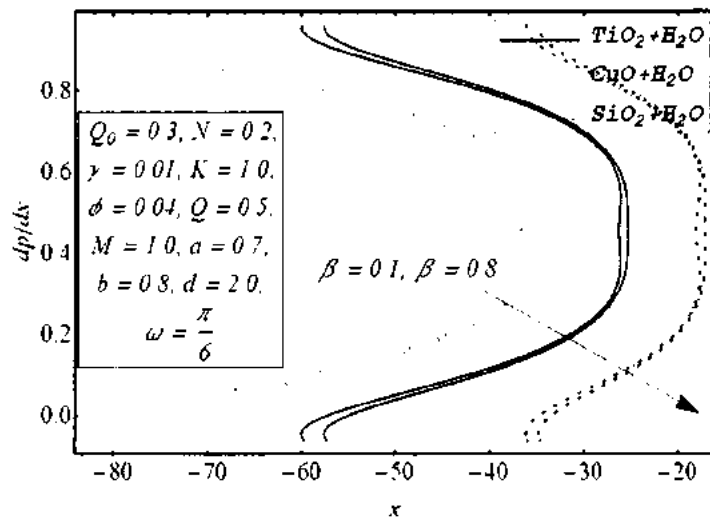
Figs. 2.2(f). Variation of pressure rise Δp for flow parameter K .



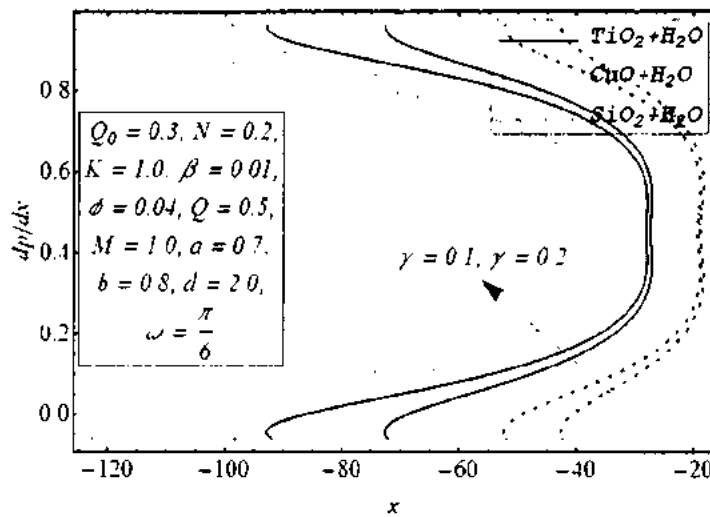
Figs. 2.3(a). Variation of pressure gradient dp/dx for flow parameter ϕ .



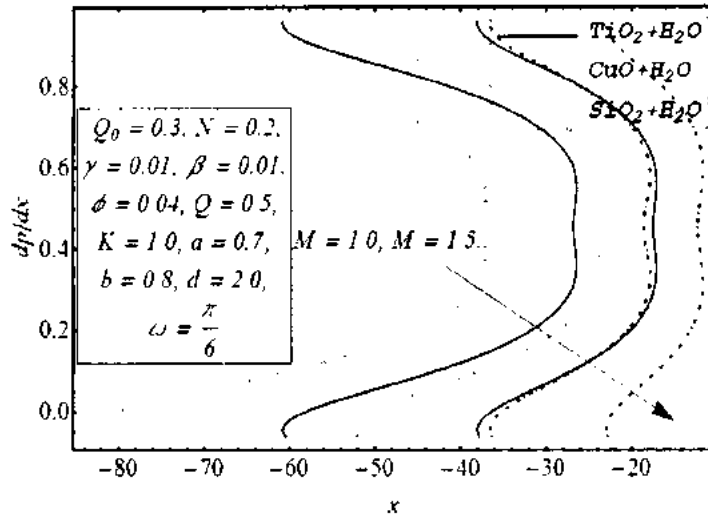
Figs. 2.3(b). Variation of pressure gradient dp/dx for flow parameter Q_0 .



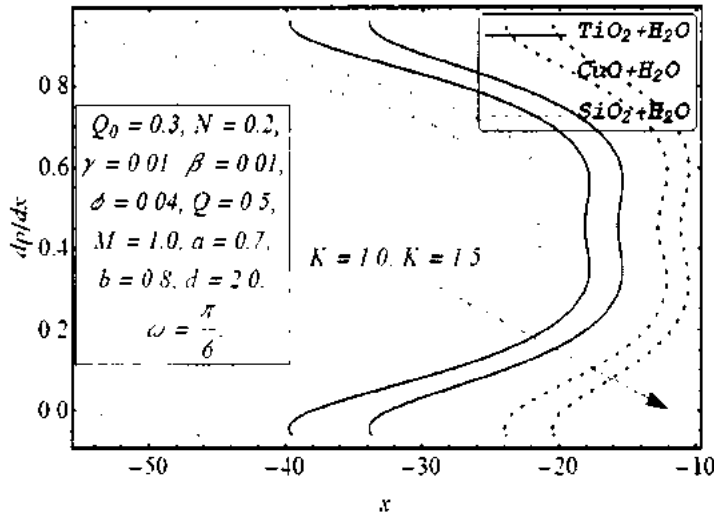
Figs. 2.3(c). Variation of pressure gradient dp/dx for flow parameter β .



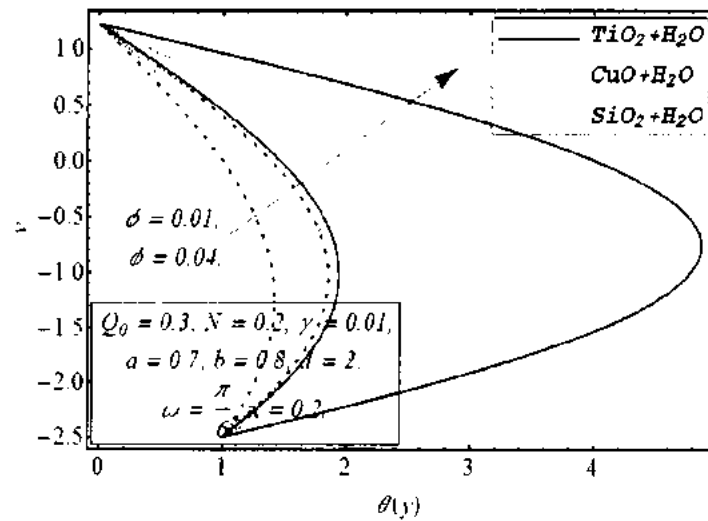
Figs. 2.3(d). Variation of pressure gradient dp/dx for flow parameter γ .



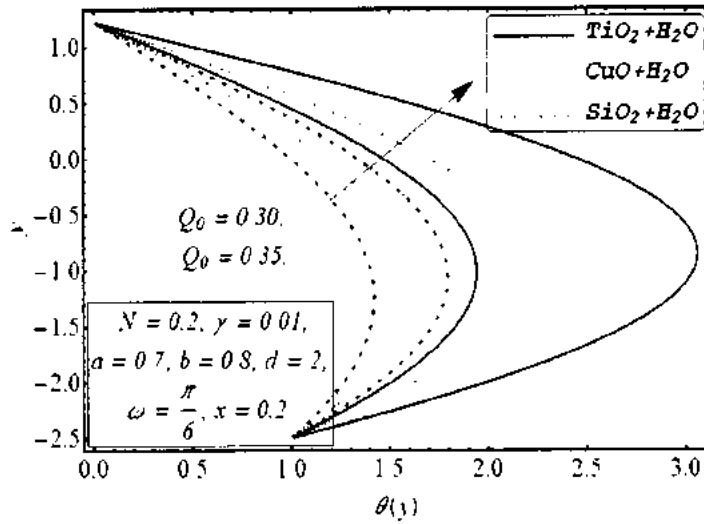
Figs. 2.3(e). Variation of pressure gradient dp/dx for flow parameter M .



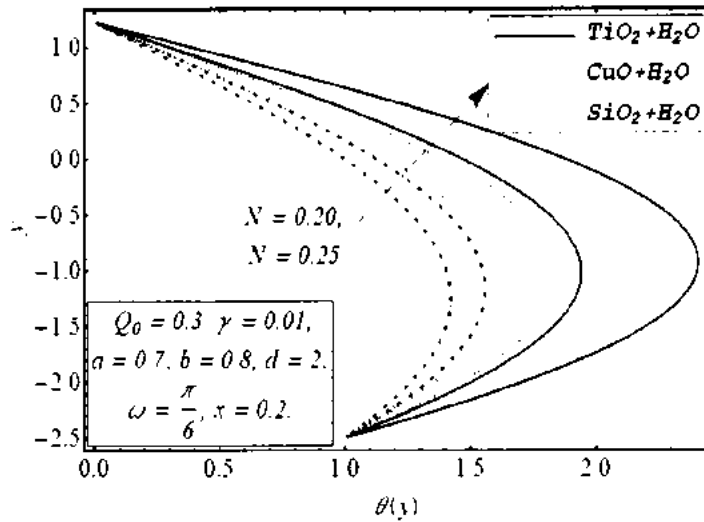
Figs. 2.3(f). Variation of pressure gradient dp/dx for flow parameter K .



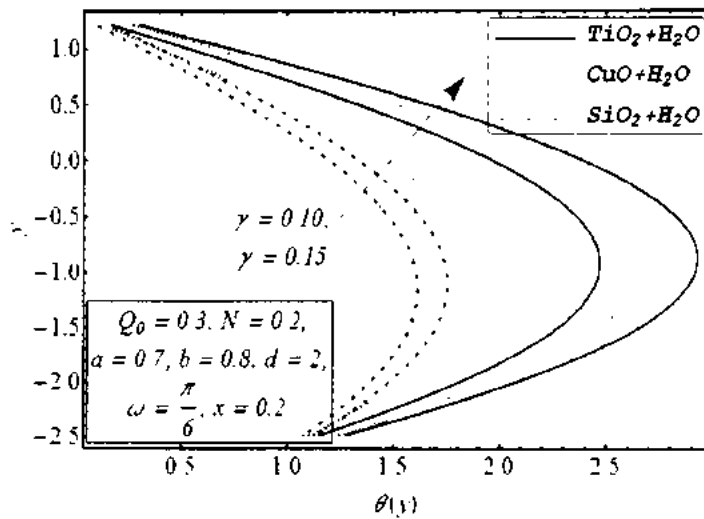
Figs. 2.4(a). Variation of temperature profile θ for ϕ .



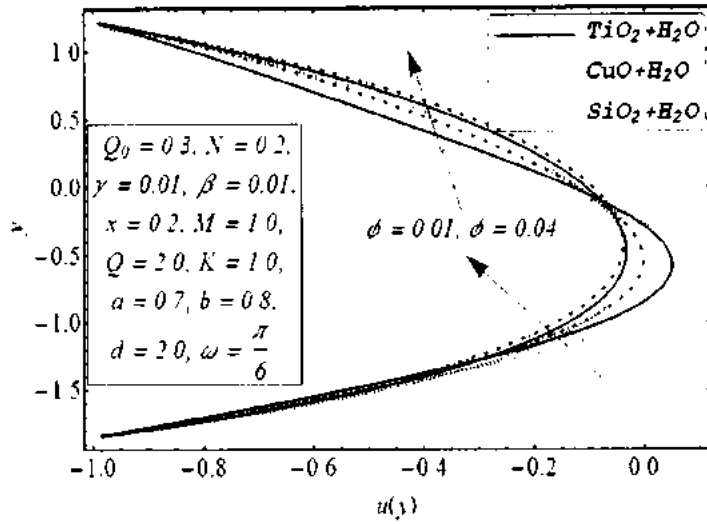
Figs. 2.4(b). Variation of temperature profile θ for flow parameter Q_0 .



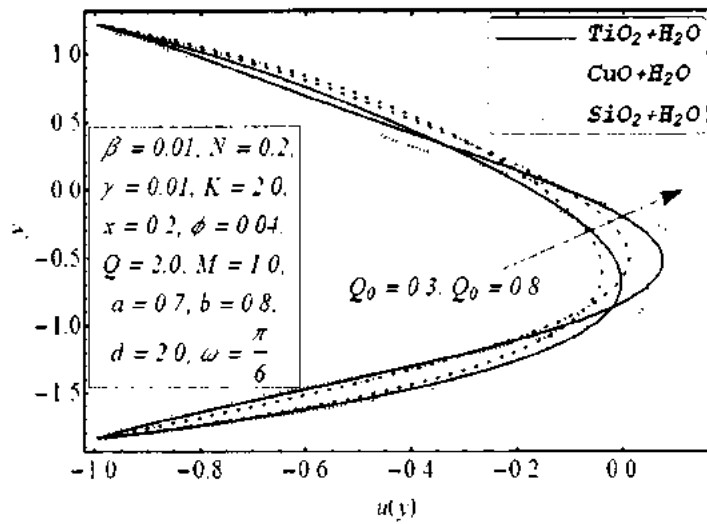
Figs. 2.4(c). Variation of temperature profile θ for flow parameter N .



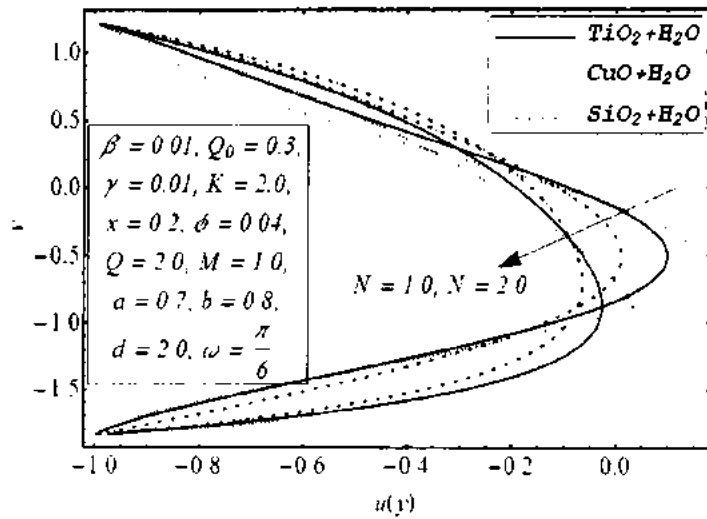
Figs. 2.4(d). Variation of temperature profile θ for flow parameter γ .



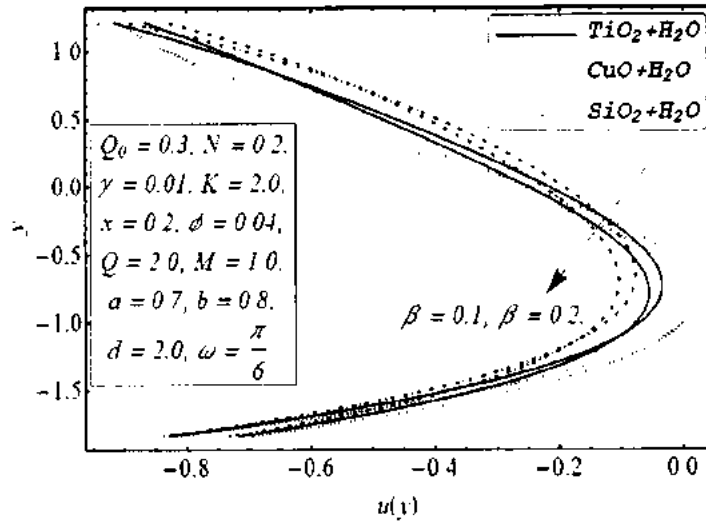
Figs. 2.5(a). Variation of velocity profile u with for flow parameter ϕ .



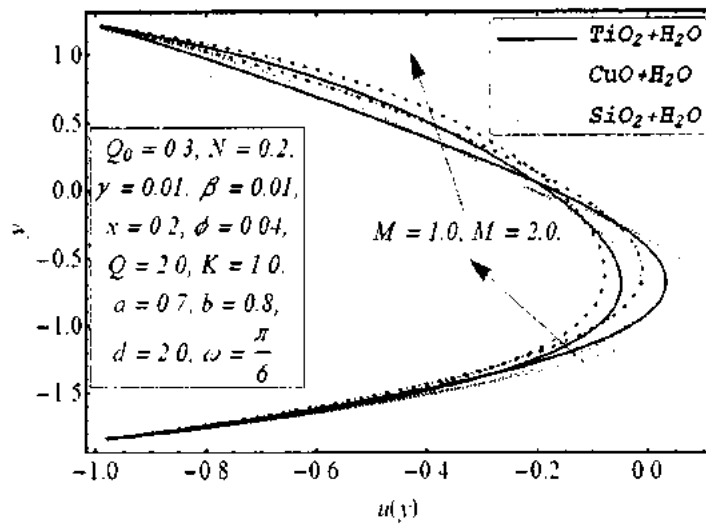
Figs. 2.5(b). Variation of velocity profile u with for flow parameter Q_0 .



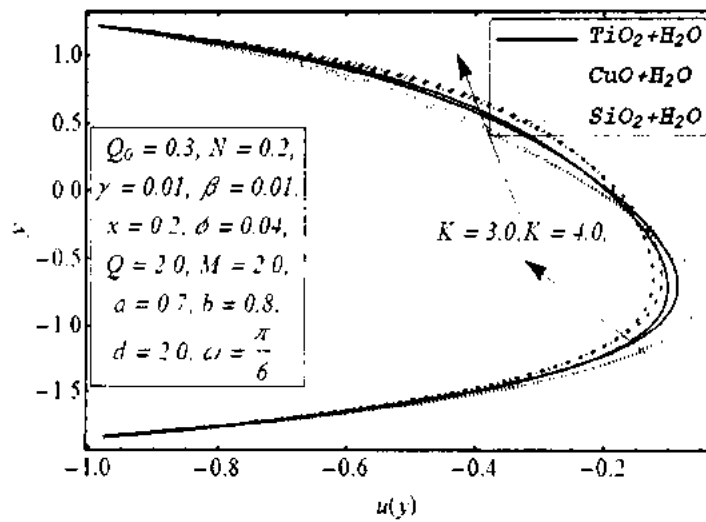
Figs. 2.5(c). Variation of velocity profile u with for flow parameter N .



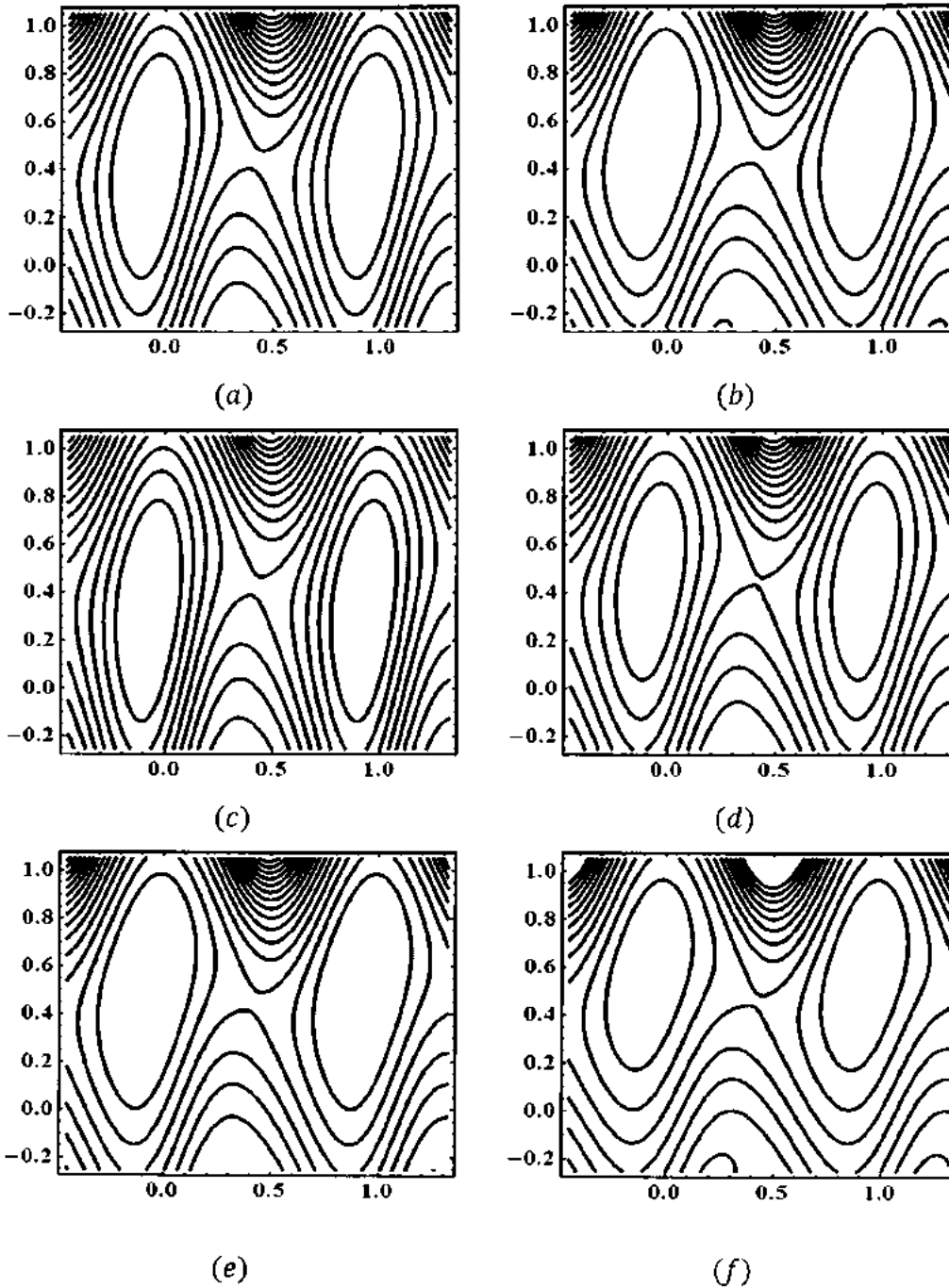
Figs. 2.5(d). Variation of velocity profile u with for flow parameter β .



Figs. 2.5(e). Variation of velocity profile u with for flow parameter M .

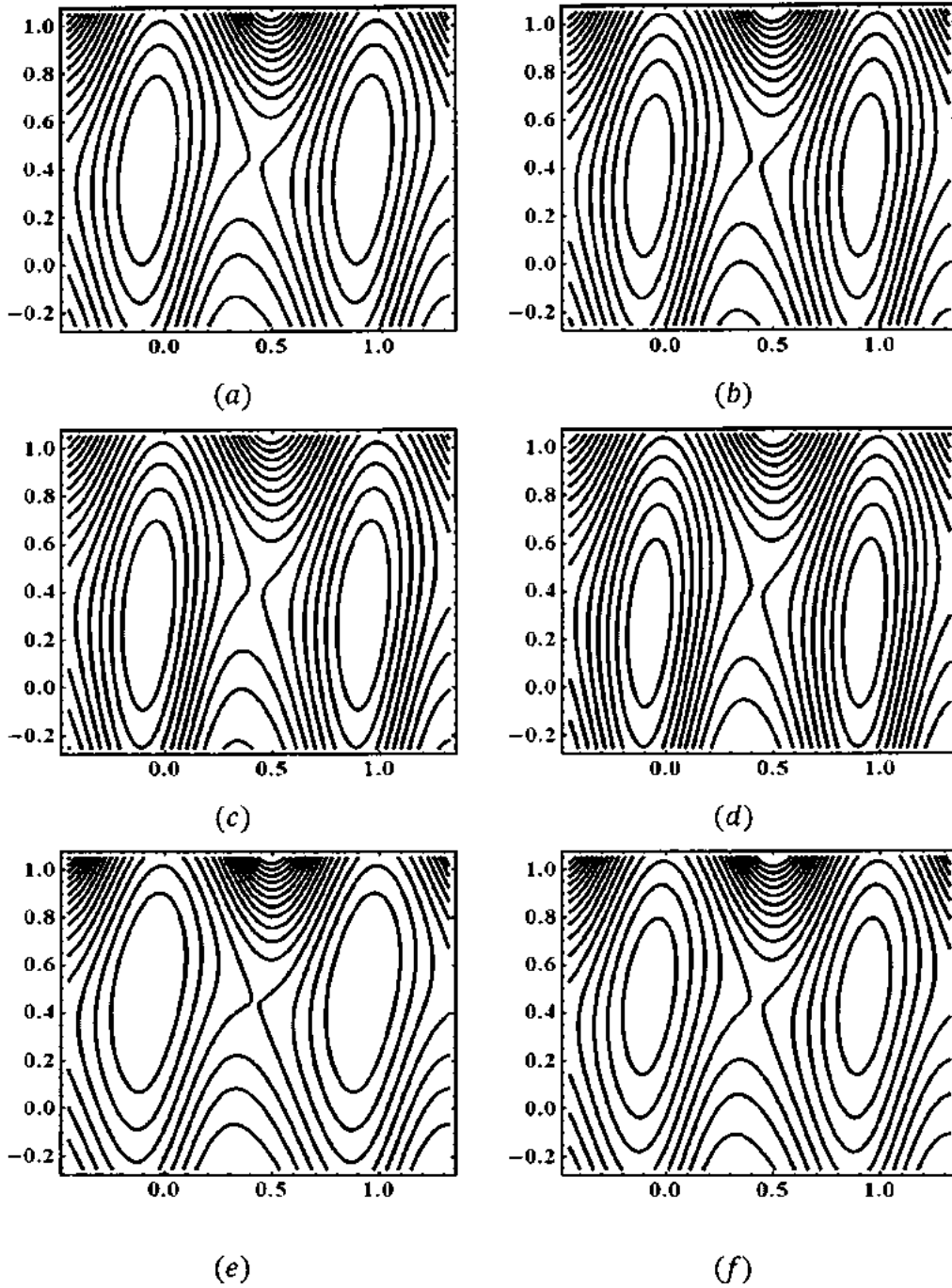


Figs. 2.5(f). Variation of velocity profile u with for flow parameter K .



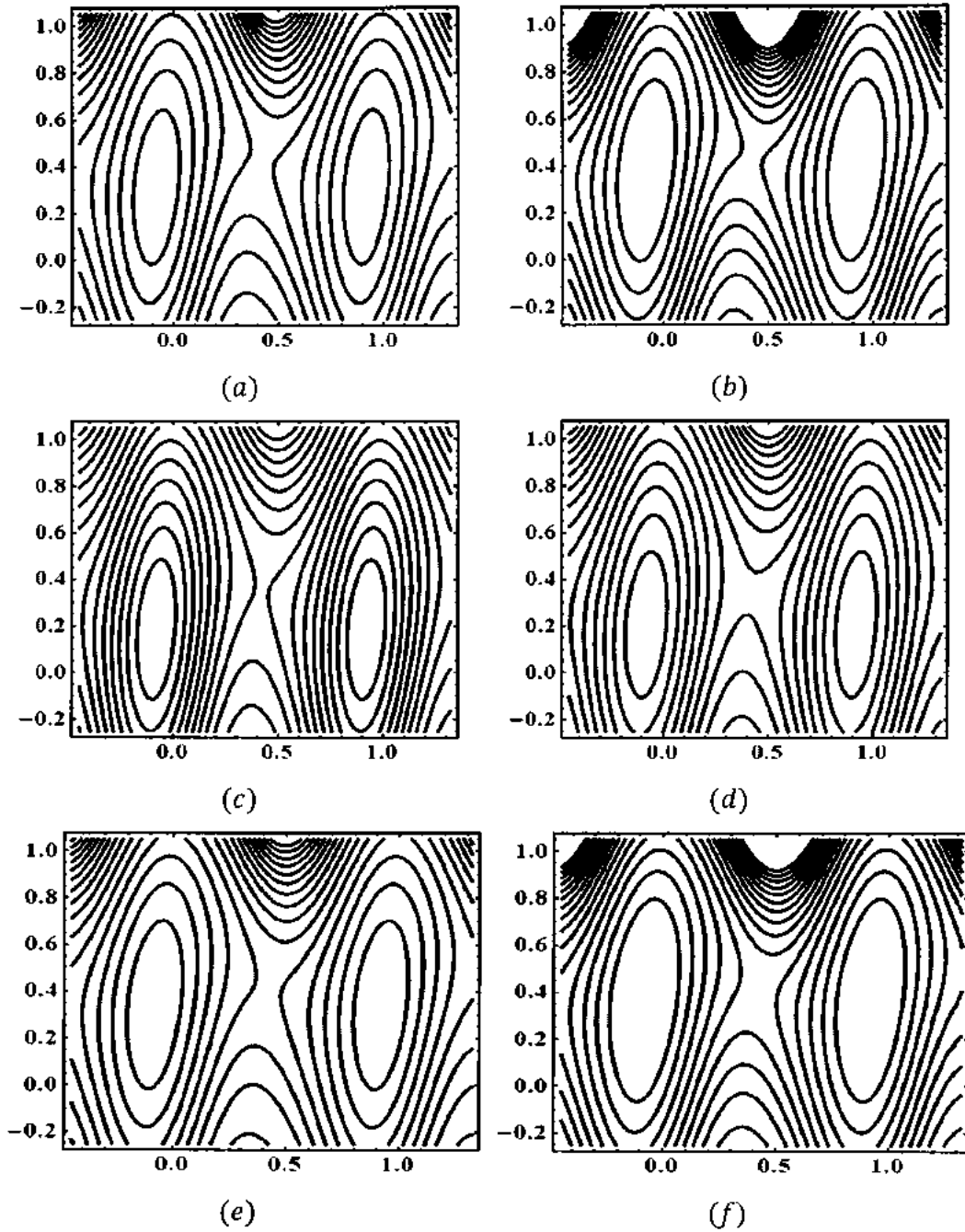
Figs. 2. 6(a) - 2. 6(d). Stream lines for different values of ϕ .

(a) for $\phi = 0.01(\text{TiO}_2 + \text{H}_2\text{O})$, (b) for $\phi = 0.04(\text{TiO}_2 + \text{H}_2\text{O})$, (c) for $\phi = 0.01(\text{CuO} + \text{H}_2\text{O})$, (d) for $\phi = 0.04(\text{CuO} + \text{H}_2\text{O})$, (e) for $\phi = 0.01(\text{SiO}_2 + \text{H}_2\text{O})$, (f) for $\phi = 0.04(\text{SiO}_2 + \text{H}_2\text{O})$. The other parameters are $Q = 2.0$, $\omega = \pi/4$, $a = 0.3$, $b = 0.5$, $d = 1.0$, $N = 0.4$, $\beta = 0.03$, $\gamma = 0.2$, $Q_0 = 0.4$, $M = 1.0$ and $K = 1.0$.



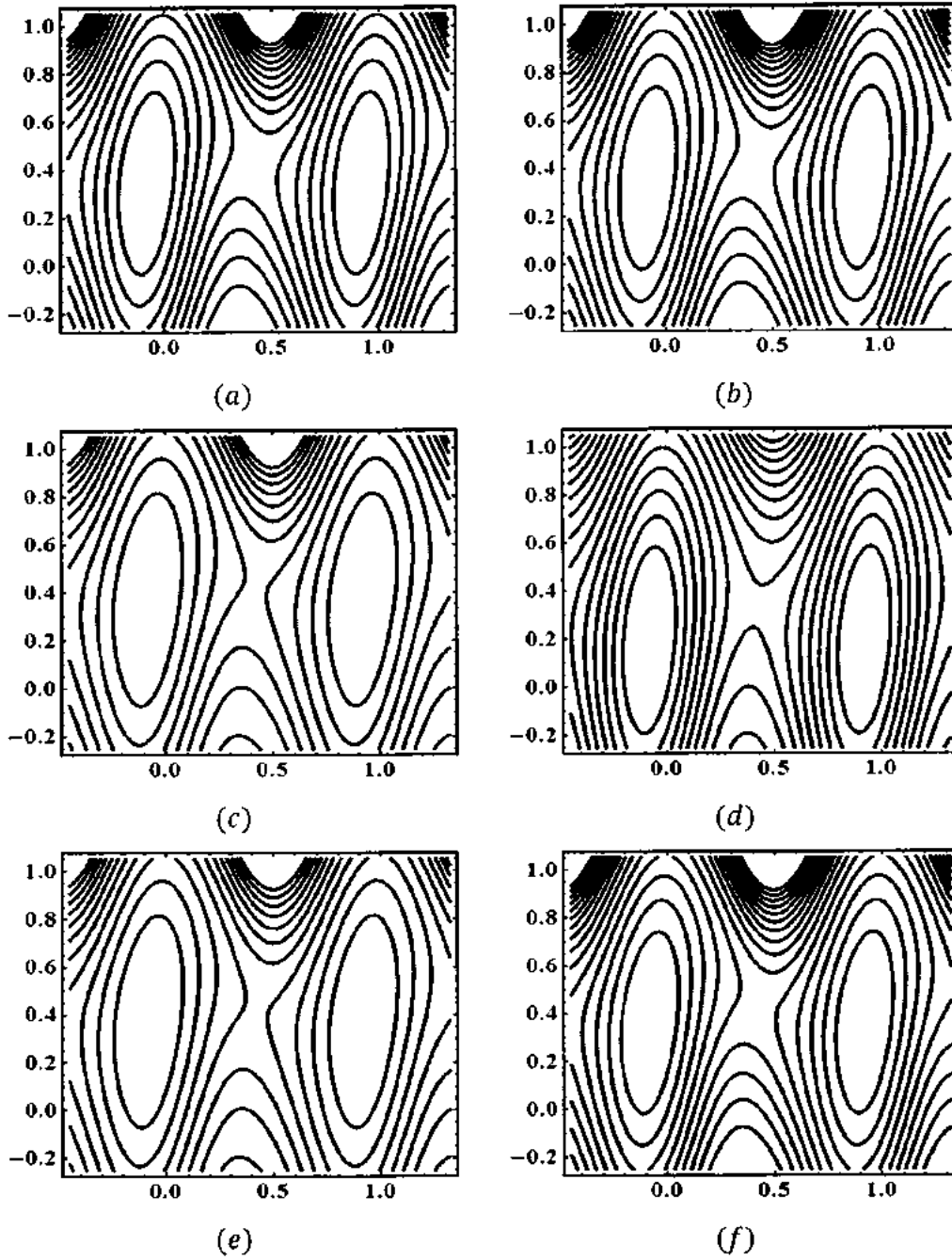
Figs. 2. 7(a) - 2. 7(f). Stream lines for different values of β .

(a) for $\beta = 0.10(\text{TiO}_2 + \text{H}_2\text{O})$, (b) for $\beta = 0.15(\text{TiO}_2 + \text{H}_2\text{O})$, (c) for $\beta = 0.10(\text{CuO} + \text{H}_2\text{O})$, (d) for $\beta = 0.15(\text{CuO} + \text{H}_2\text{O})$, (e) for $\beta = 0.10(\text{SiO}_2 + \text{H}_2\text{O})$, (f) for $\beta = 0.15(\text{SiO}_2 + \text{H}_2\text{O})$. The other parameters are $Q = 2.0$, $\omega = \pi/4$, $a = 0.3$, $b = 0.5$, $d = 1.0$, $N = 0.4$, $\phi = 0.04$, $\gamma = 0.2$, $Q_0 = 0.4$, $M = 1.0$ and $K = 1.0$.



Figs. 2. 8(a) - 2. 8(f). Stream lines for different values of M .

(a) for $M = 2.0(\text{TiO}_2 + \text{H}_2\text{O})$, (b) for $M = 3.0(\text{TiO}_2 + \text{H}_2\text{O})$, (c) for $M = 2.0(\text{CuO} + \text{H}_2\text{O})$, (d) for $M = 3.0(\text{CuO} + \text{H}_2\text{O})$, (e) for $M = 2.0(\text{SiO}_2 + \text{H}_2\text{O})$, (f) for $M = 3.0(\text{SiO}_2 + \text{H}_2\text{O})$. The other parameters are $Q = 2.0$, $\omega = \pi/4$, $a = 0.3$, $b = 0.5$, $d = 1.0$, $N = 0.4$, $\phi = 0.04$, $\gamma = 0.2$, $Q_0 = 0.4$, $\beta = 0.01$ and $K = 1.0$.



Figs. 2. 9(a)- 2. 9(f). Stream lines for different values of K .

(a) for $K = 3.0(\text{TiO}_2 + \text{H}_2\text{O})$, (b) for $K = 4.0(\text{TiO}_2 + \text{H}_2\text{O})$, (c) for $K = 3.0(\text{CuO} + \text{H}_2\text{O})$, (d) for $K = 4.0(\text{CuO} + \text{H}_2\text{O})$, (e) for $K = 3.0(\text{SiO}_2 + \text{H}_2\text{O})$, (f) for $K = 4.0(\text{SiO}_2 + \text{H}_2\text{O})$. The other parameters are $Q = 2.0$, $\omega = \pi/4$, $a = 0.3$, $b = 0.5$, $d = 1.0$, $N = 0.4$, $\phi = 0.04$, $\gamma = 0.2$, $Q_0 = 0.4$, $\beta = 0.01$ and $M = 2.0$.

2.4 Concluding remarks

In this chapter, key points are seen as:

- i. The impact of heat generation parameter on the pressure rise is minimum if there should be an occurrence of silicon dioxide and water though the impact of the parameter being a moderately larger than other two types of fluid.
- ii. The pressure rise is increasing with the increase of nanoparticle volume fraction coefficient all through in the peristaltic co-pumping area for each of the three sorts of fluid.
- iii. The thermal slip parameter does not put an extensive impact on pressure rise if there should arise an occurrence of silicon dioxide and water.
- iv. The pressure gradient increases with increase in Hartmann number and porosity parameter for every one of the three types of fluid.
- v. Temperature is expansions as increment of volume fraction, most extreme variation takes place for titanium oxide and water while, generally less variation is appeared in copper oxide water and the slightest variation is appeared in silicon oxide water.
- vi. It is observed that close to left and right wall velocity is increasing by the increase of slip parameter.
- vii. It is seen that bolus turns out to be larger when it has given greater value of nanoparticle volume fraction coefficient for each of the three types of fluid.

Chapter 3

Porosity effect in peristalsis flow of nanofluid with entropy generation

In this chapter, the peristaltic flow of nanofluid in vertical asymmetric porous channel is analyzed. For the nanofluid, the two diverse nanoparticles copper and silver are used as nanomaterial in water base fluid. Thermodynamic irreversibility is quantified through entropy calculations. The effects of sundry parameters on entropy generation and Bejan number are displayed for distinct nanofluid in graphical form. In addition, the results of heat transfer coefficient and enhancement are shown in tabular and bar chart.

3.1 Mathematical formulation

Consider water based nanofluid flow containing copper (Cu) and silver (Ag) nanoparticles in vertical asymmetric porous channel. The mathematical description of geometry of the problem is shown in Fig. 2.1. After using the relations Eq. (2.8) and non-dimensional parameters Eq. (2.13). In the presence of porosity and entropy, the governing Eqs. (1.39), (1.41) and (1.55) (without using bars) for nanofluid take the following forms

$$\frac{\partial u}{\partial x} + \frac{\partial v}{\partial y} = 0, \quad (3.1)$$

$$\frac{dp}{dx} = \frac{\mu_{nf}}{\mu_f} \frac{\partial^3 \psi}{\partial y^3} - K \frac{\mu_{nf}}{\mu_f} \left(\frac{\partial \psi}{\partial y} + 1 \right) + Gr \frac{(\rho\beta^*)_{nf}}{(\rho\beta^*)_f} \theta, \quad (3.2)$$

$$\frac{dp}{dy} = 0, \quad (3.3)$$

$$\frac{k_{nf}}{k_f} \frac{\partial^2 \theta}{\partial y^2} + Br \frac{\mu_{nf}}{\mu_f} \left(\frac{\partial^2 \psi}{\partial y^2} \right)^2 = 0 \quad (3.4)$$

where $Br = \frac{c_1^2 \mu_f}{k_f (T_1 - T_0)}$, taking derivative of Eq. (3.2) with respect to y yields

$$\frac{\mu_{nf}}{\mu_f} \frac{\partial^4 \psi}{\partial y^4} - K \frac{\mu_{nf}}{\mu_f} \left(\frac{\partial^2 \psi}{\partial y^2} \right) + \frac{Gr (\rho \beta^*)_{nf}}{Re (\rho \beta^*)_f} \frac{\partial \theta}{\partial y} = 0. \quad (3.5)$$

The non-dimensional boundaries will take the following form

$$\psi = \frac{F}{2}, \quad \frac{\partial \psi}{\partial y} = -1, \quad \text{at } y = h_1. \quad (3.6)$$

$$\psi = -\frac{F}{2}, \quad \frac{\partial \psi}{\partial y} = -1, \quad \text{at } y = h_2, \quad (3.7)$$

$$\theta = 0 \quad \text{at } y = h_1, \quad \theta = 1 \quad \text{at } y = h_2. \quad (3.8)$$

In the present chapter conductivity of nanofluid, Eq. (1.14) and the effective viscosity of nanofluid Eq. (1.19) are considered. The thermo-physical properties for pure water, copper and silver are listed in table. (3.1).

Table 3.1. Thermal-physical properties of water and nanoparticles.

Physical Properties	Water (H_2O)	Copper (Cu)	Silver (Ag)
$\rho (kgm^{-3})$	997.1	8933.0	10500.0
$C_p (Jkg^{-1}K^{-1})$	4179	385.0	235
$k (W / m-K)$	0.613	401.0	429.0
$\beta (K^{-1}) \times 10^{-5}$	21	1.67	1.89

Entropy generation can be defined as

$$S_G = \frac{k_{nf}}{T_0} \left(\left(\frac{\partial T}{\partial X} \right)^2 + \left(\frac{\partial T}{\partial Y} \right)^2 \right) + \frac{\mu_{nf}}{T_0} \left(2 \left(\left(\frac{\partial U}{\partial X} \right)^2 + \left(\frac{\partial U}{\partial Y} \right)^2 \right) + \left(\frac{\partial W}{\partial X} + \frac{\partial W}{\partial Y} \right)^2 \right) + \frac{\mu_{nf}}{T_0 k_f} (U + 1)^2. \quad (3.9)$$

Dimensionless form of the entropy generation with the help of Eq. (2.13) due to fluid friction and magnetic field is given as

$$N_s = \frac{S_G}{S_{G_0}} = Kf \left(\frac{\partial \theta}{\partial y} \right)^2 + \frac{Br}{\Lambda} A \left(\frac{\partial^2 u}{\partial y^2} \right)^2 + \frac{KBr(u+1)^2}{\Lambda}. \quad (3.10)$$

The dimensionless form of S_G is known as entropy generation number N_S which is the ratio of actual entropy generation rate to the characteristic entropy transfer rate S_{G_0} , which is defined as follows

$$S_{G_0} = \frac{k_w \Delta \bar{T}}{T_0 a_1^2}, \quad \Lambda = \frac{\Delta \bar{T}}{T_0}. \quad (3.11)$$

The total entropy generation in Eq. (3.10) can be written as

$$N_s = N_H + N_F + N_K, \quad (3.12)$$

where N_H is the entropy generation due to heat transfer, N_F is the local entropy generation due to fluid friction irreversibility and N_K is the entropy generation due to porous medium in the fluid. Alternatively, another irreversibility parameter is the Bejan number which is the ratio of heat transfer irreversibility to the total irreversibility due to heat transfer, fluid friction and magnetic field. Mathematically,

$$B_e = \frac{N_H}{N_s}, \quad (3.13)$$

where Bejan number ranges from 0 to 1.

3.2 Solution of the problem

The system of coupled nonlinear differential Eqs. (3.4) and (3.5) along with the boundary conditions (3.6) – (3.8) are solved by the Mathematica package BVP4c 2.0 which is based on the homotopy analysis method. In this package, we choose the auxiliary linear operators and initial guess for the desired solutions as follows:

$$\mathcal{L}_1(\psi) = \frac{d^4 \psi}{dy^4}, \quad \mathcal{L}_2(\theta) = \frac{d^2 \theta}{dy^2}, \quad (3.14)$$

$$\psi_0(y) = -\frac{(h_1 + h_2 - 2y) \left(-2(h_1 - h_2)(h_1 - y)(h_2 - y) + F(h_1^2 - 4h_1 h_2 + h_2^2 + 2(h_1 + h_2)y - 2y^2) \right)}{2(h_1 - h_2)^3}, \quad (3.15)$$

$$\theta_0(y) = \frac{(h_1 - y)}{(h_1 - h_2)}. \quad (3.16)$$

So far, we have defined all the input of this problem properly, except the convergence-control parameters $C_n[k]$.

Usually, the optimal values of the convergence-control parameters are obtained by minimizing the squared residual error.

$$E_w = \int_{h_1}^{h_2} \left(\frac{\mu_{nf}}{\mu_f} \frac{\partial^4 \psi}{\partial y^4} - K \frac{\mu_{nf}}{\mu_f} \left(\frac{\partial^2 \psi}{\partial y^2} \right) + G, \frac{(\rho\beta^*)_{nf}}{(\rho\beta^*)_f} \frac{\partial \theta}{\partial y} \right)^2 dy, \quad (3.17)$$

$$E_\theta = \int_{h_1}^{h_2} \left(\frac{k_{nf}}{k_f} \frac{\partial^2 \theta}{\partial y^2} + Br \frac{\mu_{nf}}{\mu_f} \left(\frac{\partial^2 \psi}{\partial y^2} \right)^2 \right)^2 dy. \quad (3.18)$$

The results for velocity and temperature at second iterations of package are obtained as

$$\psi(y) = C_{13} + C_{14}y + C_{15}y^2 + C_{16}y^3 + C_{17}y^4 + C_{18}y^5 + C_{19}y^6 + C_{20}y^7, \quad (3.19)$$

$$\theta(y) = C_{21} + C_{22}y + C_{23}y^2 + C_{24}y^3 + C_{25}y^4 + C_{26}y^5 + C_{27}y^6 + C_{28}y^7. \quad (3.20)$$

The coefficients $C_{13} - C_{28}$ can be obtained through routine calculation.

3.3 Results and discussion

In this section, all the obtained solutions graphically under the variations of various pertinent parameters on the profiles of pressure gradient, temperature, velocity, entropy generation number and Bejan number through Figs. 3.1(a) to 3.7(d) with water based nanofluids contained Copper and Silver nanoparticles. The expression for the pressure rise is calculated numerically using a Mathematica 9.0 software. The trapping bolus phenomenon observing the flow behavior is also manipulated as well with the help of streamlines graphs Figs. 3.8(a) to 3.10(c).

In the Figs. 3.1(a) – 3.1(b) we have shown the pressure rise. Fig. 3.1(a) represents the effects of Brinkman number Br on the pressure rise against the flow rate Q for different values of Br . It is noticed here that pressure rise is an increasing function with the increases of Br throughout in the pumping region ($\Delta p > 0$) at the same time, Δp will be decreasing as the Br increases in the augmented pumping region ($\Delta p < 0$). This can be viewed from Fig. 3.1(b) that Δp will be shows opposite behavior for K as we observed in Fig. 3.1(a). From Fig. 3.2(a), one can see that pressure gradient dp/dx is decreases by increasing the nanoparticle volume fraction ϕ i.e. more the volume fraction lesser the pressure gradient for both type of nanoparticles copper and

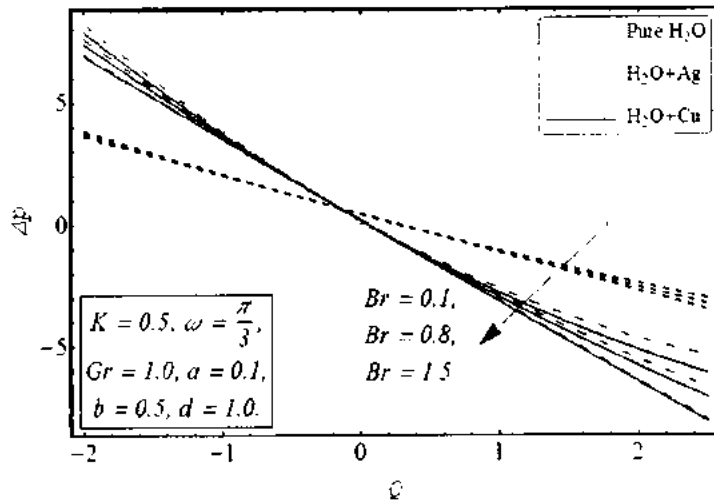
silver. The variation of porosity parameter K on pressure gradient is shown in Fig. 3.2(b), it shows that pressure gradient is increasing on an increase in K for all three types of fluid it is also observed that pressure gradient is least in case of pure water whereas the effect of K is relatively larger in the cases of copper water and silver water fluid. When we observe Fig. 3.2(c) we have observed that by increasing Br , pressure gradient is increasing.

The Fig. 3.3(a) presents the effects of temperature θ for the different values of volume fraction ϕ it is observed that as we increases the ϕ temperature also increase for both type of fluid copper water and silver water but the impact of silver water fluid is greater than the copper water fluid it is may due to maximum thermal conductivity of silver is caused of maximum temperature, we presented the Fig. 3.3(b) to show the behavior of temperature profile with the effect of Brinkman number Br the temperature θ increases as the increases of Br for all three cases of study, the impact in the case of pure water is least. The Fig. 3.4(a) presents the effects of velocity u for the different values of volume fraction ϕ it is observed that these figure are prepare within range of particle volume fraction $1\% \leq \phi \leq 4\%$, as the requirement of Eqn. 1.17 we see from the figure that as we increases the ϕ velocity also increases, we presented the Fig. 3.4(b) to show the behavior of velocity profile with the effect of porosity parameter K it is observed that near the left wall velocity profile decreasing by increases of K but near the right wall we noticed the opposite behavior of velocity profile. We can see the impact of parameters Gr on the variation of velocity from Fig. 3.4(c). It is noted that velocity is decreases as increases of Gr near the left wall of the channel while the opposite behavior is noticed near the right wall of the channel it is also observed that impact of Gr on velocity considerably least as the case of pure water as compare of copper and silver water fluid.

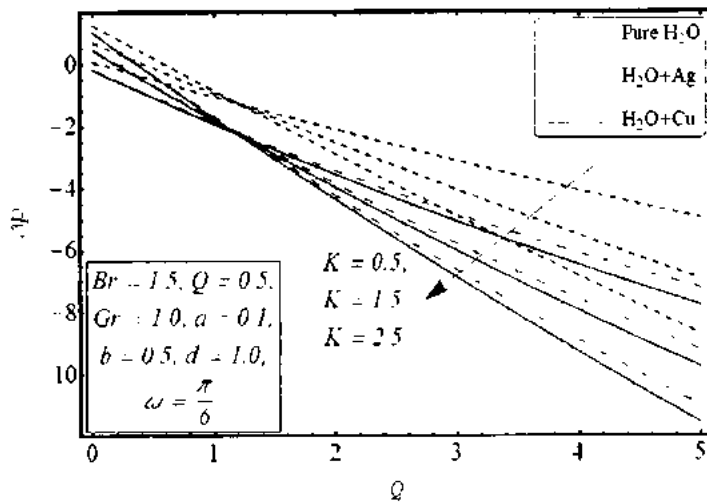
We have presented the Figs.3.5(a) – 3.5(c) to obtain the variation of entropy generation number Ns for varying the magnitude of the parameters K , Λ and Br . From Fig. 3.5(a) it depicts that Ns is increasing with increase porosity parameter K . Figs 3.5(b) shows the higher value of Λ displays least entropy and 3.5(c) shows that Ns is directly proportional Br throughout the channel for all three types of fluid the impact of copper water and silver water is observed more than pure water.

Figs. 3.6(a) – 3.6(c) are prepared to analyze the Bejan number with respect to change in different physical constraints involved. Fig.3.6(a) depicts that with the increase in K , there is a decrease in Bejan number. Fig. 3.6(b) shows the variation of Bejan number for different values of Λ , we see that Bejan number is increasing by increase in the values of Λ . Fig. 3.6(c) shows that there is an opposite behavior for Br as we see for Λ . The effect of porosity parameter K on the trapping is illustrated in Figs. 3.7(a) – 3.9(c). In these figure, we kept all parameter fixed as $a = 0.1$, $b = 0.5$, $d = 1$, $Q = 2.5$, $\omega = \frac{\pi}{6}$, $Br = 0.3$ and $Gr = 2$. Figs. 3.7(a) – 3.7(c) show the streamlines with three values of K ($K = 1.7, K = 2.4, K = 2.8$) for pure water. It is noticed that bolus becomes larger when we give greater values of K . Figs. 3.8(a) – 3.8(c) show the streamlines for $H_2O + Cu$ and it is noticed that boluses becomes large for higher values of porosity parameter K . Further, more trapped bolus appears with increasing permeability parameter K . Figs. 3.9(a) – 3.9(c) shows the streamlines for $H_2O + Ag$, one can observed that size of bolus becomes large as large values of K , from all these Figures it is important to noticed that boluses formation is not symmetric about the central line of the channel.

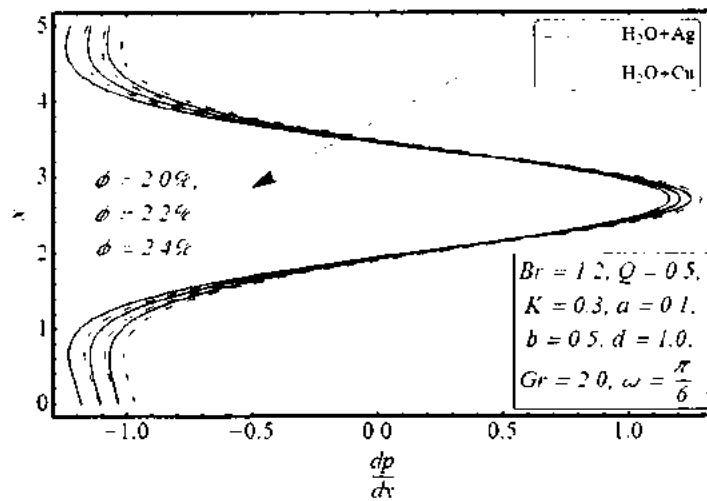
The dimensionless form of heat transfer coefficient $h = -K_f \theta'(0)$, numerically results in the tables 3.2 to 3.3 illustrate the effects of particles volume fraction and porosity parameter on the heat transfer coefficient. These tables are repaired by fixing the parameters as $a = 0.1$, $b = 0.5$, $d = 1$, $Q = 0.5$, $\omega = \frac{\pi}{6}$, $Br = 0.3$ and $Gr = 1$. The table 3.2 depicts that when volume fraction of nanoparticles suspension in the base fluid is increased heat transfer rate, i.e., when we choose silver and copper nanoparticles, heat transfer rate of water is improve for copper 30.59%, 33.75% and 35.89 % corresponding to 1%, 2.5% and 4% particles volume fraction respectively similarly for silver nanoparticles 31.84%, 34.93% and 37.04 % corresponding to 1%, 2.5% and 4% particles volume fraction shown in the form of bar chart 3.1. The effect of porosity parameter on heat transfer coefficient in table 3.3. In this table, we analysis that heat transfer decreased with the enhancement of porosity parameter. We also examine that in the case silver particles heat transfer are more rapidly decreased as compare to copper water case shown pictorially in the form of bar chart 3.2.



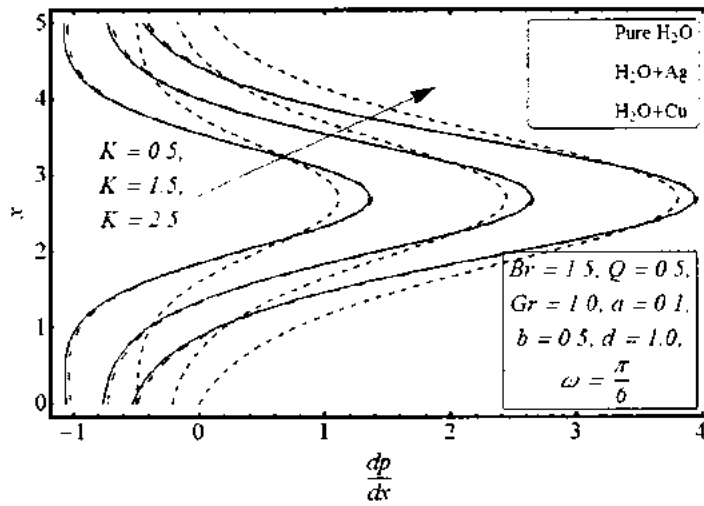
Figs. 3.1(a): Variation of pressure rise Δp for different values of Br .



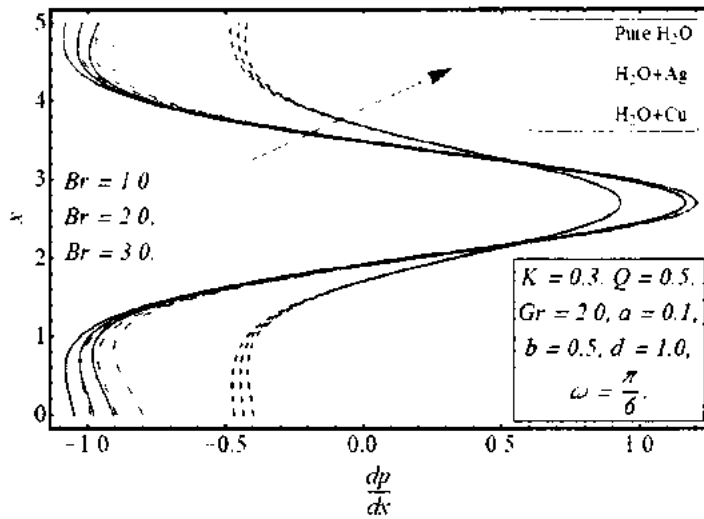
Figs. 3.1(b): Variation of pressure rise Δp for different values of K .



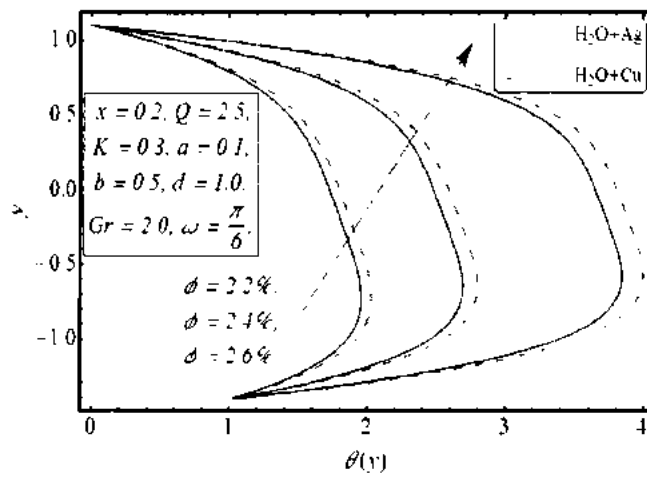
Figs. 3.2(a): Variation of pressure gradient dp/dx for different value ϕ .



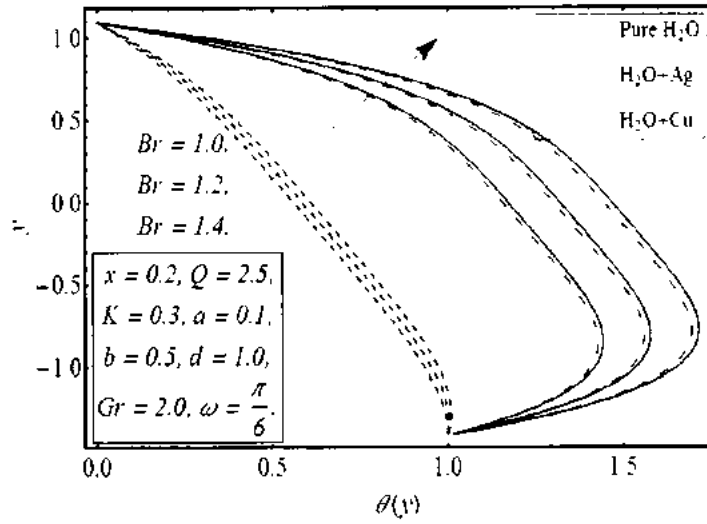
Figs. 3.2(b): Variation of pressure gradient dp/dx for different value K .



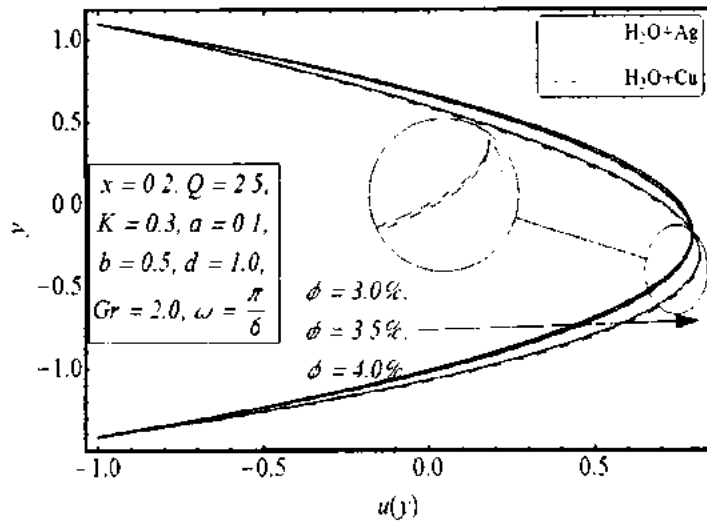
Figs. 3.2(c): Variation of pressure gradient dp/dx for different value Br .



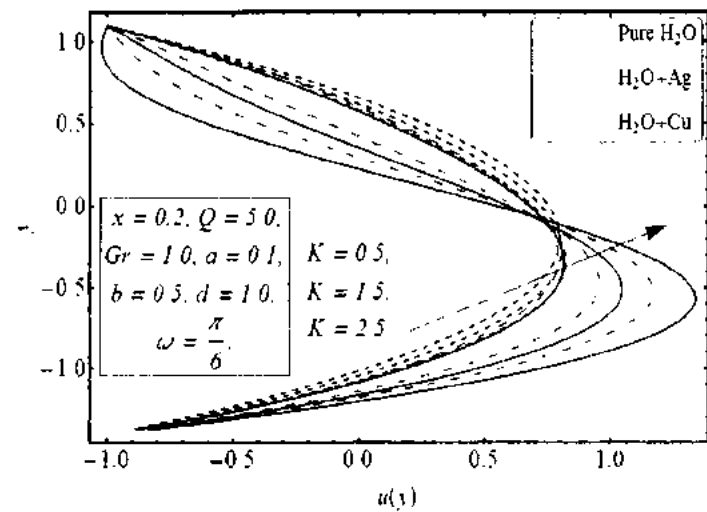
Figs. 3.3(a): Variation of temperature profile θ for different value ϕ .



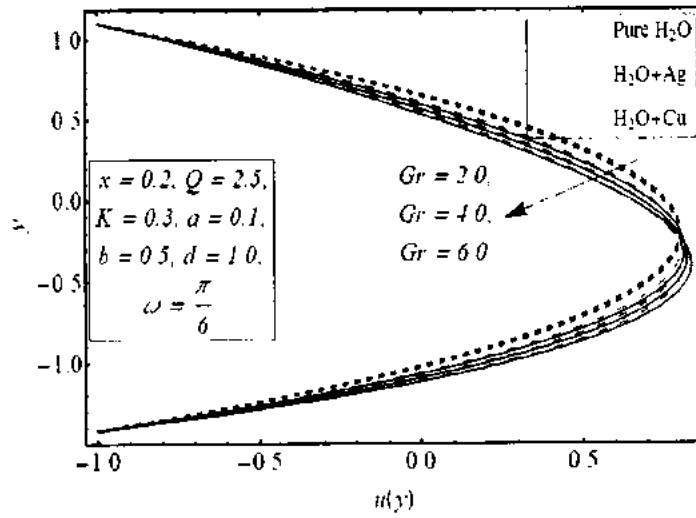
Figs. 3.3(b): Variation of temperature profile θ for different value Br .



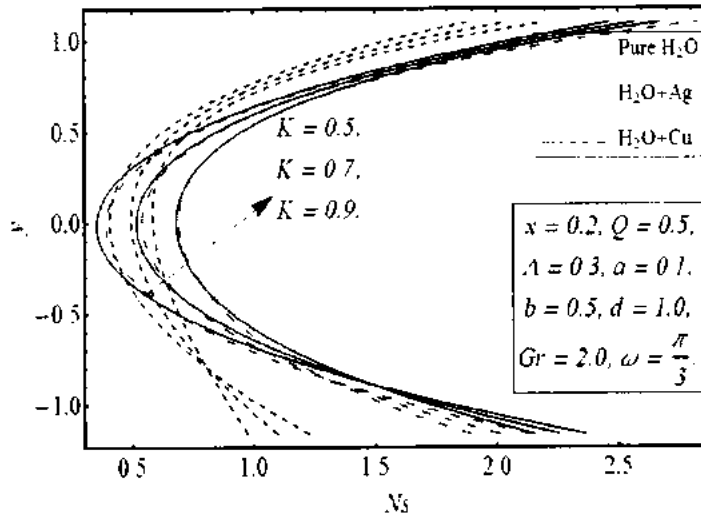
Figs. 3.4(a): Variation of velocity profile u with for different value ϕ .



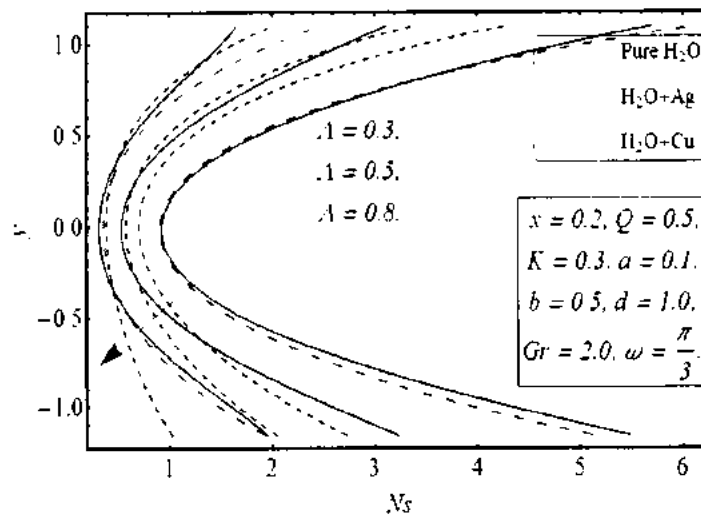
Figs. 3.3(b): Variation of velocity profile u with for different value K .



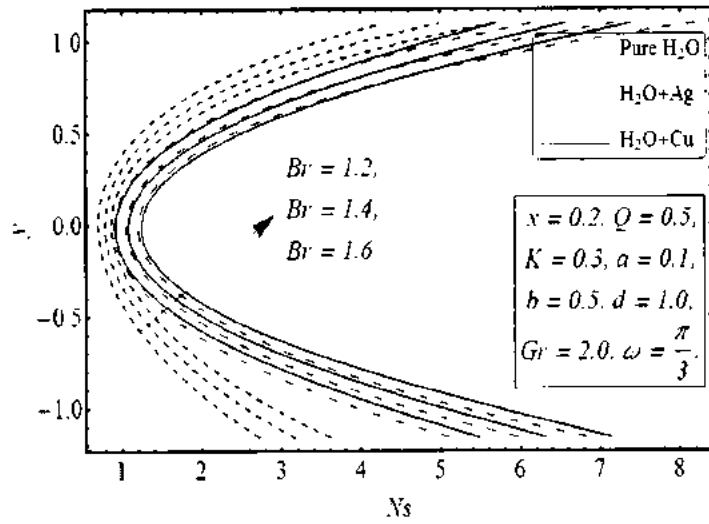
Figs. 3.4(c): Variation of velocity profile u with for different value Gr .



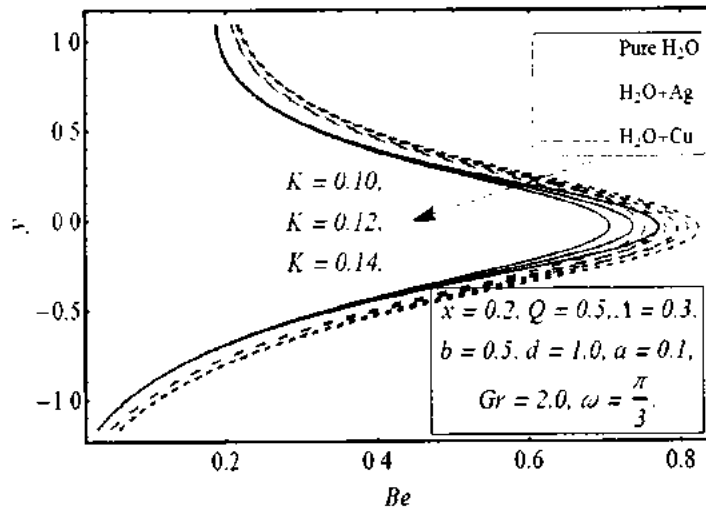
Figs. 3.5(a): Variation of entropy generation number N_s for different values of K .



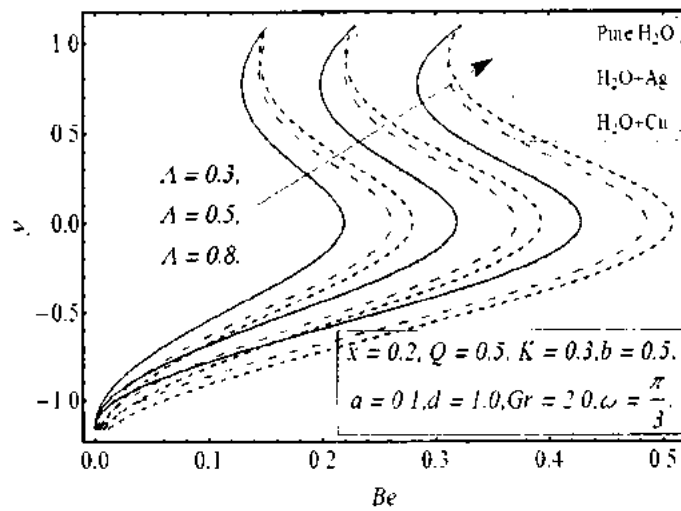
Figs. 3.5(b): Variation of entropy generation number N_s for different values of A .



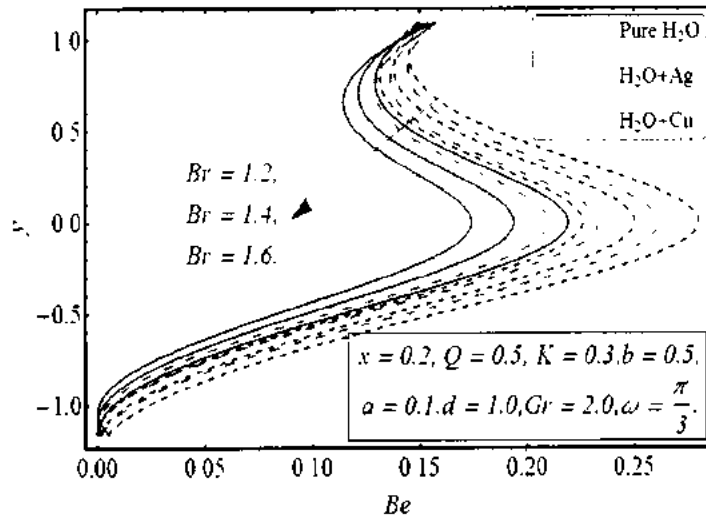
Figs. 3.5(c): Variation of entropy generation number N_s for different values of Br .



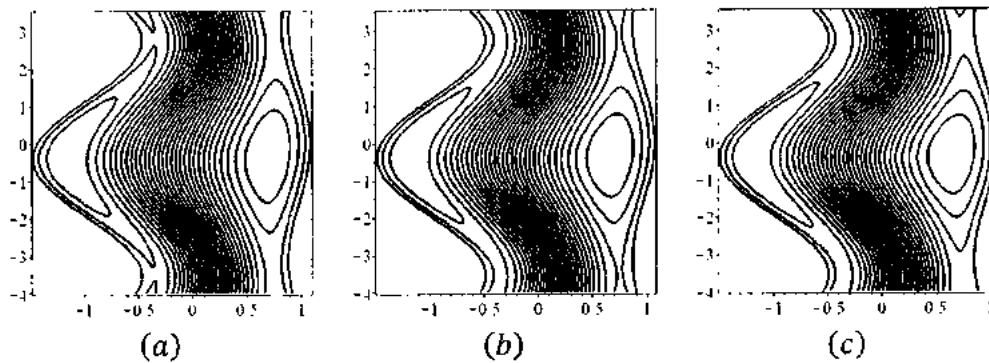
Figs. 3.6(a): Variation of Bejan number B_e for different values of K .



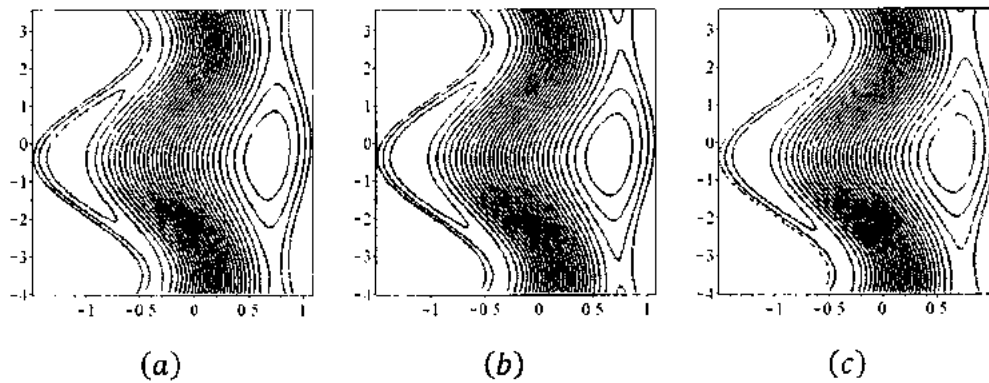
Figs. 3.6(b): Variation of Bejan number B_e for different values of A .



Figs. 3. 6(c): Variation of Bejan number Be for different values of Br .

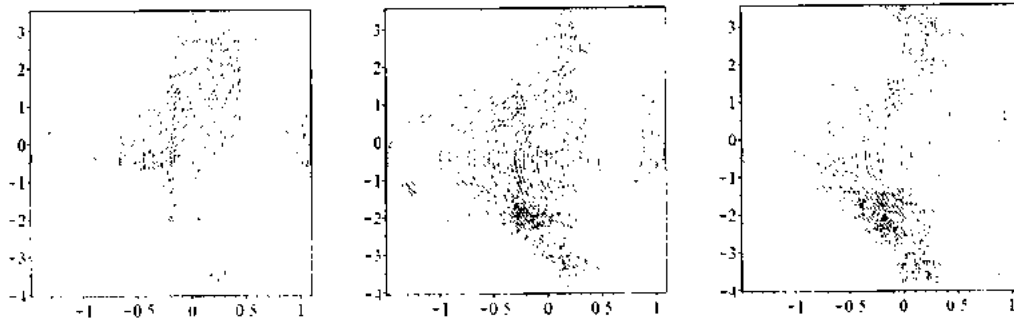


Figs.3. 7(a) – 3. 7(c): Stream lines of pure H_2O for different values of K .



Figs. 3. 8(a) – 3. 8(c): Stream lines of $H_2O + Cu$ for different values of K .

(a) for $K = 1.7$, (b) for $K = 2.4$, (c) for $K = 2.8$.



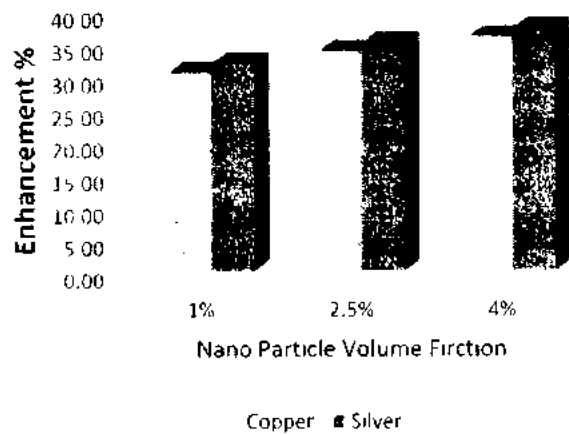
Figs. 3.9(a) – 3.9(c): Stream lines of $H_2O + Ag$ for different values of K .
 (a) for $K = 1.7$, (b) for $K = 2.4$, (c) for $K = 2.8$.

Table 3.2. Effect of volume fraction on Heat transfer coefficient.

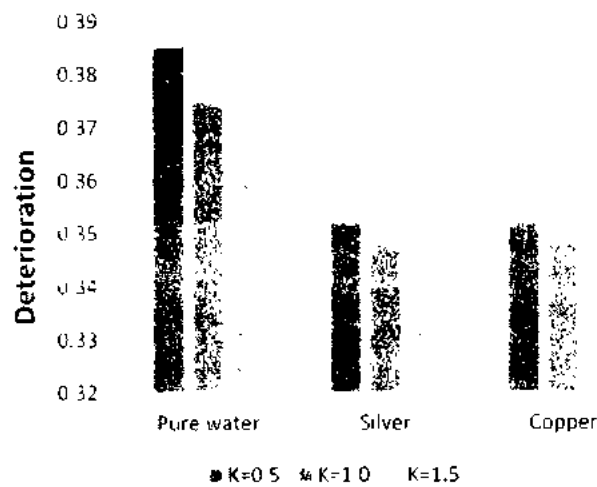
Nano particles			
Heat transfer coefficient	ϕ	Silver	Copper
	0%	0.39	0.39
	1%	0.572211	0.561904
	2.5%	0.59937	0.588702
	4%	0.619394	0.608352

Table 3.3. Effect of porosity parameter on Heat transfer coefficient.

Fluids				
Heat transfer coefficient	K	Pure water	Silver water	Copper water
	0.5	0.38519	0.35191	0.35191
	1.0	0.37463	0.34806	0.34806
	1.5	0.36072	0.342	0.342



Bar chart 3.1. The Enhancement in heat transfer rate of water by particle volume fraction.



Bar chart 3. 2. The Deterioration in heat transfer rate by porosity parameter.

In order to validate the nanofluid properties, the thermal conductivity of water was calculated from Eq. (1.14) at temperatures of 288.15 K, 298.15 K and 308.15 K. Then, the calculated data of water were compared with the reference data presented in the standard textbook [79]. As shown in Fig. 3.10, the results show that the measured data gave reasonable agreement with the reference data. Furthermore, the results also show that the uncertainty of the thermal conductivity measurement is approximately 3.5%. The thermal conductivity of Ag-water as a function of particle volume concentration and temperature compared with the reference data presented in [80] is shown in Fig. 3.11. The thermal conductivity of the nanofluid is observed to increase with an increase in temperature and particle volume concentration. The minimum enhancement for $\phi =$

0.6% and a maximum enhancement for $\phi = 0.6\%$ are observed when compared with pure water for the same temperature. Fig. 3.12 shows a comparison of calculated conductivity of nanofluids of Eq. (1.19) with the reference data presented in [80]. The viscosity of the nanofluid increases with an increase in particle volume concentration and decreases with an increase in the temperature.

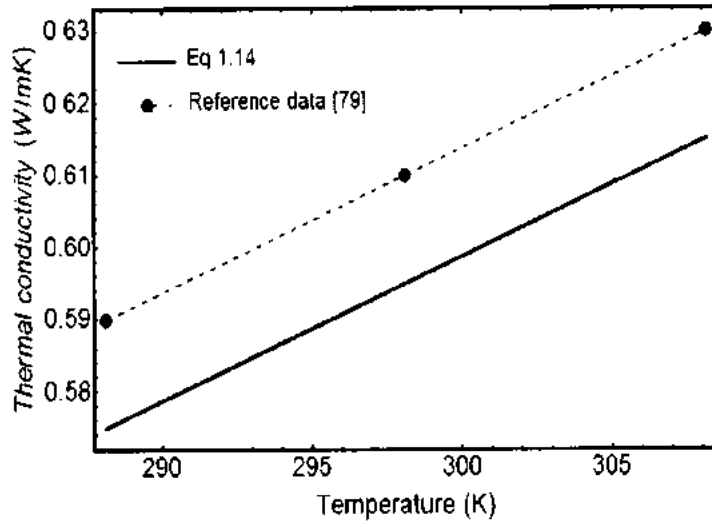


Fig. 3. 10: Comparison of the thermal conductivity between calculated data Eq. (1.14) and standard data [79].

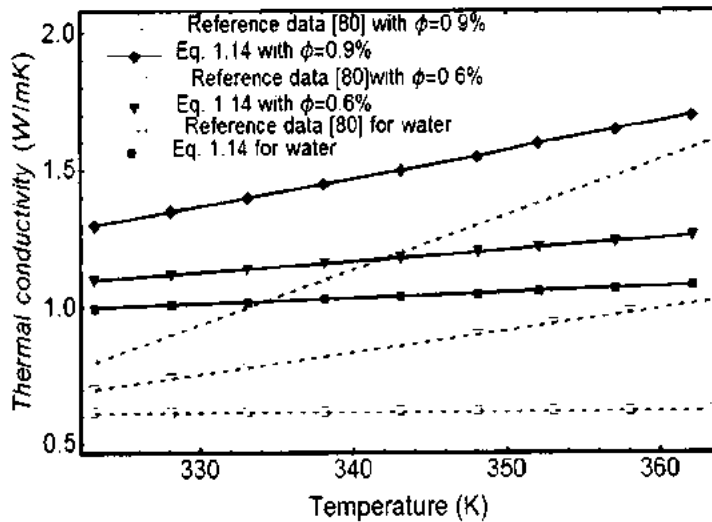


Fig. 3. 11: Comparison of the Thermal conductivity of silver-water nanofluids as a function of temperature and volume fraction between calculated data Eq. (1.14) and reference data [80].

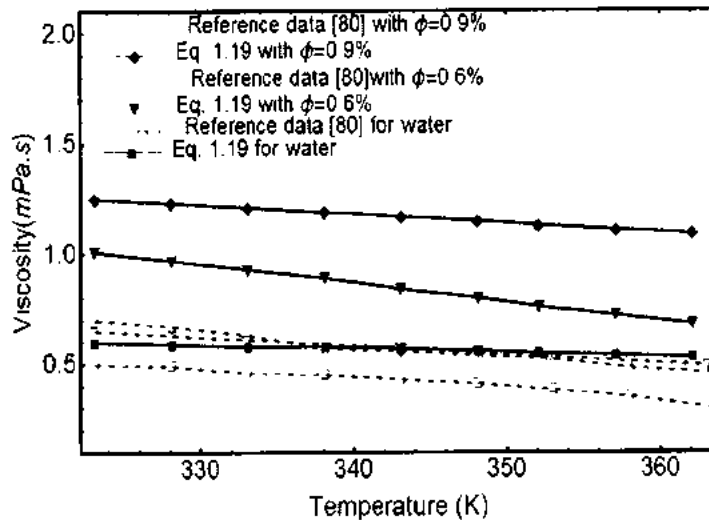


Fig. 3. 12: Comparison of the viscosity of silver-water nanofluids as a function of temperature and volume fraction between calculated data Eq. (1.19) and reference data [90].

3.4 Concluding remarks

In this chapter we discuss the Interaction of copper and silver nanoparticle with base fluid water for the peristaltic flow in porous vertical channel, key points are observed as follows.

- i. It is observed that pressure gradient is least in case of pure water whereas the effect of porosity parameter is relatively larger in the cases of copper water and silver water fluid.
- ii. It is observed that near the left wall velocity profile decreasing by increases of porosity parameter but near the right wall we noticed the opposite behavior of velocity profile.
- iii. It is observed that as increases of nano particle volume fraction the temperature also increase for both type of fluid copper water and silver water but the impact of silver water fluid is greater than the copper water fluid.
- iv. It is observed that entropy generation number is directly proportional to the Brickman number throughout the channel for all three types of fluids the impact of copper water and silver water is observed more than the pure water.
- v. It is observed that nanoparticles suspension in the base fluid is increased heat transfer rate.
- vi. It is observed that heat transfer shows deterioration effect with the enhancement of porosity parameter.

Chapter 4

Interaction of nanoparticles for the peristaltic flow in an asymmetric channel with the induced magnetic field

In this chapter, collaboration of nanoparticle copper with the base fluid water in an asymmetric channel in the presence of induced magnetic field is examined. The complexity of equations describing the flow of nanofluid is reduced through applying the low Reynolds number and long wavelength approximations. Exact solutions have been obtained from the resulting equation. The obtained expressions for velocity and temperature phenomenon are sketched through graphs. The resulting relations for pressure gradient and pressure rise are plotted for various pertinent parameters. The streamlines are drawn for some physical quantities to discuss the trapping phenomenon.

4.1 Mathematical formulation

Consider water based nanofluid flow containing copper (Cu) in vertical asymmetric channel. The mathematical description of geometry of the problem is shown in Fig. 2.1. After using the relations Eq. (2.8) and non-dimensional parameters Eq. (2.13) In the presence of induced magnetic field, the governing Eqs. (1.39), (1.41), (1.45) and (1.53) (without using bars) for nanofluid take the following form as

$$\frac{\partial u}{\partial x} + \frac{\partial v}{\partial y} = 0, \quad (4.1)$$

$$\frac{dp}{dx} = \frac{\mu_{nf}}{\mu_f} \frac{\partial^3 \psi}{\partial y^3} + \text{Re} S_1^2 \Phi_n + \frac{(\rho\beta^*)_{nf}}{(\rho\beta^*)_f} Gr\theta, \quad (4.2)$$

$$\frac{dp}{dy} = 0, \quad (4.3)$$

$$\Phi_{,y} = R_m \left(E - \frac{\partial \psi}{\partial y} \right), \quad (4.4)$$

$$\frac{\partial^2 \theta}{\partial y^2} + \theta \frac{k_f}{k_m} Q_o = 0, \quad (4.5)$$

where $\bar{\Phi} = \frac{\Phi}{H_0 d_1}$, $R_m = \sigma \mu_e d_1 c_1$, $S_1 = \frac{H_0}{c_1} \sqrt{\frac{\mu_e}{\rho}}$, putting Eq. (4.4) into Eq. (4.2), we obtain

$$\frac{dp}{dx} = \frac{\mu_{nf}}{\mu_f} \frac{\partial^3 \psi}{\partial y^3} + \text{Re} S_1^2 R_m \left(E - \frac{\partial \psi}{\partial y} \right) + \frac{(\rho \beta^*)_{nf}}{(\rho \beta^*)_f} Gr \theta. \quad (4.6)$$

Taking derivative of Eq. (4.6) with respect to y , we get

$$\frac{\mu_{nf}}{\mu_f} \frac{\partial^4 \psi}{\partial y^4} + \text{Re} S_1^2 R_m \left(-\frac{\partial^2 \psi}{\partial y^2} \right) + \frac{(\rho \beta^*)_{nf}}{(\rho \beta^*)_f} Gr \frac{\partial \theta}{\partial y} = 0. \quad (4.7)$$

The non-dimensional boundaries are

$$\psi = \frac{F}{2}, \quad \frac{\partial \psi}{\partial y} = -1, \quad \text{at } y = h_1. \quad (4.8)$$

$$\psi = -\frac{F}{2}, \quad \frac{\partial \psi}{\partial y} = -1, \quad \text{at } y = h_2. \quad (4.9)$$

$$\theta = 0 \quad \text{at } y = h_1, \quad \theta = 1 \quad \text{at } y = h_2, \quad (4.10)$$

$$\Phi = 0 \quad \text{at } y = h_1, \quad \Phi = 0 \quad \text{at } y = h_2. \quad (4.11)$$

The pressure rise Δp in non-dimensional form is defined in Eq. (2.26), axial induced magnetic h_x and current density J_z in non-dimensional form are defined as

$$h_x = \frac{\partial \Phi}{\partial y}, \quad (4.12)$$

$$J_z = -\frac{\partial h_x}{\partial y}. \quad (4.13)$$

In this chapter conductivity of nanofluid and the effective viscosity of nanofluid given in Eqs. (1.12) and (1.10) have been used, thermal physical properties of water and nanoparticles at defined in table 3.1.

4.2 Solution of the problem

The exact solutions of the Eqs. (4.4), (4.5) and (4.7) corresponding to associative boundary conditions given in Eqs. (4.8) – (4.11) are calculates as

Integrating twice Eq. (4.5) with respect to y

$$\theta(y) = C_{31} \cos[C_{29}y] + C_{30} \sin[C_{29}y], \quad (4.14)$$

for simplicity we choose $C_{29} = \frac{\sqrt{k_l} \sqrt{Q_0}}{\sqrt{k_m}}$, C_{30} and C_{31} are constant of integration

which are calculating by using the boundary condition (4.10) as

$$C_{30} = -\cos[C_{29}h_1] \csc[C_{29}(h_1 - h_2)], \quad (4.15)$$

$$C_{31} = \csc[C_{29}(h_1 - h_2)] \sin[C_{29}h_1], \quad (4.16)$$

Similarly integrating Eq. (4.7) with respect to y we get

$$\begin{aligned} \psi(y) = C_{37} + yC_{38} + \frac{((C_{35}) \cosh[C_{33}y] + (C_{36}) \sinh[C_{33}y])}{C_{33}^2} + \\ C_{34} (-\cos[yC_{29}]C_{30} + \sin[yC_{29}]C_{31}), \end{aligned} \quad (4.17)$$

where the constants $C_{32} - C_{34}$ are defined as

$$C_{32} = ReS_1^2 R_m, \quad C_{33} = \frac{\sqrt{C_{32}}}{\sqrt{C_4}}, \quad C_{34} = \frac{C_6}{C_{29}(C_4 C_{29}^2 + C_{32})}. \quad (4.18)$$

Using the boundary conditions (4.8) – (4.9) we obtain the constants of integration as

$$C_{35} = \frac{
\begin{aligned}
& \left(C_{33} \operatorname{csch} \left[\frac{1}{2} C_{33} (h_1 - h_2) \right] C_{33} \right. \\
& \left(2 \sin \left[\frac{1}{2} C_{29} (h_1 - h_2) \right] C_{29} \right. \\
& \left(\cos \left[\frac{1}{2} C_{29} (h_1 + h_2) \right] C_{30} \right) \\
& \left. - \sin \left[\frac{1}{2} C_{29} (h_1 + h_2) \right] C_{31} \right) \\
& - C_{34} \left(\begin{aligned} & -\sinh [C_{33} h_1] + \sinh [C_{33} h_2] + \\ & \cosh [C_{33} h_1] C_{33} (h_1 - h_2) \end{aligned} \right) \\
& - \left(\begin{aligned} & \cosh [C_{33} h_1] - \\ & \cosh [C_{33} h_2] \end{aligned} \right) \\
& C_{33} F + \\
& \left(h_1 + C_{31} C_{34} \left(\begin{aligned} & -\sin [C_{29} h_1] + \sin [C_{29} h_2] \\ & + \cos [C_{29} h_1] C_{29} (h_1 - h_2) \end{aligned} \right) + \right) \\
& \left. C_{30} C_{34} \left(\begin{aligned} & \cos [C_{29} h_1] - \cos [C_{29} h_2] + \\ & \sin [C_{29} h_1] C_{29} (h_1 - h_2) \end{aligned} \right) - h_2 \right)
\end{aligned}
}{
\begin{aligned}
& 2 \left(\begin{aligned} & -2 \sinh \left[\frac{1}{2} C_{33} (h_1 - h_2) \right] + \\ & \cosh \left[\frac{1}{2} C_{33} (h_1 - h_2) \right] C_{33} (h_1 - h_2) \end{aligned} \right)
\end{aligned}
} \tag{4.19}$$

$$C_{36} = \frac{\begin{pmatrix} Csch\left[\frac{1}{2}C_{33}(h_1 - h_2)\right]C_{33} \\ 2\left(\frac{\cosh[C_{33}h_1] - 1}{\cosh[C_{33}h_2] - 1}\right)\sin\left[\frac{1}{2}C_{29}(h_1 - h_2)\right] \\ C_{29}C_{34}\begin{pmatrix} \cos\left[\frac{1}{2}C_{29}(h_1 + h_2)\right]C_{30} \\ -\sin\left[\frac{1}{2}C_{29}(h_1 + h_2)\right]C_{31} \end{pmatrix} \\ +C_{33}C_{31}C_{34}\begin{pmatrix} -\left(\frac{\sin[C_{29}h_1] - 1}{\sin[C_{29}h_2] - 1}\right)\left(\frac{\sinh[C_{33}h_1] - 1}{\sinh[C_{33}h_2] - 1}\right) + \\ \left(\frac{\cos[C_{29}h_2]\sinh[C_{33}h_1] - 1}{\cos[C_{29}h_1]\sinh[C_{33}h_2] - 1}\right)C_{29}(h_1 - h_2) \end{pmatrix} \end{pmatrix}}{\left(2\left(-2\sinh\left[\frac{1}{2}C_{33}(h_1 - h_2)\right] + \cosh\left[\frac{1}{2}C_{33}(h_1 - h_2)\right]C_{33}(h_1 - h_2)\right)\right)}, \quad (4.20)$$

$$C_{37} = \frac{\left(\frac{F}{2} + (\cos[C_{29}h_1]C_{30} - \sin[C_{29}h_1]C_{31})C_{34} + C_{29}\left(\frac{\sin[C_{29}h_1] - 1}{\sin[C_{29}h_2] - 1}\right)C_{30} + \left(\frac{\cos[C_{29}h_1] - 1}{\cos[C_{29}h_2] - 1}\right)C_{31}\right)C_{34}\left(\frac{\sinh[C_{33}h_1] - 1}{\cosh[C_{33}h_1]C_{33}h_1}\right)}{(\cosh[C_{33}h_1] - \cosh[C_{33}h_2])C_{33}}, \quad (4.21)$$

$$C_{1x} = \left(\begin{array}{c} \frac{1}{-2 + \coth \left[\frac{1}{2} C_{33} (h_1 - h_2) \right] C_{33} (h_1 - h_2)} \\ 2 + C_{29} \left(\left(\frac{\sin [C_{29} h_1] +}{\sin [C_{29} h_2]} \right) C_{30} + \left(\frac{\cos [C_{29} h_1] +}{\cos [C_{29} h_2]} \right) C_{31} \right) C_{34} + \\ \coth \left[\frac{1}{2} C_{33} (h_1 - h_2) \right] C_{33} \\ \left(F + \left(\frac{\cos [C_{29} h_1] -}{\cos [C_{29} h_2]} \right) C_{30} C_{34} \right) \\ - \left(\frac{\sin [C_{29} h_1] -}{\sin [C_{29} h_2]} \right) C_{31} C_{34} \end{array} \right). \quad (4.22)$$

For finding the magnetic force function integrating two time of Eq. (4.4) with respect to y we get

$$\Phi(y) = \left(\begin{array}{c} \sin [y C_{29}] C_{39} + \cos [y C_{29}] C_{40} - \sinh [y C_{33}] C_{41} - \\ \cosh [y C_{33}] C_{42} + C_{43} + y C_{44} + \frac{1}{2} E y^2 R_m - \frac{1}{2} y^2 C_{38} R_m \end{array} \right), \quad (4.23)$$

where the constants

$$C_{39} = \frac{C_{30} C_{34} R_m}{C_{29}}, \quad C_{40} = \frac{C_{31} C_{34} R_m}{C_{29}}, \quad C_{41} = \frac{C_{35} R_m}{C_{33}^3}, \quad C_{42} = \frac{\cosh [y C_{33}] C_{36} R_m}{C_{33}^3}. \quad (4.24)$$

Using the boundary conditions (4.11) in Eq. (4.23) obtain the constant of integration as

$$C_{43} = -\frac{1}{h_1 - h_2} \left(\begin{array}{c} \left(\begin{array}{c} \sin [C_{29} h_1] C_{39} + \cos [C_{29} h_1] C_{40} - \\ \sinh [C_{33} h_1] C_{41} - \cosh [C_{33} h_1] C_{42} + \\ \frac{1}{2} E h_1^2 R_m - \frac{1}{2} C_{38} h_1^2 R_m \end{array} \right) + \\ \left(\begin{array}{c} \sin [C_{29} h_2] C_{39} + \cos [C_{29} h_2] C_{40} - \\ \sinh [C_{33} h_2] C_{41} - \cosh [C_{33} h_2] C_{42} + \\ \frac{1}{2} E h_2^2 R_m - \frac{1}{2} C_{38} h_2^2 R_m \end{array} \right) \end{array} \right), \quad (4.25)$$

$$C_{44} = -\frac{1}{2(h_1 - h_2)} \begin{pmatrix} 2 \sin [C_{29} h_1] C_{39} - 2 \sin [C_{29} h_2] C_{39} + \\ 2 \cos [C_{29} h_1] C_{40} - 2 \cos [C_{29} h_2] C_{40} - \\ 2 \sinh [C_{33} h_1] C_{41} + 2 \sinh [C_{33} h_2] C_{41} - \\ 2 \cosh [C_{33} h_1] C_{42} + 2 \cosh [C_{33} h_2] C_{42} + \\ E h_1^2 R_m - C_{38} h_1^2 R_m - E h_2^2 R_m + C_{38} h_2^2 R_m \end{pmatrix}. \quad (4.26)$$

The mean volume flow rate Q over one period is given in Eq. (2.31) and pressure gradient dp/dx , axial induced magnetic h_x and current density J_z are obtained as

$$\begin{aligned} & (0.5 - 0.25C_{33}F)(\cosh(C_{33}h_1 - 2A_5h_2) - \sinh(C_{33}h_1 - 2C_{33}h_2)) + \\ & (-0.25C_{33}F - 0.5)(\sinh(2C_{33}h_1 - C_{33}h_2) + \cosh(2C_{33}h_1 - C_{33}h_2)) + \\ & (0.25C_{33}F + 1.5)(\sinh(C_{33}h_1) + \cosh(C_{33}h_1)) + \\ \frac{dp}{dx} = & \frac{(0.25C_{33}F - 1.5)(\sinh(C_{33}h_2) + \cosh(C_{33}h_2))}{(\sinh(C_{33}h_1) + 1. \cosh(C_{33}h_1) - \sinh(C_{33}h_2) - \\ & \cosh(C_{33}h_2))(-0.5C_{33}h_1 \sinh(C_{33}h_1 - C_{33}h_2) + \\ & 0.5C_{33}h_2 \sinh(C_{33}h_1 - C_{33}h_2) + \cosh(C_{33}h_1 - C_{33}h_2) - 1)} \end{aligned}, \quad (4.27)$$

$$h_x = \cos[\gamma C_{29}] C_{29} C_{39} - \sin[\gamma C_{29}] C_{29} C_{40} - \cosh[\gamma C_{33}] C_{33} C_{41} - \sinh[\gamma C_{33}] C_{33} C_{42} + C_{44} + E\gamma R_m - \gamma C_{38} R_m, \quad (4.28)$$

$$J_z = \sin[\gamma C_{29}] C_{29}^2 C_{39} + \cos[\gamma C_{29}] C_{29}^2 C_{40} + \sinh[\gamma C_{33}] C_{33}^2 C_{41} + \cosh[\gamma C_{33}] C_{33}^2 C_{42} - ER_m + C_{38} R_m. \quad (4.29)$$

4.3 Results and discussion

In this section, the impacts of various physical parameters, on the pressure rise, pressure gradient, temperature, axial induced magnetic field h_x , current density j_z and the velocity profiles for copper nanofluid and pure water fluid with the assistance of graphical results showed in Figs. 4.1(a) - 4.6(b). The expression for the pressure rise is ascertained numerically utilizing a mathematics software. The trapping phenomena in the Figs. 4.7(a) - 4.9(d).

Fig. 4.1(a) expresses the impacts of ϕ on the pressure rise. It is seen here that pressure rise is an expanding capacity with the expansions of ϕ all through in the retrograde pumping region. In the Figs. 4.1(b) - 4.1(c), it is measured that Δp gets diminished with the expanding impacts of S_1 and R_m for both copper water and pure water cases in the retrograde locale. From Fig. 4.2(a), it can be seen that pressure gradient diminishes as nanoparticle volume fraction is increased. The variation of the S_1 and R_m

have the same conduct on pressure gradient graph, the both show expanding pattern as parameters worth builds see Figs. 4.2(b) and 4.2(c) for both the cases, copper-water and pure water. The contrast between copper nanofluid and pure water fluid is that the copper nanofluid contains more pressure than the pure water. it can see the effect of parameters local temperature Grashof number Gr on the variation of dp/dx from Fig. 4.2(d), at the point when every single other parameter are kept settled. It is noticed that pressure gradient diminishes as Gr increments. o as to see the contrast between copper nanofluid and pure water, constructed the table. 4.1. Grashof number Gr and other flow parameters are altered as $d = 1.0$, $a = 0.2$., $Q_0 = 0.3$, $R_m = 1.0$, $b = 0.4$, $\omega = \pi/6$, $Re = 1.0$. From table.4.2 it has watch that the copper water and unadulterated water, both give us diminishing estimations of pressure gradient as expand the estimation of Gr . Fig. 4.3(a) presents the impacts of temperature θ for the distinctive estimations of ϕ one can see that as expansion the ϕ , temperature additionally increments, exhibited the Fig. 4.3(b) to demonstrate the conduct of temperature profile with the impact of heat generation parameter Q_0 the temperature θ increments with an expansion of Q_0 for both copper-water and pure water cases. The distinction between these can be seen from the table 4.3. It is seen from Fig. 4.4(a) that velocity profile diminishes close to both dividers of direct however increments in the focal point of the divert with expansion in the estimation of ϕ . To see the conduct of velocity profile u for the instances of copper water and unadulterated water with the variation of R_m and S_1 showed in the Figs. 4.4(b) and 4.4(c). Velocity profile u increments close to the dividers of diverts however amidst the channel, velocity diminishes by expansion in R_m and S_1 separately.

Fig.4.4(d) is drawn to acquire the variation of u for differing the magnitude of the parameters Gr . The Fig.4.4(d) delineates that in the event of copper nanofluid there are demonstrated three stages in the channel *i.e.*, left divider, focal point of divider and right divider, be that as it may, for the pure water case there are two stages *i.e.*, from left to the middle, and from focus to one side. It can watched that if there should be an occurrence of copper water velocity is reductions in the first and third stage *i.e.*, close to one side divider and right divider separately with an expansion of Gr . In the focal point of channel, the estimation of velocity goes to the most extreme level. In the event of pure water, velocity profile increments from the left mass of channel to the focal point of channel on expansion of Gr . Yet, inverse conduct is seen from focus of the

channel to the right divider. Breaking down this contrast between copper water and unadulterated water numerically, it has drawn a table 4.4. . Fig.4.4(e) talks about the practices of Q_0 on u versus y for both, copper water and unadulterated water. One can see that velocity profile does not change to awesome degree as contrast with copper water liquid. It can be seen that velocity is expanding by expansion in Q_0 . Figs. 4.5(a) and 4.5(b) demonstrate the variations of magnetic Reynolds and Stommer's number on an axial induced magnetic field h_x versus y . It is fascinating to note that in the half district of the channel, the induced magnetic field is in one course. Notwithstanding, it is the other way in the other half district of the channel. The Fig. 4.5(a) shows that magnitude of h_x increases R_m increases from divider h_1 to the center of channel, yet the diminishing pattern is seen in the other portion of the channel keeping R_m increased. Then again, the impacts of S_1 on h_x are very inverse in examination to R_m . It has likewise displayed the tables 4.5 and 4.6, to demonstrate this distinction in copper nanofluid and pure water. In Figs. 4.6(a) and 4.6(b) the current density j_z is appeared as an element of y for three distinct estimations of R_m and S_1 both of these figures are of of parabolic type, In the both figures the magnitude of j_z declines as the estimations of R_m and S_1 increase. Figs. 4.7(a) – 4.7(d) demonstrates the streamlines for the different estimations of the parameter ϕ . It is noticed that bolus turns out to be huge when it give more noteworthy qualities to the value of ϕ . Fig 4.7(a) – 4.7(d) is drawn for the nano copper fluid it can be see that bolus turns out to be small when it give more noteworthy estimations of Gr where one can saw that from Fig.4.8(a) – 4.8(d) on account of pure water, number of catching bolus is diminishing with expanding and in addition size of bolus additionally diminishes.

Table 4.1. Numerical values of pressure gradient dp / dx for different values of Gr .

x	$Gr = 4.0$		$Gr = 6.0$		$Gr = 8.0$	
	$Cu + H_2O$ $\phi = 0.2$	H_2O $\phi = 0.0$	$Cu + H_2O$ $\phi = 0.2$	H_2O $\phi = 0.0$	$Cu + H_2O$ $\phi = 0.2$	H_2O $\phi = 0.0$
-4.0	-5.50196	-5.6484	-4.0911	-4.1563	-5.7369	-6.0299
-3.5	-6.1127	-6.2600	-4.4551	-4.5206	-6.3443	-6.6389
-3.0	-5.5339	-5.6805	-4.1104	-4.1756	-5.7687	-6.0618
-2.5	-4.3405	-4.4844	-3.3728	-3.4368	-4.5855	-4.8733
-2.0	-3.3217	-3.4599	-2.7004	-2.7619	-3.5852	-3.8616
-1.5	-2.6873	-2.8156	-2.2481	-2.3053	-2.9770	-3.2337
-1.0	-2.3576	-2.4735	-1.9950	-2.0468	-2.6757	-2.9073
-0.5	-2.2332	-2.3404	-1.8940	-1.9421	-2.5687	-2.7832
0.0	-2.2633	-2.3730	-1.9188	-1.9680	-2.5940	-2.8133
0.5	-2.4612	-2.5821	-2.0764	-2.1304	-2.7682	-3.0101
1.0	-2.9002	-3.0330	-2.4039	-2.4630	-3.1786	-3.4442
1.5	-3.6871	-3.8281	-2.9476	-3.0103	-3.9422	-4.2240
2.0	-4.8332	-4.9784	-3.6824	-3.7470	-5.0731	-5.3636
2.5	-5.8966	-6.0437	-4.3272	-4.3926	-6.1292	-6.4234
3.0	-5.9987	-6.1459	-4.3878	-4.4532	-6.2308	-6.5252
3.5	-5.0336	-5.1793	-3.8061	-3.8709	-5.2718	-5.5632
4.0	-3.8531	-3.9950	-3.0574	-3.1205	-4.1051	-4.3888

Table 4. 2. Numerical values of temperature θ for different values of Q_0 .

y	$Q_0 = 0.4$		$Q_0 = 0.6$		$Q_0 = 0.8$	
	$Cu + H_2O$	H_2O	$Cu + H_2O$	H_2O	$Cu + H_2O$	H_2O
	$\phi = 0.2$	$\phi = 0.0$	$\phi = 0.2$	$\phi = 0.0$	$\phi = 0.2$	$\phi = 0.0$
-1.21	1.0000	1.0000	1.0000	1.0000	1.0000	1.0000
-0.81	0.8685	0.8583	0.9098	0.8866	0.9582	0.9181
-0.41	0.7180	0.7029	0.7797	0.7449	0.8536	0.7924
-0.01	0.5518	0.5363	0.6156	0.5795	0.6931	0.6288
0.38	0.3734	0.3612	0.4245	0.3955	0.4871	0.4351
0.78	0.1869	0.1802	0.2148	0.1989	0.2492	0.2206

Table 4. 3. Numerical values of velocity u for different values of Gr .

y	$Gr = 2.0$		$Gr = 4.0$		$Gr = 6.0$	
	$Cu + H_2O$	H_2O	$Cu + H_2O$	H_2O	$Cu + H_2O$	H_2O
	$\phi = 0.2$	$\phi = 0.0$	$\phi = 0.2$	$\phi = 0.0$	$\phi = 0.2$	$\phi = 0.0$
-1.21	-1.0000	-1.0000	-1.0000	-1.0000	-1.0000	-1.0000
-0.91	-0.5097	-0.2750	-0.7042	-0.2347	-0.8986	-0.1945
-0.61	0.1199	0.1929	0.1067	0.2526	0.0934	0.3123
-0.31	0.6023	0.4379	0.8184	0.4895	1.0345	0.5412
-0.01	0.7596	0.4853	1.0525	0.5039	1.3454	0.5225
0.28	0.5395	0.3540	0.6970	0.3261	0.8546	0.2981
0.58	0.0202	0.0569	-0.0836	-0.0104	-0.1876	-0.0777
0.88	-0.5966	-0.3996	-0.8635	-0.4696	-1.1304	-0.5396

Table 4.4. Numerical values of velocity u for different values of Q_0 .

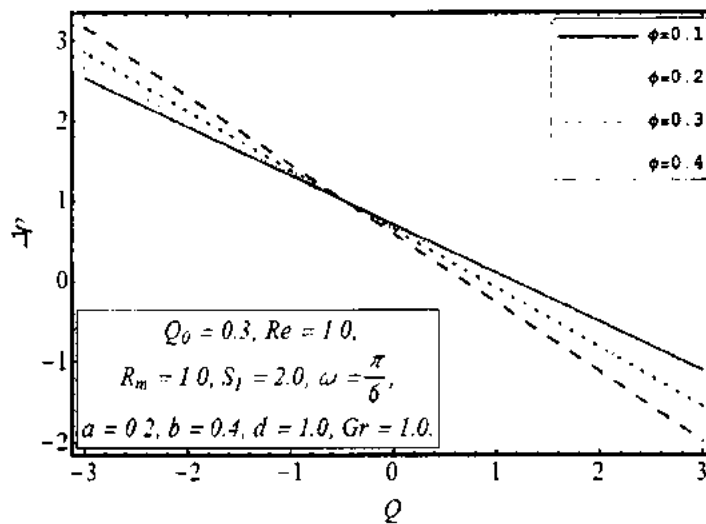
y	$Q_0 = 0.4$		$Q_0 = 0.6$		$Q_0 = 0.8$	
	$Cu + H_2O$	H_2O	$Cu + H_2O$	H_2O	$Cu + H_2O$	H_2O
	$\phi = 0.2$	$\phi = 0.0$	$\phi = 0.2$	$\phi = 0.0$	$\phi = 0.2$	$\phi = 0.0$
-1.21	-1.0000	-1.0000	-1.0000	-1.0000	-1.0000	-1.0000
-0.91	-0.1149	-0.0980	-0.1072	-0.1046	-0.0569	-0.1153
-0.61	0.2039	0.2545	0.2269	0.2566	0.2992	0.2581
-0.31	0.2875	0.3575	0.3123	0.3675	0.3634	0.3811
-0.01	0.2796	0.3354	0.2910	0.3465	0.2912	0.3629
0.28	0.2272	0.2307	0.2181	0.2357	0.1678	0.2439
0.58	0.1041	0.0347	0.0782	0.0293	0.0065	0.0229
0.88	-0.2130	-0.3219	-0.2405	-0.3340	-0.2923	-0.3506

Table 4.5. Numerical values of axial induced magnetic field h_z for different values of R_m .

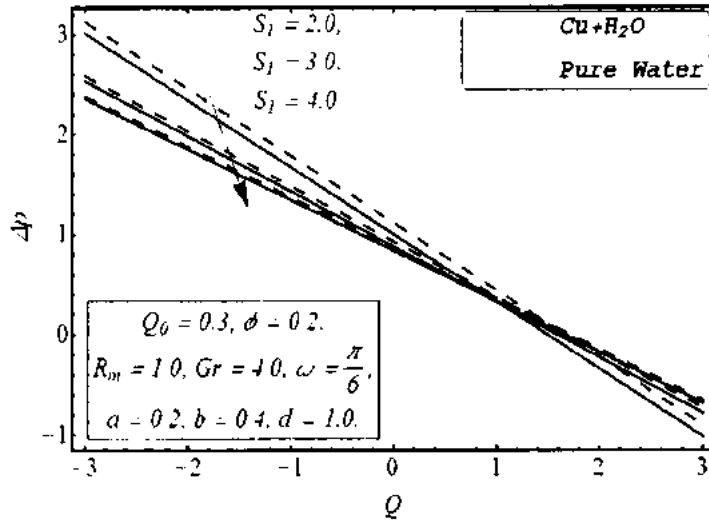
y	$R_m = 1.0$		$R_m = 2.0$		$R_m = 3.0$	
	$Cu + H_2O$	H_2O	$Cu + H_2O$	H_2O	$Cu + H_2O$	H_2O
	$\phi = 0.2$	$\phi = 0.0$	$\phi = 0.2$	$\phi = 0.0$	$\phi = 0.2$	$\phi = 0.0$
-1.21	0.000	0.0000	0.0000	0.0000	0.0000	0.0000
-0.91	0.3242	0.1662	0.3058	0.1570	0.2860	0.1471
-0.61	0.3976	0.1847	0.3650	0.1700	0.3308	0.1545
-0.31	0.2485	0.1068	0.2249	0.0969	0.2004	0.0866
-0.01	-0.0153	-0.0116	-0.0130	-0.0098	-0.0109	-0.0081
0.28	-0.2715	-0.1244	-0.2446	-0.1119	-0.2171	-0.0992
0.58	-0.4000	-0.1868	-0.3674	-0.1721	-0.3333	-0.1565
0.88	-0.3010	-0.1487	-0.2860	-0.1421	-0.2695	-0.1347

Table 4.6. Numerical values of axial induced magnetic field h_x for different values of R_m .

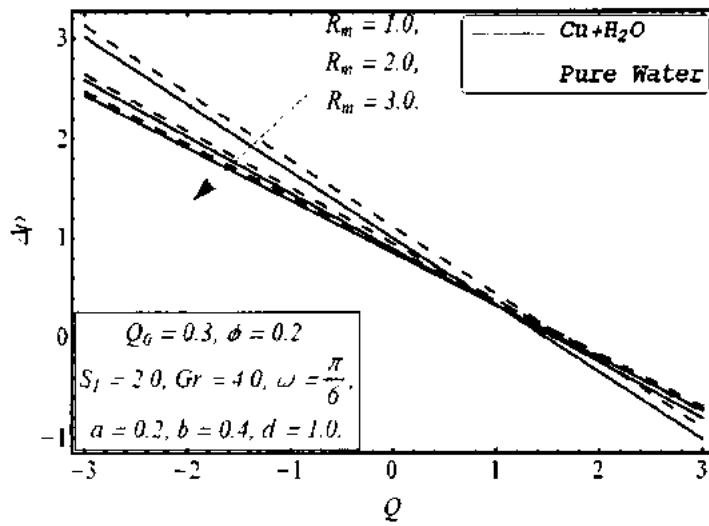
y	$R_m = 1.0$		$R_m = 2.0$		$R_m = 3.0$	
	$Cu + H_2O$ $\phi = 0.2$	H_2O $\phi = 0.0$	$Cu + H_2O$ $\phi = 0.2$	H_2O $\phi = 0.0$	$Cu + H_2O$ $\phi = 0.2$	H_2O $\phi = 0.0$
-1.21	0.000	0.0000	0.0000	0.0000	0.0000	0.0000
-0.91	0.3242	0.1662	0.3058	0.1570	0.2860	0.1471
-0.61	0.3976	0.1847	0.3650	0.1700	0.3308	0.1545
-0.31	0.2485	0.1068	0.2249	0.0969	0.2004	0.0866
-0.01	-0.0153	-0.0116	-0.0130	-0.0098	-0.0109	-0.0081
0.28	-0.2715	-0.1244	-0.2446	-0.1119	-0.2171	-0.0992
0.58	-0.4000	-0.1868	-0.3674	-0.1721	-0.3333	-0.1565
0.88	-0.3010	-0.1487	-0.2860	-0.1421	-0.2695	-0.1347



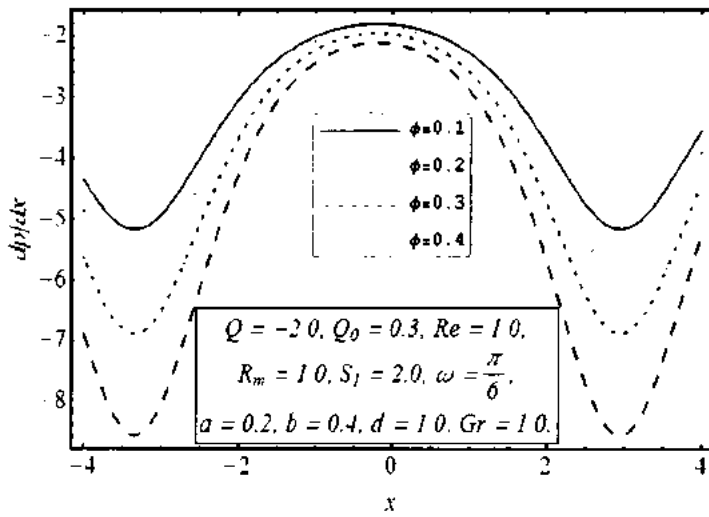
Figs. 4.1(a). Variation of pressure rise Δp for flow parameter ϕ .



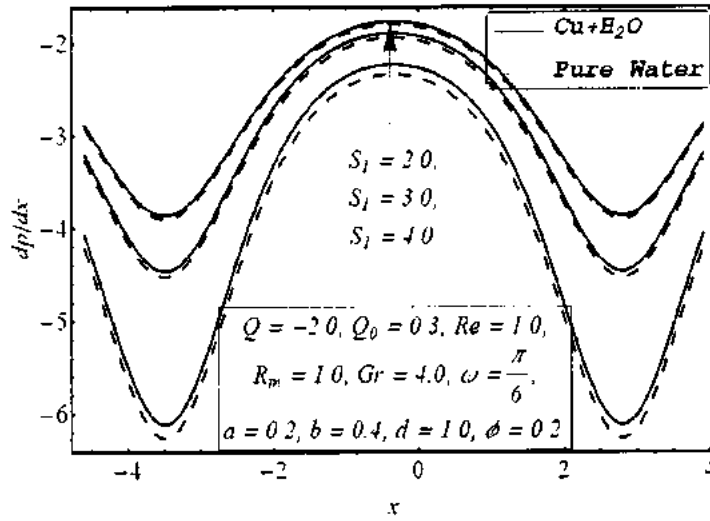
Figs. 4. 1(b). Variation of pressure rise Δp for flow parameter S_1 .



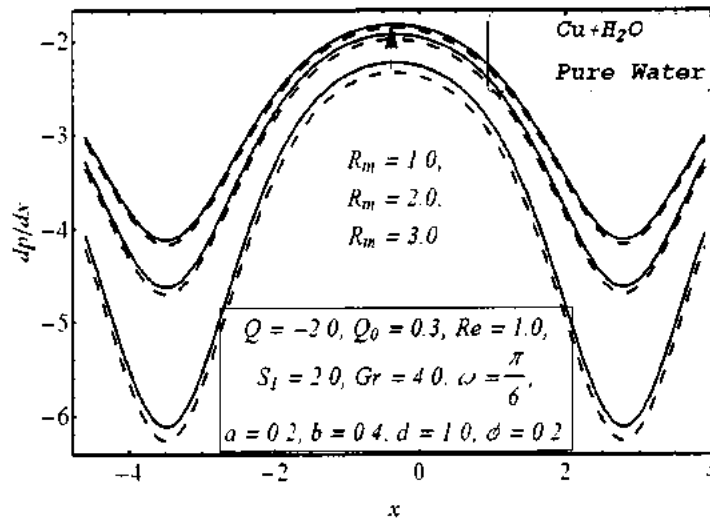
Figs. 4. 1(c). Variation of pressure rise Δp for flow parameter R_m .



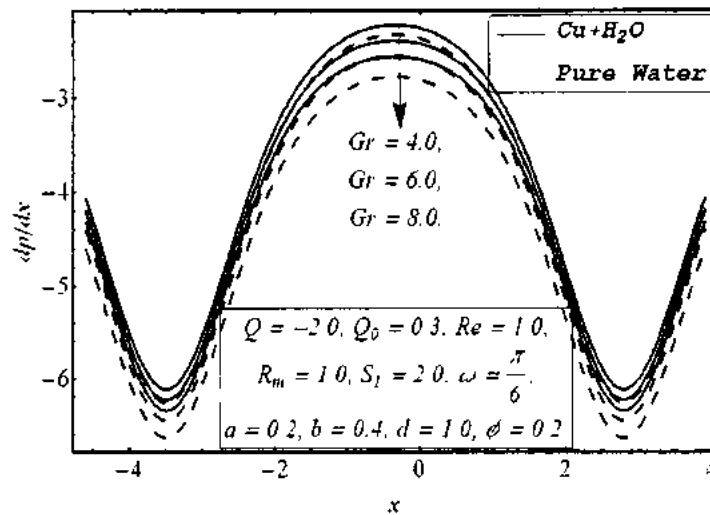
Figs. 4. 2(a). Variation of pressure gradient dp/dx for flow parameter ϕ .



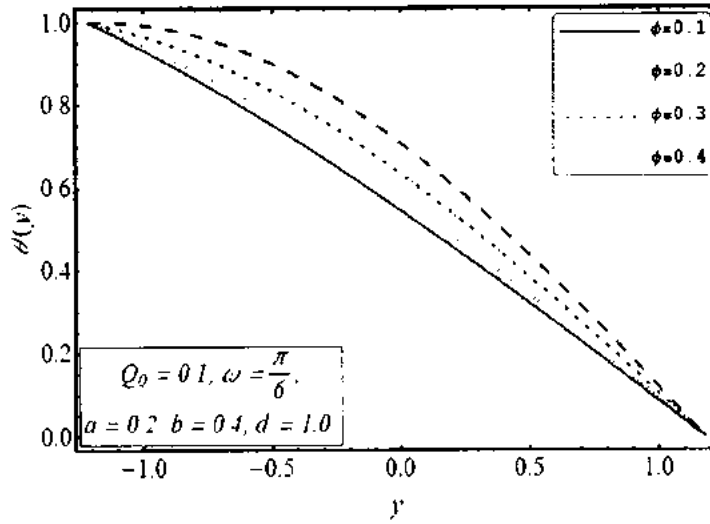
Figs. 4.2(b). Variation of pressure gradient dp/dx for flow parameter S_1 .



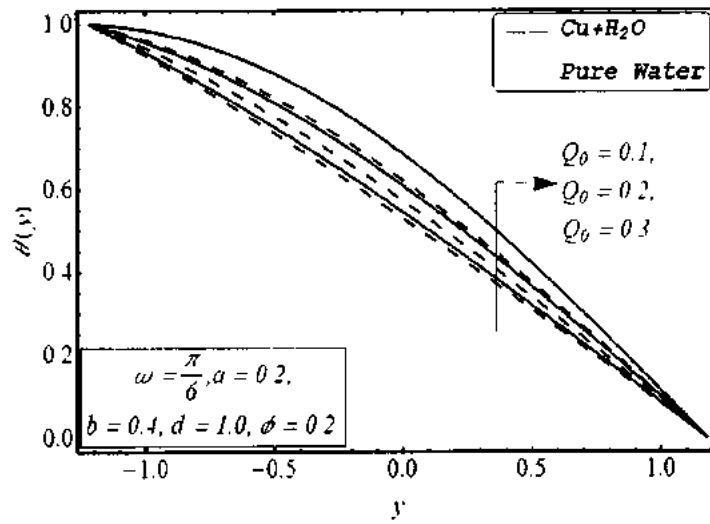
Figs. 4.2(c). Variation of pressure gradient dp/dx for flow parameter R_m .



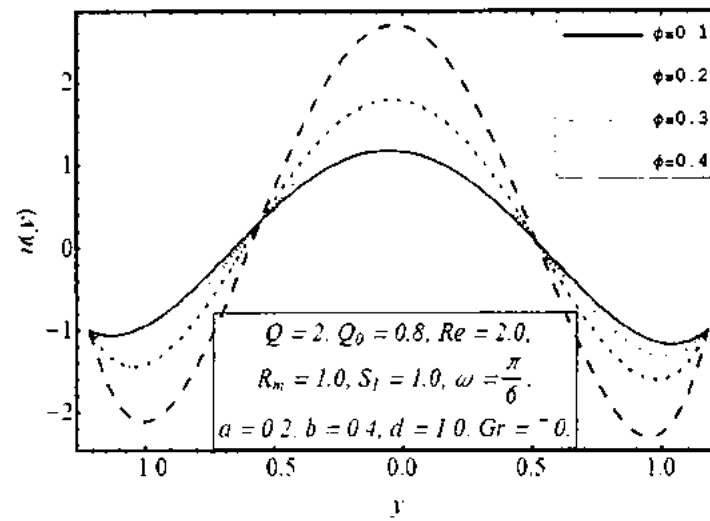
Figs. 4.2(d). Variation of pressure gradient dp/dx for flow parameter Gr .



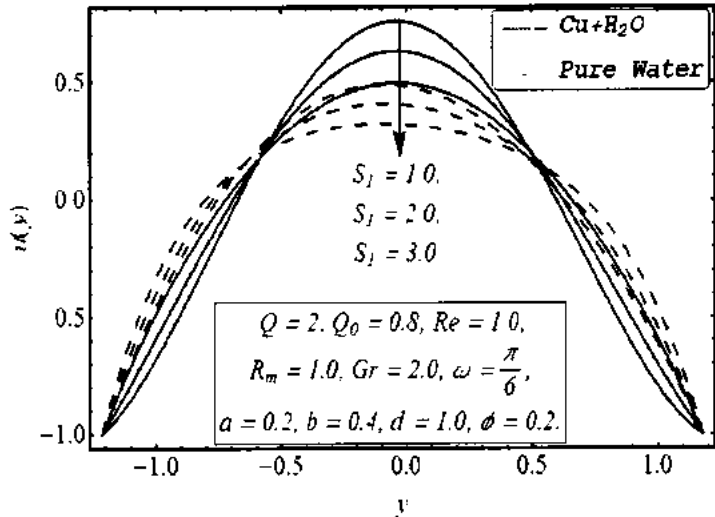
Figs. 4.3(a). Variation of temperature profile θ for flow parameters ϕ .



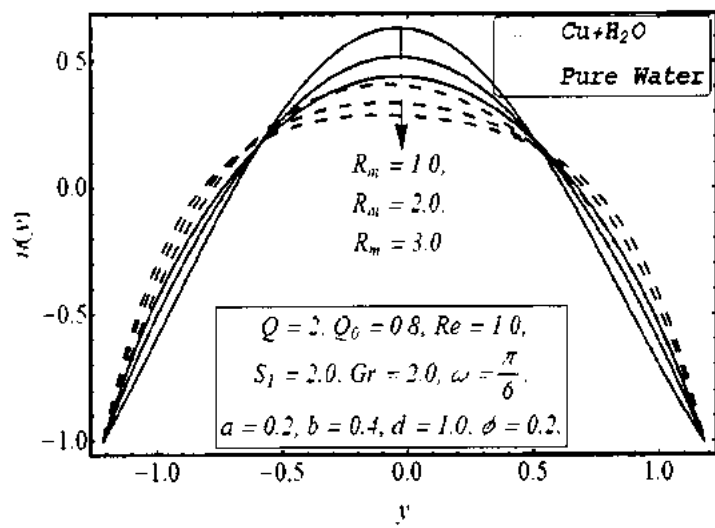
Figs. 4.3(b). Variation of temperature profile θ for flow parameters Q_0 .



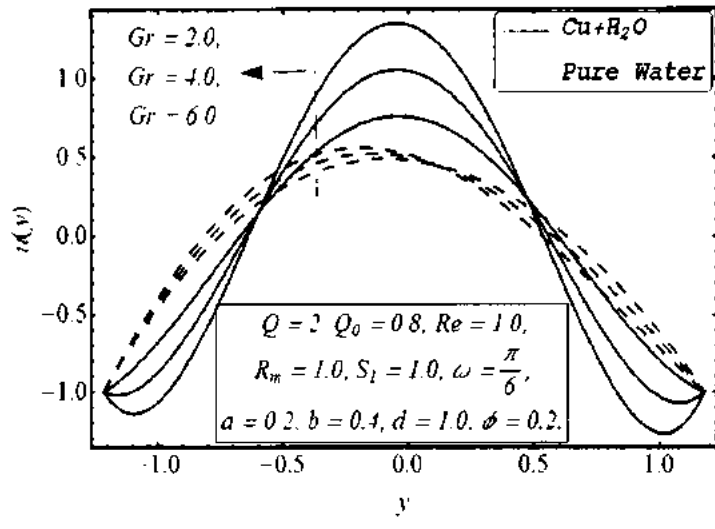
Figs. 4.4(a). Variation of velocity profile u with for flow parameter ϕ .



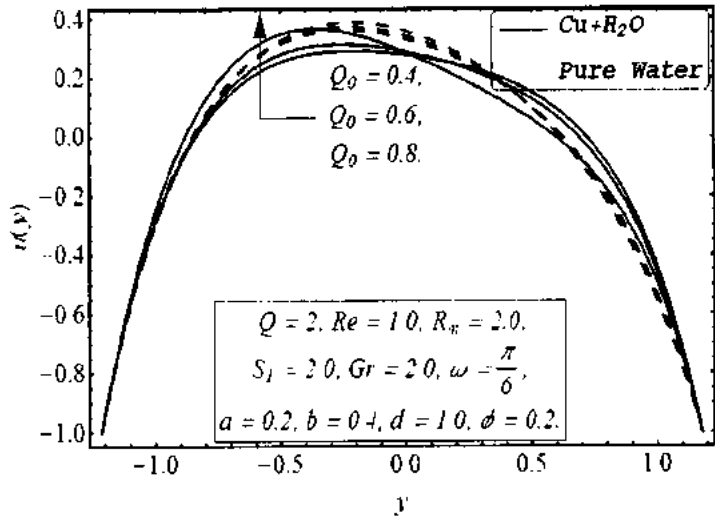
Figs. 4.4(b). Variation of velocity profile u with for flow parameter S_1 .



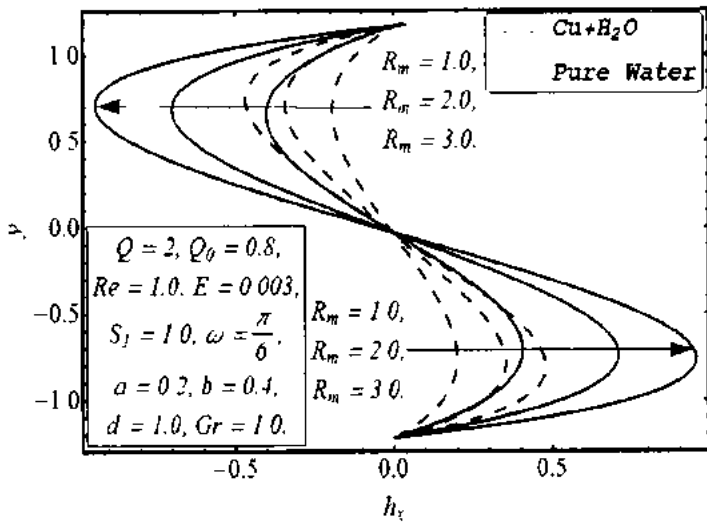
Figs. 4.4(c). Variation of velocity profile u with for flow parameter R_m .



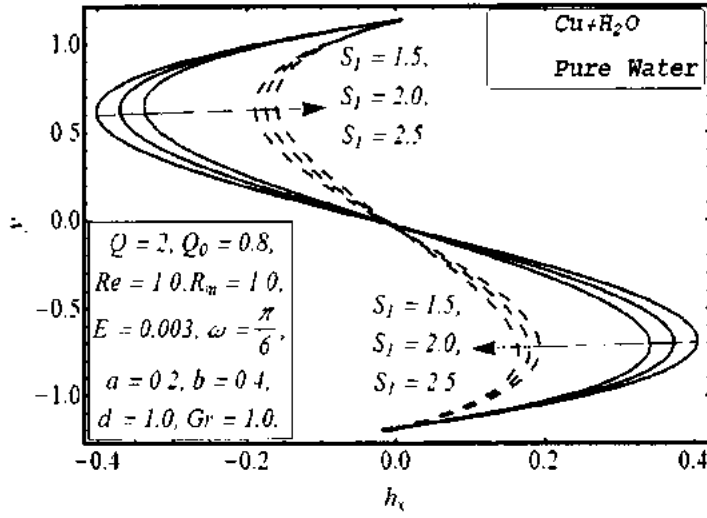
Figs. 4.4(d). Variation of velocity profile u with for flow parameter Gr .



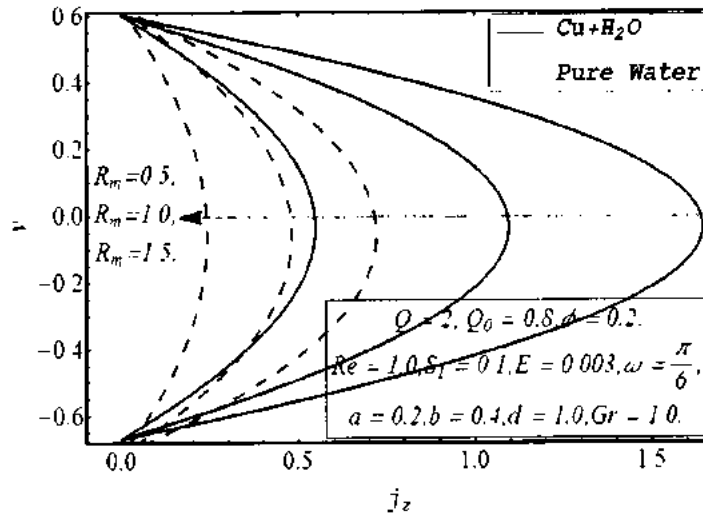
Figs. 4. 4(e). Variation of velocity profile u with for flow paramter Q_0 .



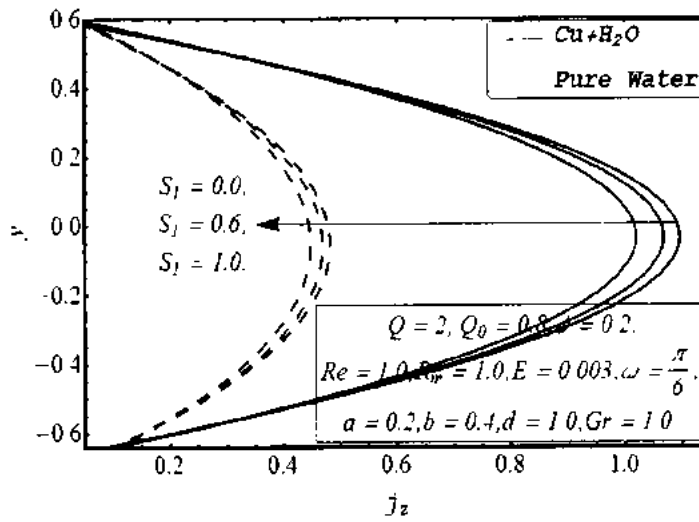
Figs. 4. 5(a). Variation of axial induced magnetic field h_x for different parameter R_m .



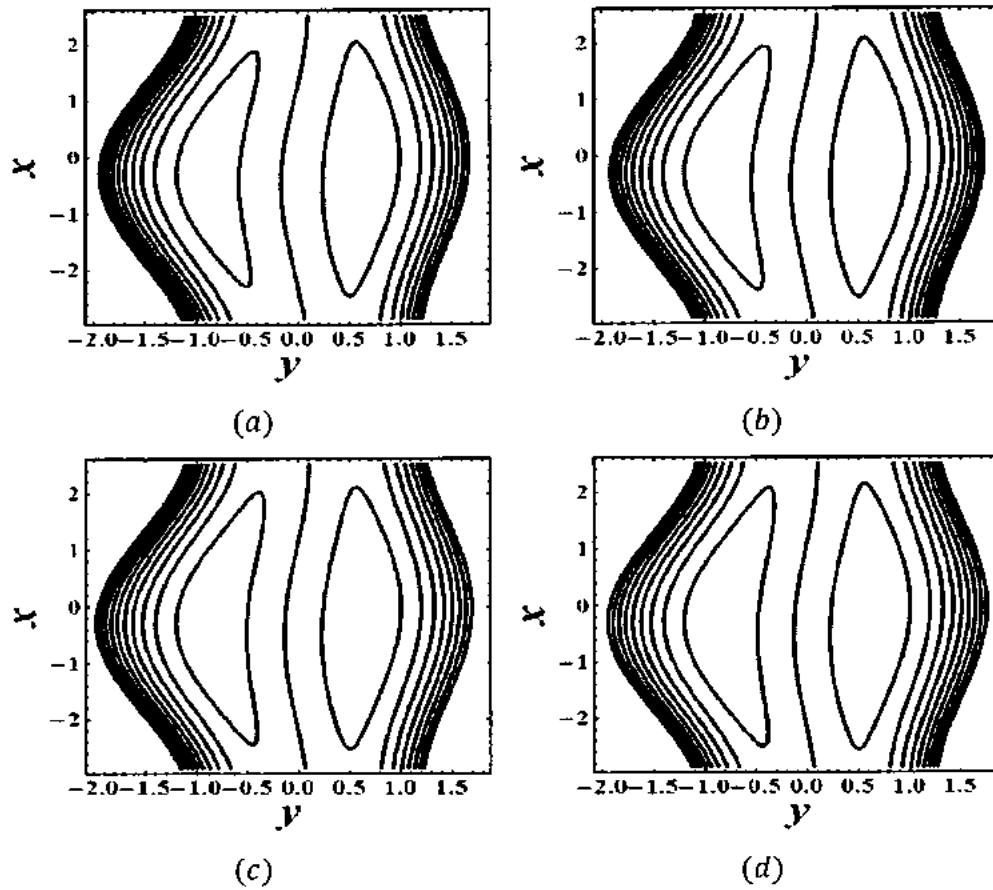
Figs. 4. 5(b). Variation of axial induced magnetic field h_x for different parameter S_1 .



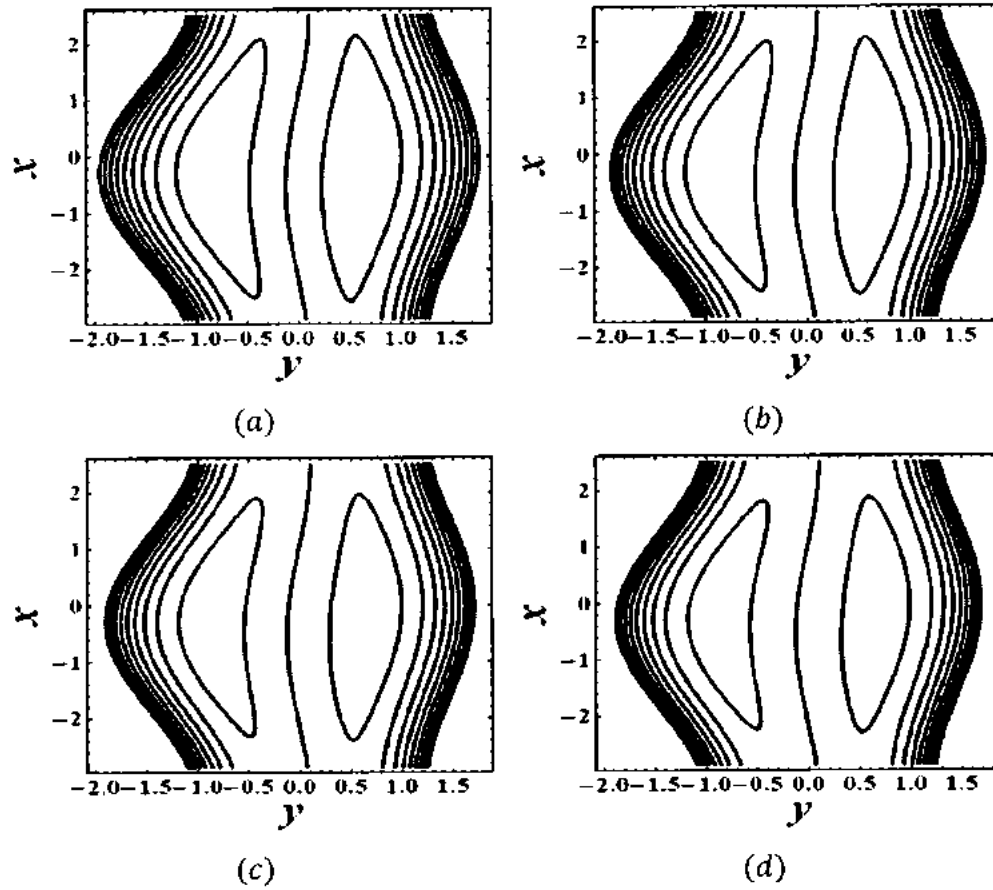
Figs. 4.6(a). Variation of current density J_z for flow parameter R_m .



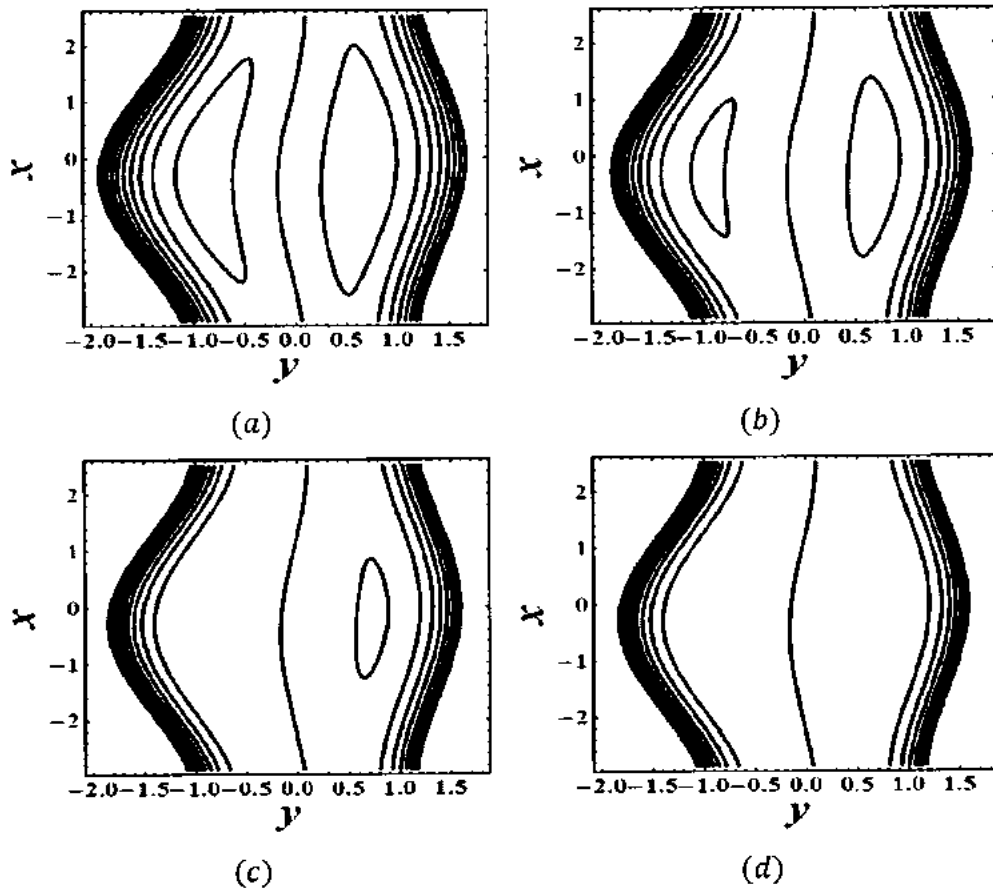
Figs. 4.6(b). Variation of current density J_z for flow parameter S_1 .



Figs. 4.7(a)- 4.7(d). Stream lines of copper water fluid for different values of ϕ .
 (a) for $\phi = 0.1$, (b) for $\phi = 0.2$, (c) for $\phi = 0.3$, (d) for $\phi = 0.4$. The other parameters are $Q = 2.0$, $\omega = 0.3$, $a = 0.2$, $b = 0.3$, $d = 1.0$, $Gr = 1.0$, $R_m = 1.0$, $S_1 = 2.0$, $Re = 1.0$ and $Q_0 = 0.1$.



Figs. 4.8(a)- 4.8(d). Stream lines of copper water fluid for different values of Gr .
 (a) for $Gr = 1.0$, (b) for $Gr = 2.0$, (c) for $Gr = 3.0$, (d) for $Gr = 4.0$. The other parameters are $Q = 2.0$, $\omega = 0.3$, $a = 0.2$, $b = 0.4$, $d = 1.0$, $\phi = 0.4$, $R_m = 1.0$, $S_1 = 2.0$, $Re = 1.0$ and $Q_0 = 0.1$.



Figs. 4.9(a)- 4.9(d). Stream lines of pure water for different values of Gr .
 (a) for $Gr = 1.0$, (b) for $Gr = 2.0$, (c) for $Gr = 3.0$, (d) for $Gr = 4.0$. The other parameters are $Q = 2.0$, $\omega = 0.3$, $a = 0.2$, $b = 0.4$, $d = 1.0$, $\phi = 0.0$, $R_m = 1.0$, $S_1 = 2.0$, $Re = 1.0$ and $Q_0 = 0.1$.

4.4 Concluding remarks

In this chapter the communication of nanoparticles for the peristaltic flow with induced magnetic field is investigated. Key focuses are seen as

- i. It is seen that pressure rise is an expanding capacity with the expansions of nanoparticle volume fraction all through in the retrograde pumping area.
- ii. It is measured that pressure rise gets diminished with the expanding impacts of Stommer's and magnetic Reynolds number for both copper water and unadulterated water.
- iii. The variation of the magnetic Reynolds gives the same conduct on pressure gradient for both copper water and pure water.
- iv. It is noticed that value of pressure gradient is reductions as expansions of Grashof number.
- v. For the distinctive estimations of volume fraction, it can see that as expansions the volume fraction temperature likewise increments.
- vi. Temperature profile increments as the expansions of heat generation parameter for both copper water and pure water cases.
- vii. It is watched that if there should be an occurrence of copper water velocity is reductions in the first and third phase *i.e.*, close to one side divider and right divider individually with an expansion of Grashof number. In the focal point of channel, the estimation of velocity goes to the extreme level. If there should arise an occurrence of unadulterated water, velocity profile increments from the left wall of channel to the focal point of channel on expansion of Grashof number. Be that as it may, inverse conduct is seen from focal point of the channel to the right divider.
- viii. It is noticed that bolus turns out to be huge when it has given more noteworthy qualities to the volume fraction.
- ix. It can be seen that bolus turns out to be small when it has given more prominent estimations of Grashof number.

Chapter 5

Influence of induced magnetic field and heat flux with the suspension of carbon nanotubes for the peristaltic flow in a permeable channel

This chapter is intended for investigating the effects of heat flux and induced magnetic field for the peristaltic flow of single and multiwall carbon nanotubes with the base fluid water in the symmetric vertical permeable channel. Mathematical modeling is based upon continuity, momentum, energy and magnetic induction equations. The obtained expressions for pressure gradient, pressure rise, temperature, axial magnetic field, current density and velocity phenomenon are described through graphs for various pertinent parameters.

5.1 Mathematical formulation

Consider water based nanofluid flow containing SWCNT and MWCNT with in vertical symmetric permeable channel. The mathematical description of geometry of the problem is shown in Fig. 2.1 using the relations Eq. (2.8) and non-dimensional parameters Eq. (2.13) In the presence of induced magnetic field, the governing Eqs. (1.39), (1.41) (1.45) and (1.53) (without using bars) for nanofluid take the final form as

$$\frac{\partial u}{\partial x} + \frac{\partial v}{\partial y} = 0, \quad (5.1)$$

$$\frac{dp}{dx} = \frac{\partial^3 \psi}{\partial y^3} \left(\frac{1}{(1-\phi)^{2.5}} \right) + \text{Re} S_1^2 \Phi_{,y} + \frac{(\rho\beta^*)_{nf}}{(\rho\beta^*)_f} Gr\theta, \quad (5.2)$$

$$\frac{dp}{dy} = 0, \quad (5.3)$$

$$\Phi_{,y} = R_m \left(E - \frac{\partial \psi}{\partial y} \right), \quad (5.4)$$

$$\left(\frac{k_{nf}}{k_f} - N \right) \frac{\partial^2 \theta}{\partial y^2} + Q_o = 0. \quad (5.5)$$

Putting Eq. (5.4) into Eq. (5.2) we get

$$\frac{dp}{dx} = \frac{\partial^3 \psi}{\partial y^3} \left(\frac{\mu_{nf}}{\mu_f} \right) + \text{Re} S_1^2 R_m \left(E - \frac{\partial \psi}{\partial y} \right) + \frac{(\rho \beta^*)_{nf}}{(\rho \beta^*)_f} Gr \theta. \quad (5.6)$$

Taking derivative of Eq. (5.6) with respect to y , we have

$$\frac{\partial^4 \psi}{\partial y^4} \left(\frac{\mu_{nf}}{\mu_f} \right) + \text{Re} S_1^2 R_m \left(-\frac{\partial^2 \psi}{\partial y^2} \right) + \frac{(\rho \beta^*)_{nf}}{(\rho \beta^*)_f} Gr \frac{\partial \theta}{\partial y} = 0. \quad (5.7)$$

The non-dimensional boundaries are

$$\psi = 0, \quad \frac{\partial^2 \psi}{\partial y^2} = 0, \quad \text{at } y = 0. \quad (5.8)$$

$$\psi = F, \quad \frac{\partial \psi}{\partial y} = -1 - \frac{\sqrt{D_\alpha}}{\alpha} \frac{\partial^2 \psi}{\partial y^2}, \quad \text{at } y = h. \quad (5.9)$$

$$\frac{\partial \theta}{\partial y} = 0 \quad \text{at } y = 0, \quad \theta = 0 \quad \text{at } y = h, \quad (5.10)$$

$$\frac{\partial \Phi}{\partial y} = 0 \quad \text{at } y = 0, \quad \Phi = 0 \quad \text{at } y = h. \quad (5.11)$$

The pressure rise Δp , axial induced magnetic h , and current density J_x in non-dimensional form is defined in Eqs. (2.26), (4.12) and (4.13) respectively. In present chapter conductivity of nanofluid Eq. (1.24) and the effective viscosity of nanofluid Eq. (1.21) are used, thermal physical properties of water and nanoparticles defined in table 5.1.

Table 5.1. Thermal-physical properties of water and nanoparticles.

Physical Properties	Water (H_2O)	SWCNT	MWCNT
ρ (kgm^{-3})	997.1	2600	1600
C_p ($Jkg^{-1}K^{-1}$)	4179	425	796
k ($W/m-K$)	0.613	6600	3000
β (K^{-1}) $\times 10^{-5}$	21.0	2.6	2.8

5.2 Solution of the problem

The exact solutions of the Eqs. (5.4), (5.5) and (5.7) using boundary conditions given in Eqs. (5.8) – (5.11) are found as follows:

$$\theta(y) = \frac{Q_0 k_f (y^2 - h^2)}{2Nk_f - 2k_{nf}} \quad (5.17)$$

$$\psi(y) = \frac{k_f \left((C_{45} - C_{46}) 6N\beta_f \rho_f \mu_{nf} \left[(C_{48} - C_{47}) \sinh\left(\frac{\sqrt{Re} S_1 \sqrt{\mu_f} \sqrt{R_m}}{\sqrt{\mu_{nf}}}\right) + (C_{47} + C_{48}) \cosh\left(\frac{\sqrt{Re} S_1 \sqrt{\mu_f} \sqrt{R_m}}{\sqrt{\mu_{nf}}}\right) \right] + Gr Q_0 y^3 \mu_f \beta_{nf} \rho_{nf} \right) - 6\beta_f \rho_f k_{nf} \mu_{nf} \left[(C_{48} - C_{47}) \sinh\left(\frac{\sqrt{Re} S_1 \sqrt{\mu_f} \sqrt{R_m}}{\sqrt{\mu_{nf}}}\right) + (C_{47} + C_{48}) \cosh\left(\frac{\sqrt{Re} S_1 \sqrt{\mu_f} \sqrt{R_m}}{\sqrt{\mu_{nf}}}\right) \right]}{6 Re S_1^2 \beta_f \mu_f \rho_f R_m (Nk_f - k_{nf})} + C_{50} y + C_{49} \quad (5.18)$$

The mean volume flow rate Q over one period is given in Eq. (2.31) and pressure gradient dp/dx , axial induced magnetic h , and current density J_z are elaborated as

$$\frac{dp}{dx} = \frac{\sinh\left(\frac{h\sqrt{\text{Re}S_1}\sqrt{\mu_f}\sqrt{R_m}}{\sqrt{\mu_{nf}}}\right)\left(6\text{Re}S_1^2\beta_f\rho_fR_m\left(\sqrt{D_\alpha}F\text{Re}S_1^2\mu_fR_m + \alpha\mu_{nf}\right) + \text{Gr}hQ_0k_f\beta_{nf}\rho_{nf}\left(3\mu_{nf}\left(2\sqrt{D_\alpha} + \alpha h\right) - \sqrt{D_\alpha}h^2\text{Re}S_1^2\mu_fR_m\right)\right) + \alpha\sqrt{\text{Re}S_1}\sqrt{\mu_f}\sqrt{R_m}\sqrt{\mu_{nf}}\cosh\left(\frac{h\sqrt{\text{Re}S_1}\sqrt{\mu_f}\sqrt{R_m}}{\sqrt{\mu_{nf}}}\right)\left(6F\text{Re}S_1^2\beta_f\rho_fR_mkN - \text{Gr}h^3Q_0k_f\beta_{nf}\rho_{nf}\right)}{6\text{Re}S_1^2\beta_f\rho_fR_m\left(\sinh\left(\frac{h\sqrt{\text{Re}S_1}\sqrt{\mu_f}\sqrt{R_m}}{\sqrt{\mu_{nf}}}\right)\left(\sqrt{D_\alpha}h\text{Re}S_1^2\mu_fR_m - \alpha\mu_{nf}\right) + \alpha h\sqrt{\text{Re}S_1}\sqrt{\mu_f}\sqrt{R_m}\sqrt{\mu_{nf}}\cosh\left(\frac{h\sqrt{\text{Re}S_1}\sqrt{\mu_f}\sqrt{R_m}}{\sqrt{\mu_{nf}}}\right)\right)}, \quad (5.19)$$

$$h_1 = C_{52} - \frac{\left[\begin{aligned} & -24N\text{Re}S_1^2y\beta_fk_f\mu_f^{3/2}\rho_fR_m + 24\text{Re}S_1^2y\beta_f\mu_f^{3/2}\rho_fk_{nf}R_m - \\ & 24(C_{47} - C_{48})N\beta_fk_f\sqrt{\mu_f}\rho_f\mu_{nf}\sinh\left(\frac{\sqrt{\text{Re}S_1y}\sqrt{\mu_f}\sqrt{R_m}}{\sqrt{\mu_{nf}}}\right) + \\ & 24(C_{47} + C_{48})N\beta_fk_f\sqrt{\mu_f}\rho_f\mu_{nf}\cosh\left(\frac{\sqrt{\text{Re}S_1y}\sqrt{\mu_f}\sqrt{R_m}}{\sqrt{\mu_{nf}}}\right) + \\ & 24(C_{47} - C_{48})\beta_f\sqrt{\mu_f}\rho_fk_{nf}\mu_{nf}\sinh\left(\frac{\sqrt{\text{Re}S_1}\sqrt{\mu_f}\sqrt{R_m}}{\sqrt{\mu_{nf}}}\right) - \\ & 24(C_{47} + C_{48})\beta_f\sqrt{\mu_f}\rho_fk_{nf}\mu_{nf}\cosh\left(\frac{\sqrt{\text{Re}S_1}\sqrt{\mu_f}\sqrt{R_m}}{\sqrt{\mu_{nf}}}\right) + \\ & 4\text{Gr}Q_0y^3k_f\mu_f^{3/2}\beta_{nf}\rho_{nf} \end{aligned} \right]}{24\text{Re}S_1^2\beta_f\mu_f^{3/2}\rho_f}, \quad (5.20)$$

$$J_2 = \frac{\sqrt{\mu_f}\left(\text{Gr}Q_0y^2k_f\beta_{nf}\rho_{nf} - 2\text{Re}S_1^2(E - C_{50})\beta_f\rho_fR_mkN\right) + 2(C_{47} + C_{48})\sqrt{\text{Re}S_1}\beta_f\rho_f\sqrt{R_m}\sqrt{\mu_{nf}}\sinh\left(\frac{\sqrt{\text{Re}S_1y}\sqrt{\mu_f}\sqrt{R_m}}{\sqrt{\mu_{nf}}}\right) - 2(C_{47} - C_{48})\sqrt{\text{Re}S_1}\beta_f\rho_f\sqrt{R_m}\sqrt{\mu_{nf}}\cosh\left(\frac{\sqrt{\text{Re}S_1}\sqrt{\mu_f}\sqrt{R_m}}{\sqrt{\mu_{nf}}}\right)}{2\text{Re}S_1^2\beta_f\sqrt{\mu_f}\rho_f}, \quad (5.21)$$

where $C_{45} - C_{52}$ are constants that can be obtain by Mathematica 9.

5.3 Results and discussion

To consider the conduct of the solution, for a few qualities applicable parameters have been done for both CNTs with water as base fluid. Fig. 5.1(a) speaks to the impacts of volume division ϕ on the Δp It is seen here that pressure rise is increasing capacity with the expansion of ϕ all through the domain, Fig. 5.1(b) portrays that as it will build the estimation of R_m then pressure rise increments in the retrograde area. Fig. 5.1(c) demonstrates the impact of S_1 on pressure rise, it is watched that pressure rise demonstrates the same conduct which is appeared for R_m , Figs. 5.1(d) - 5.1(e) demonstrate the impact of Q_0 and N individually. It has been watched that pressure rise

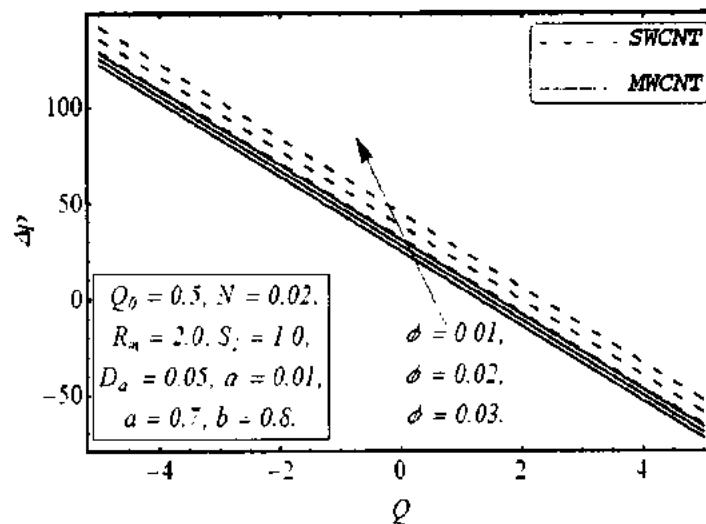
increasing by increase in Q_0 and N in the entire area for $(SWCNT + H_2O)$ and $(MWCNT + H_2O)$. The impact of the ϕ on the pressure gradient is outlined in Fig. 5.2(a) it is apparent that, expand the estimation of ϕ tends to builds the pressure gradient, it is watched that the impact of ϕ on pressure gradient is slightest if there should arise an occurrence of $(SWCNT + H_2O)$ while the impact of ϕ is generally bigger with $(MWCNT + H_2O)$. The variation of R_m and S_1 on pressure gradient is appeared in Figs. 5.2(b) – 5.2(c), it demonstrates that pressure gradient is expanding on an expansion in R_m and S_1 for both sorts of fluids, Figs. 5.2(d) – 5.2(e) showed that pressure gradient diminishes with an expansion in heat generation parameter and heat flux parameter all through the channel for both sorts of fluid. Figs. 5.3(a) – 5.3(c) to comprehend the variation of temperature for various estimations of ϕ , Q_0 and N . Fig. 5.3(a) demonstrates that θ diminishes as it is increment ϕ for both sorts of fluid.

When it is watch Figs. 5.3(b) – 5.3(c), the same pattern is watched for heat generation parameter Q_0 and heat flux parameter individually, it had watched that by expanding Q_0 and N , θ likewise increment. Plotted Figs. 5.4(a) – 5.4(e) to outline the impacts of germane parameters on velocity profile u . It is seen from Fig. 5.4(a) that velocity profile increments alongside the dividers yet diminishes at the center of channel with expanding the estimation of ϕ . Displayed the Figs. 5.4(b) – 5.4(c) to get the variation of velocity profile u for fluctuating the magnitude of the parameters R_m and S_1 for both sorts of fluid. It delineates that velocity is diminishing with expansion of R_m and S_1 at the center of channel yet inverse conduct is seen at center of channel. It had displayed the Fig. 5.4(d) to get the variation of velocity profile u for shifting the size of the parameter Q_0 . It portrays that velocity is expanding with expansion of Q_0 . at the center of channel however inverse conduct is seen along the left and right dividers of channel. Fig. 5.4(e) demonstrates the impact of Darcy number D_α on velocity profile it is watched that close to one side and right divider velocity profile is expanding by expansion of D_α however at focal point of channel, it has seen the inverse conduct of velocity profile.

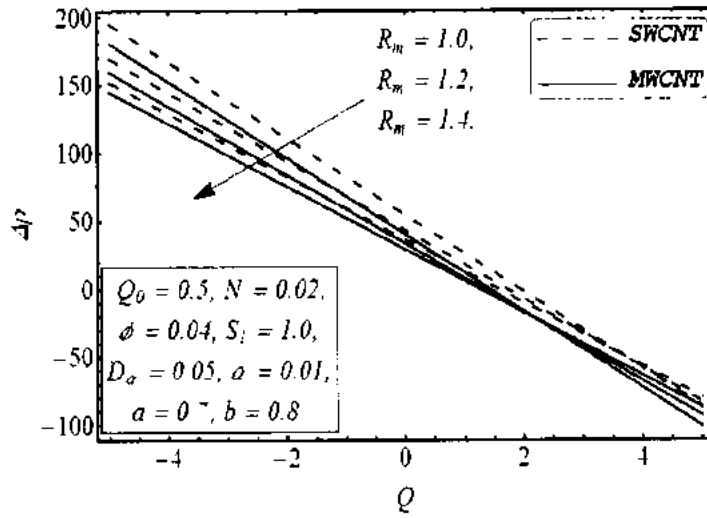
To watched the conduct of slip parameter α on velocity profile, showed Fig. 5.4(f) this figure demonstrates that along the dividers velocity profile is diminishing by expansion of α , yet at focal point of the channel velocity profile increments. Figs. 5.5(a) – 5.5(b) demonstrate the variation of magnetic Reynolds and Stommer's number on an axial

induced magnetic field h_x versus y . The Fig. 5.5(a) displays that the magnitude of h_x increases when R_m increments from divider to the center of channel, yet the diminishing pattern is seen in the other portion of the channel keeping R_m expanded. Then again, the impacts of S_1 on h_x are very inverse in contrast with R_m . In Figs. 5.6(a) - 5.6(b) the current density j_z is appeared as a component of y for three different values of R_m and S_1 respectively, both of these figures are of parabolic type, one can find in Fig. 5.6(a) that by expanding R_m , j_z also increment however from Fig. 5.6(b) demonstrates j_z diminish as the estimations of S_1 increase.

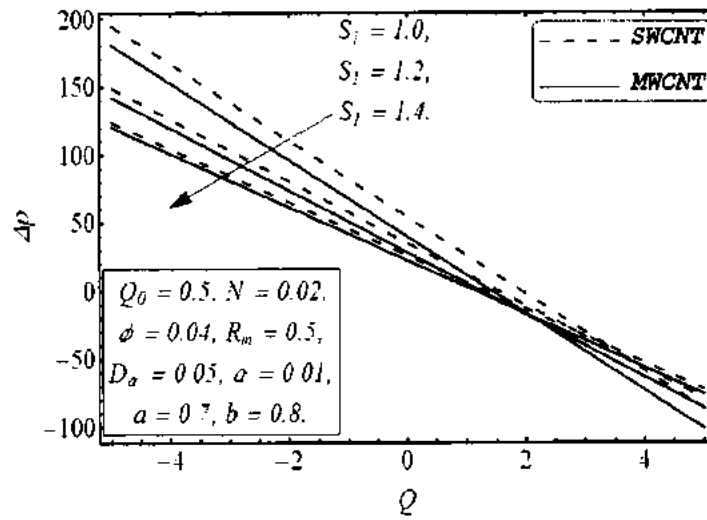
Figs. 5.7(a) - 5.8(d) show contour maps for the streamlines with four estimations of R_m ($R_m = 0.5, R_m = 1.0, R_m = 1.5, R_m = 2.0$) for both SWCNT and MWCNT. It is seen that bolus turns out to be substantial when we give more noteworthy qualities to the magnetic Reynolds number R_m . Figs. 5.9(a) - 5.10(d) demonstrate the streamlines for SWCNT and MWCNT separately, It is seen that bolus turns out to be small when it has given more noteworthy qualities to the S_1 , one can see from figures that number of bolus also decreases in both cases. Figs. 5.11(a) - 5.12(d) demonstrate the effect of Darcy number D_a on streamlines for SWCNT and MWCNT separately it is demonstrated that bolus turns out to be small as bigger estimations of D_a .



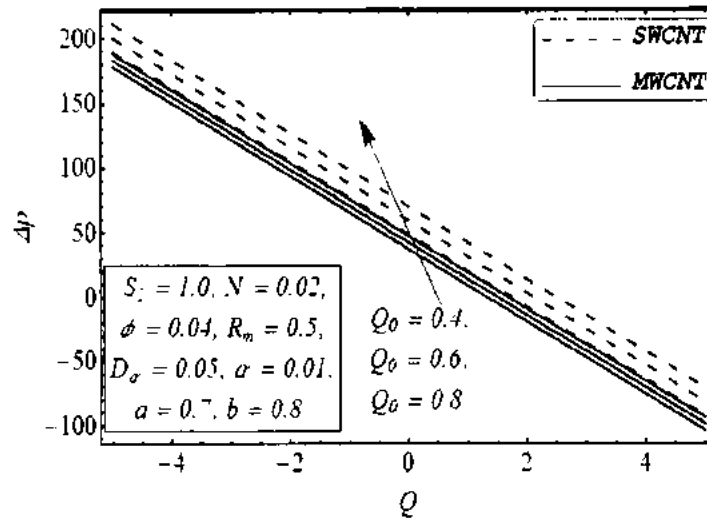
Figs. 5.1(a). Variation of pressure rise Δp for flow parameter ϕ .



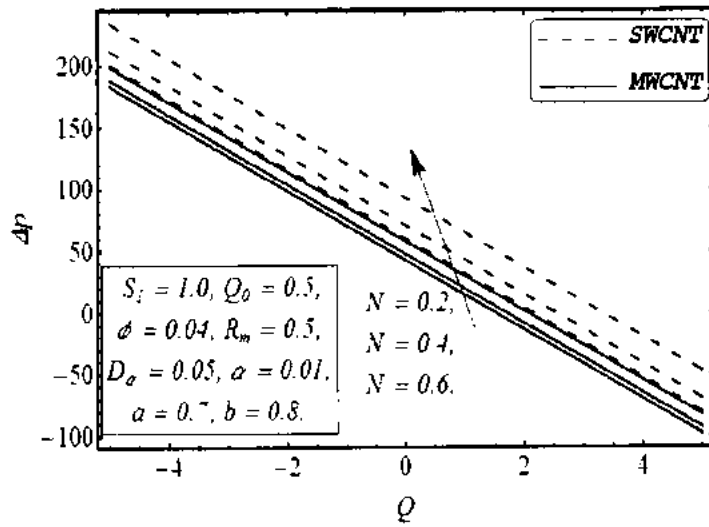
Figs. 5.1(b). Variation of pressure rise Δp for flow parameter R_m .



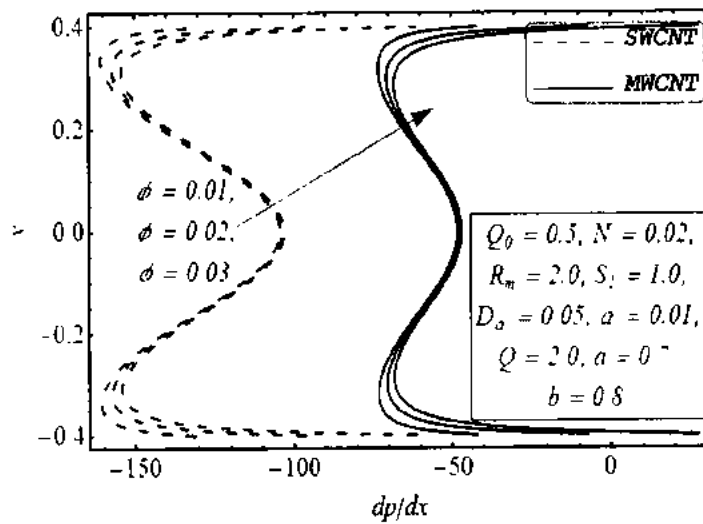
Figs. 5.1(c). Variation of pressure rise Δp for flow parameter S_i .



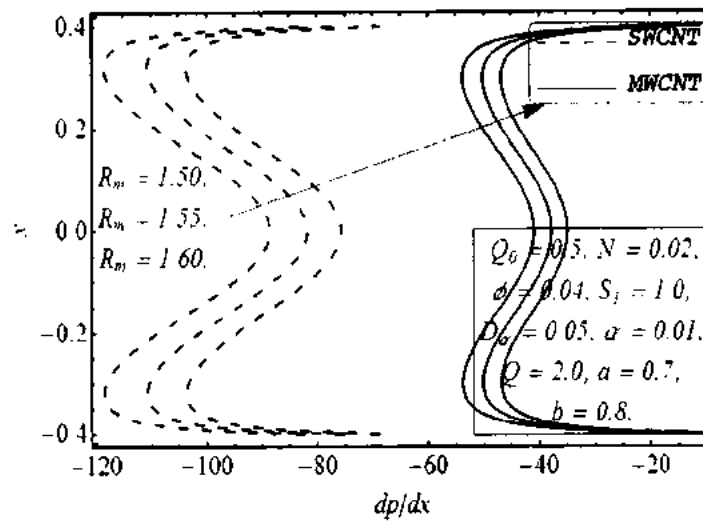
Figs. 5.1(d). Variation of pressure rise Δp for flow parameter Q_0 .



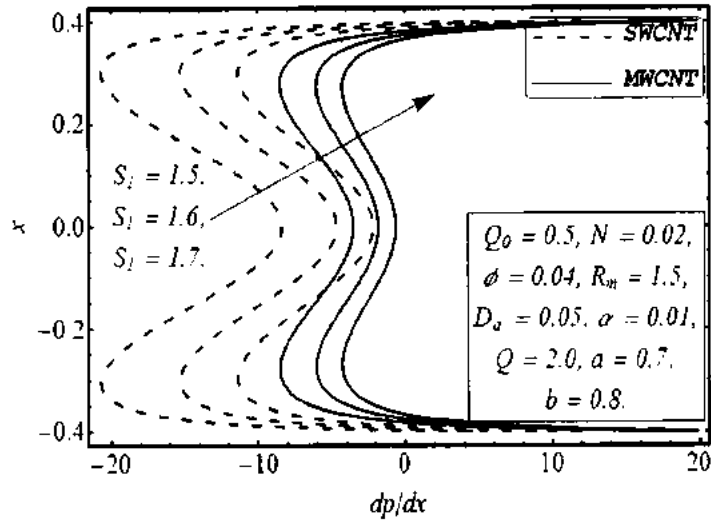
Figs. 5.1(e). Variation of pressure rise Δp for flow parameter N .



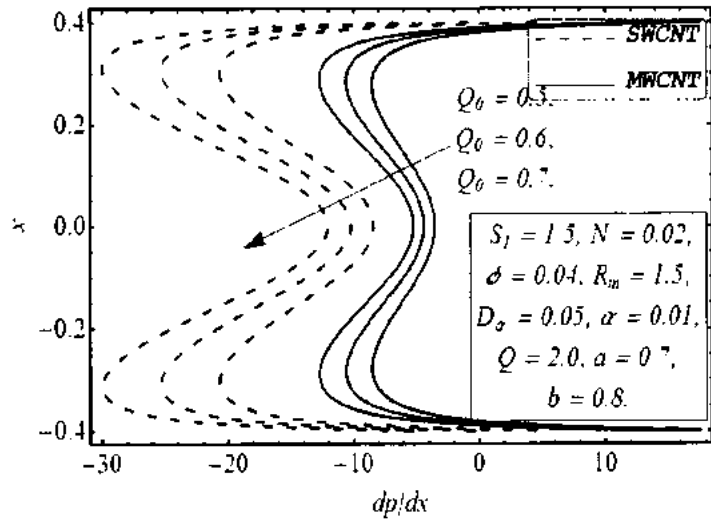
Figs. 5.2(a). Variation of pressure gradient dp/dx for flow parameter ϕ .



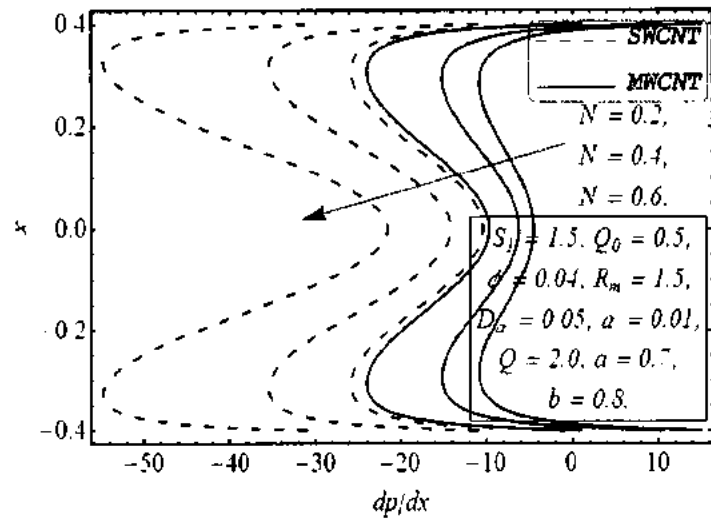
Figs. 5.2(b). Variation of pressure gradient dp/dx for flow parameter R_m .



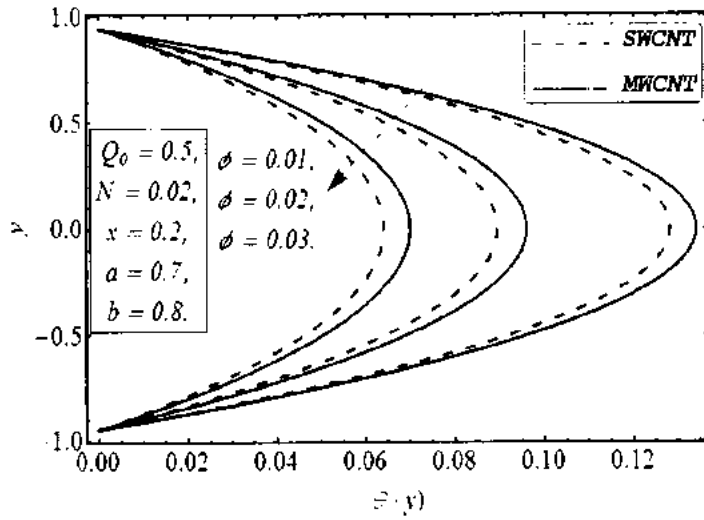
Figs. 5.2(c). Variation of pressure gradient dp/dx for flow parameter S_1 .



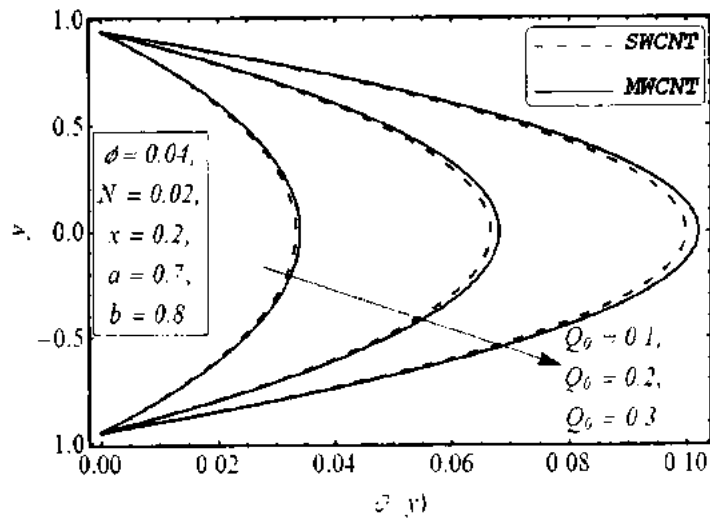
Figs. 5.2(d). Variation of pressure gradient dp/dx for flow parameter Q_0 .



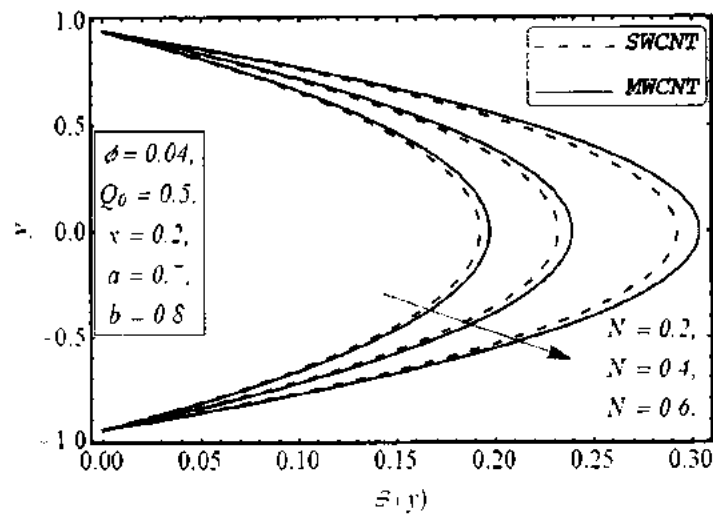
Figs. 5.2(e). Variation of pressure gradient dp/dx for flow parameter N .



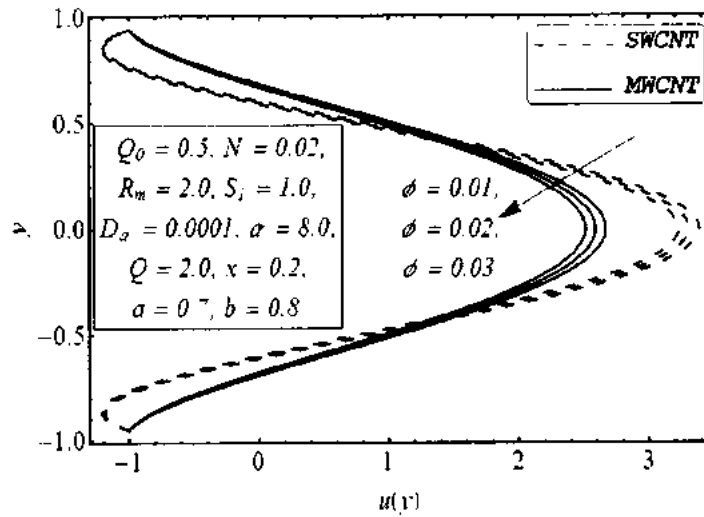
Figs. 5.3(a). Variation of temperature profile θ for flow parameter ϕ .



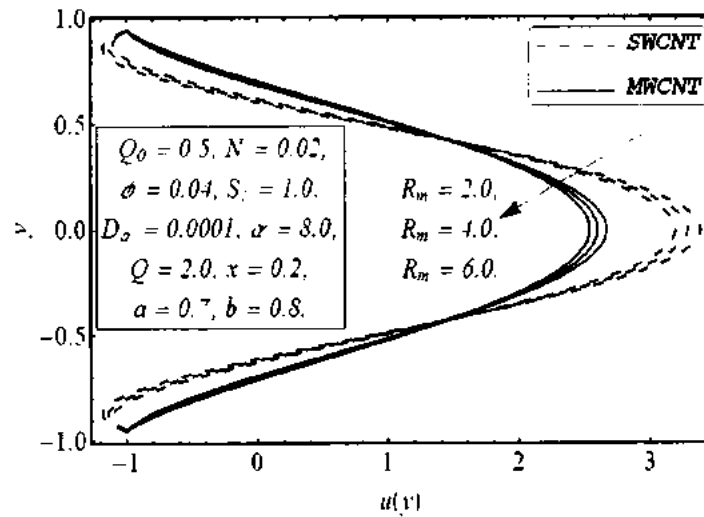
Figs. 5.3(b). Variation of temperature profile θ for flow parameter Q_0 .



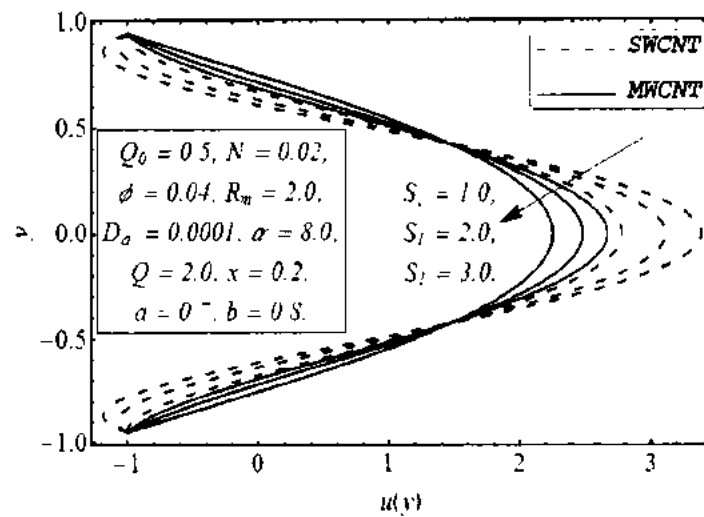
Figs. 5.3(c). Variation of temperature profile θ for flow parameter N .



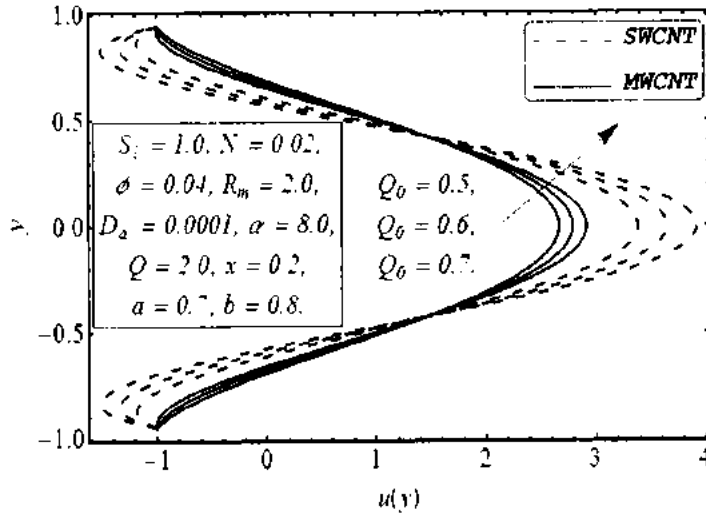
Figs. 5.4(a). Variation of velocity profile u for flow parameter ϕ .



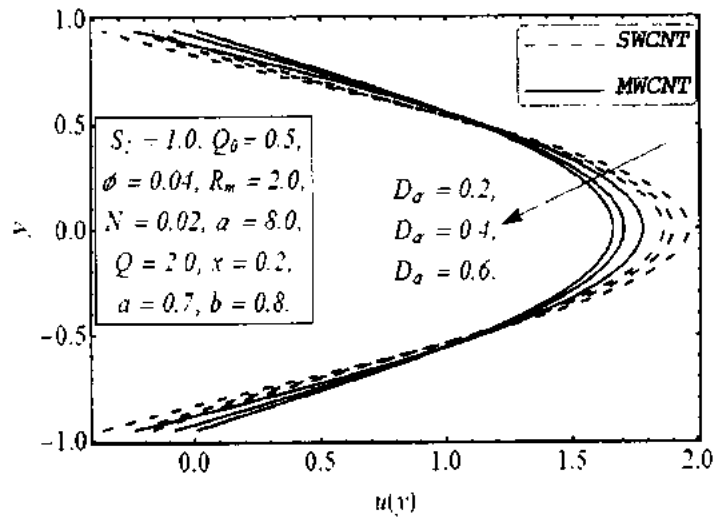
Figs. 5.4(b). Variation of velocity profile u for flow parameter R_m .



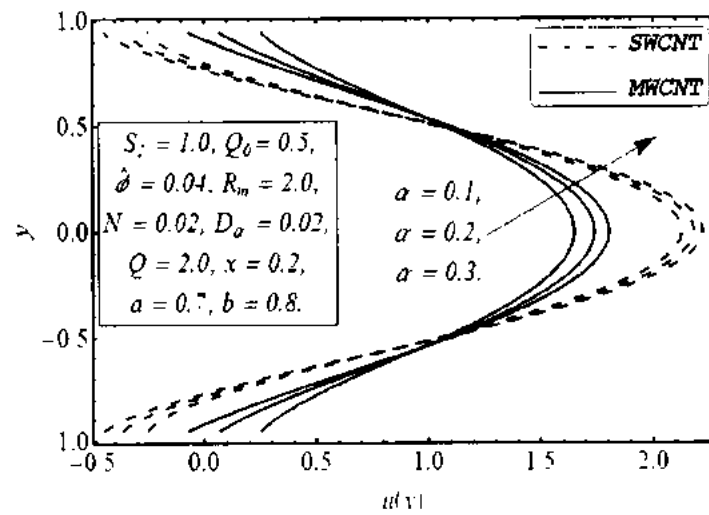
Figs. 5.4(c). Variation of velocity profile u for flow parameter S_1 .



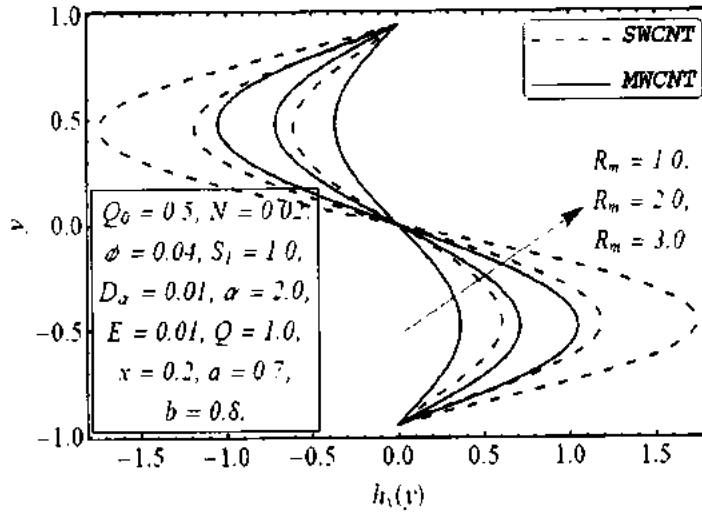
Figs. 5.4(d). Variation of velocity profile u for flow parameter Q_0 .



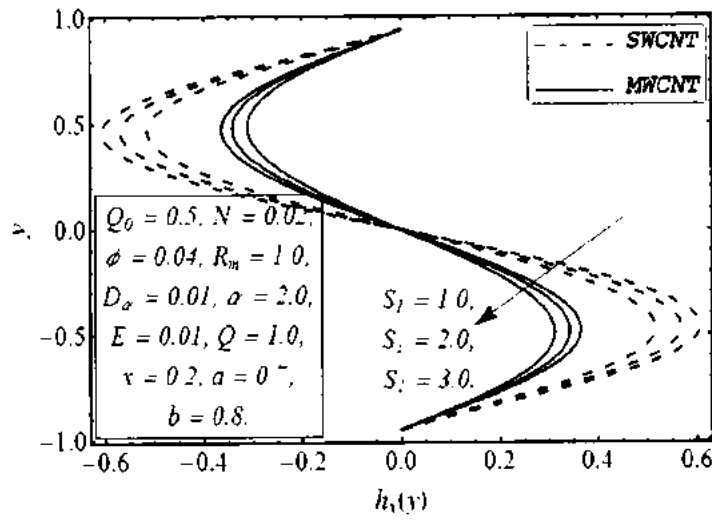
Figs. 5.4(e). Variation of velocity profile u for flow parameter D_α .



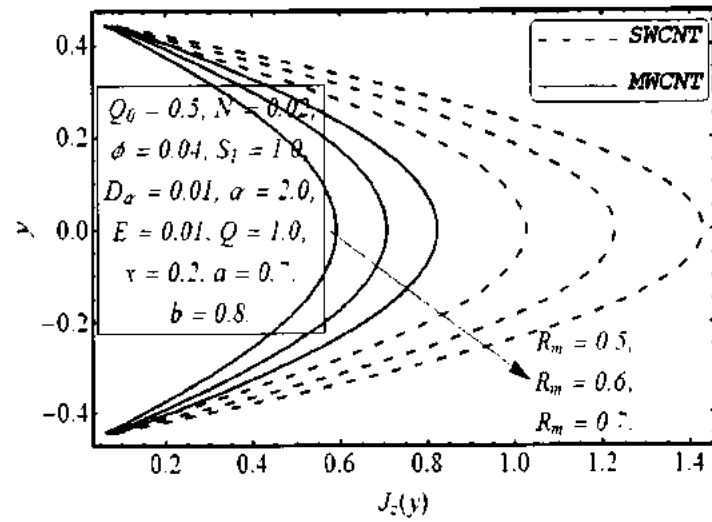
Figs. 5.4(f). Variation of velocity profile u for flow parameter α .



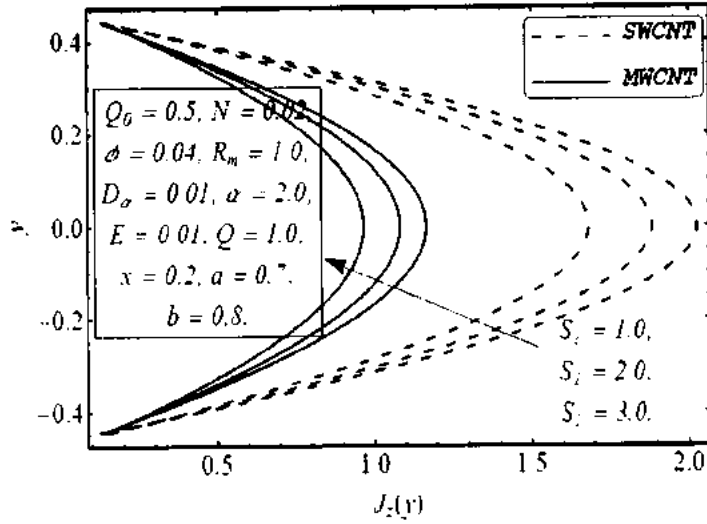
Figs. 5.5(a). Variation of axial induced magnetic field h_x for flow parameter R_m .



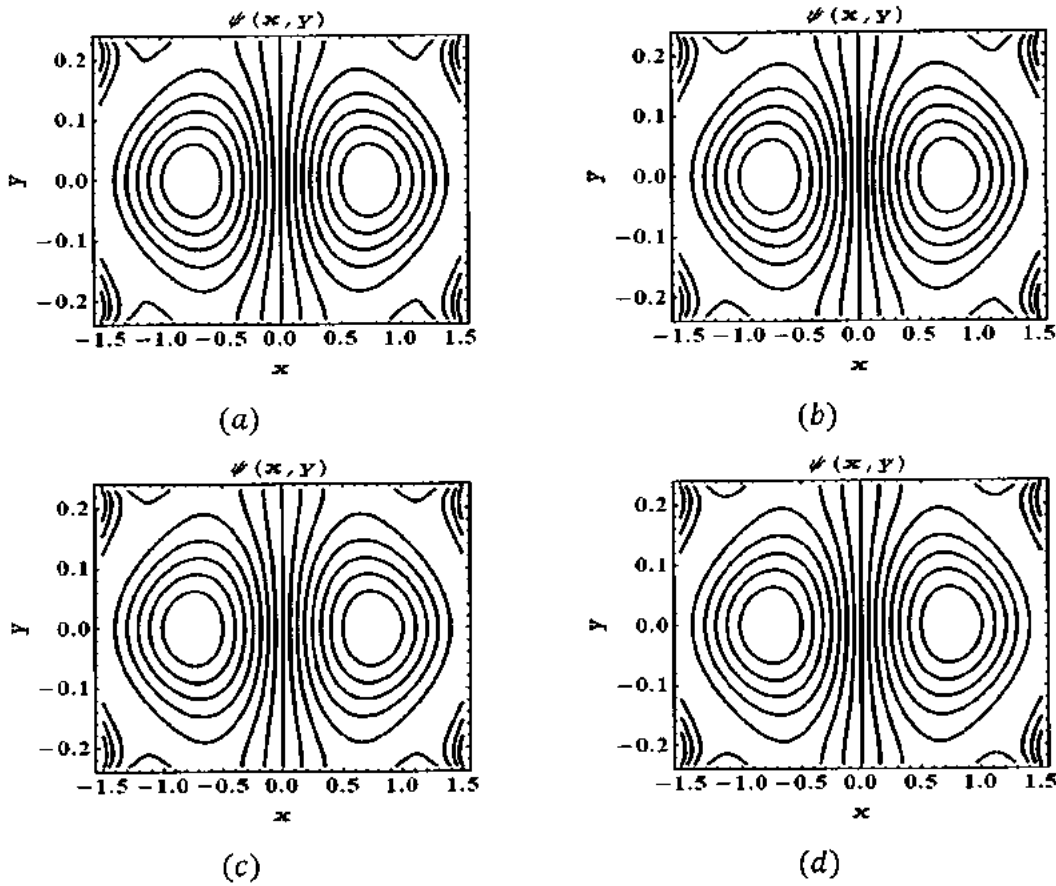
Figs. 5.5(a). Variation of axial induced magnetic field h_x for flow parameter S_1 .



Figs. 5.5(a). Variation of current density J_z for different flow parameter R_m .

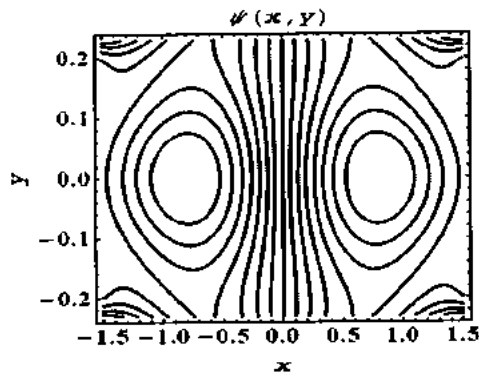


Figs. 5.5(b). Variation of current density J_z for different flow parameter S_1 .

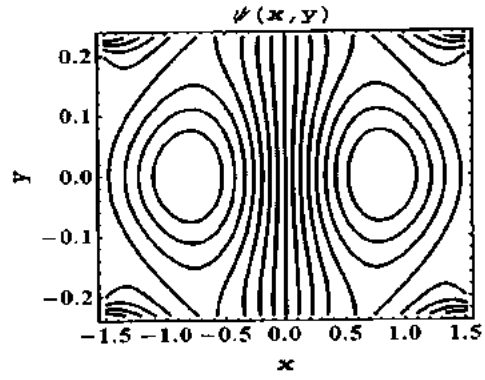


Figs. 5.7(a) - 5.7(d). Stream lines of SWCNT for different values of R_m .

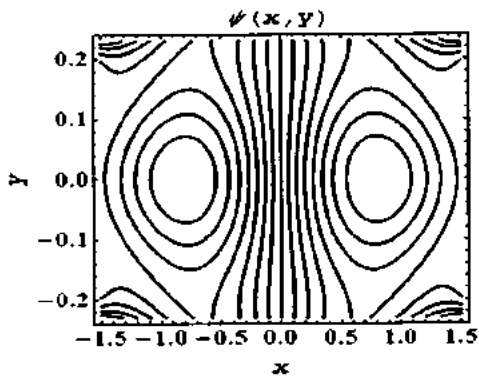
(a) for $R_m = 0.5$, (b) for $R_m = 1.0$, (c) for $R_m = 1.5$, (d) for $R_m = 2.0$. The other parameters are $Q = 2$, $\alpha = 2.0$, $a = 0.7$, $b = 0.8$, $S_1 = 1$, $N = 0.02$, $D_\alpha = 0.002$ and $Q_0 = 0.5$.



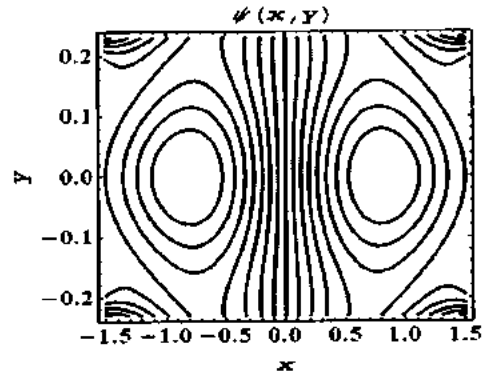
(a)



(b)



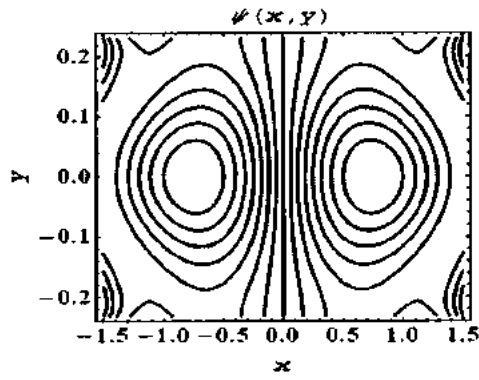
(c)



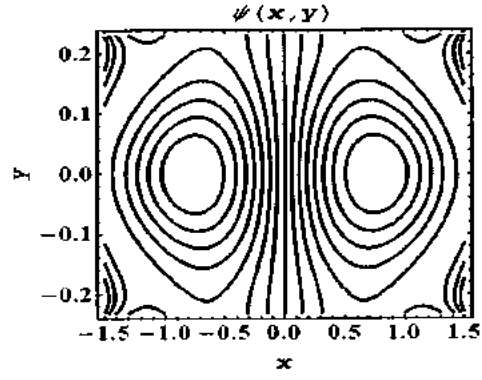
(d)

Figs. 5.8(a) - 5.8(d). Stream lines of MWCNT for different values of R_m .

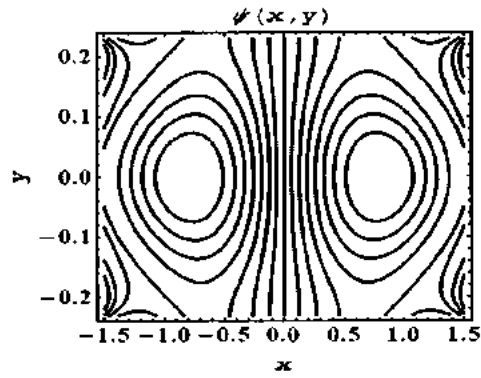
(a) for $R_m = 0.5$, (b) for $R_m = 1.0$, (c) for $R_m = 1.5$, (d) for $R_m = 2.0$. The other parameters are $Q = 2$, $\alpha = 2.0$, $a = 0.7$, $b = 0.8$, $S_1 = 1$, $N = 0.02$, $D_\alpha = 0.002$ and $Q_0 = 0.5$.



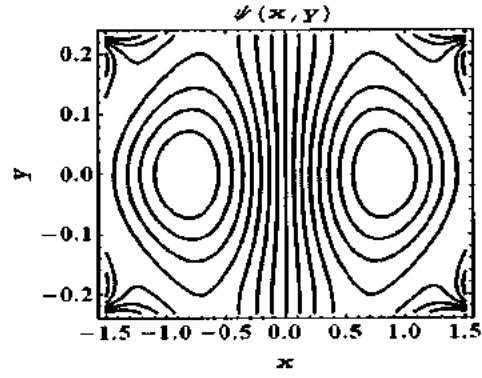
(a)



(b)



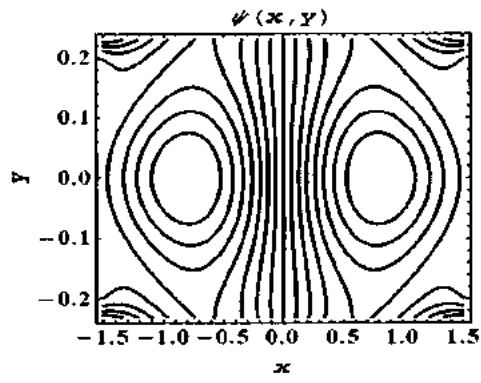
(c)



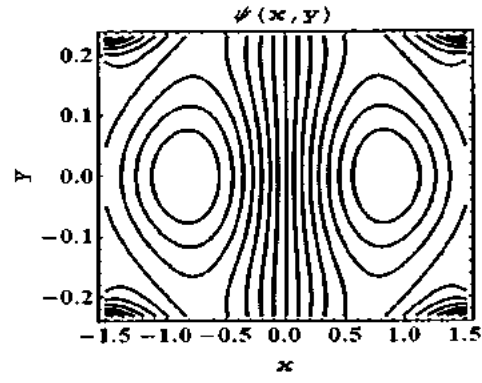
(d)

Figs. 5.9(a)– 5.9(d). Stream lines of SWCNT for different values of S_1 .

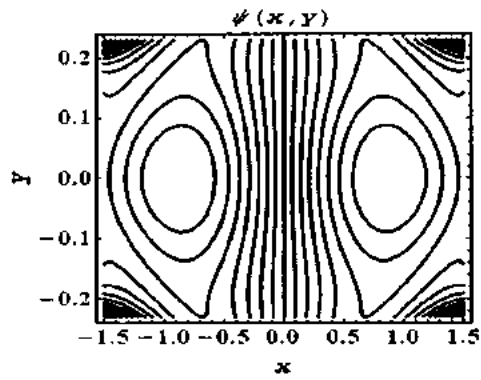
(a) for $S_1 = 1.0$, (b) for $S_1 = 2.0$, (c) for $S_1 = 3.0$, (d) for $S_1 = 4.0$. The other parameters are $Q = 2$, $\alpha = 2.0$, $a = 0.7$, $b = 0.8$, $R_m = 1$, $N = 0.02$, $D_\alpha = 0.002$ and $Q_0 = 0.5$.



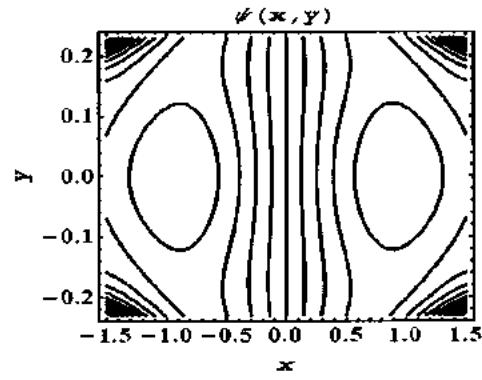
(a)



(b)



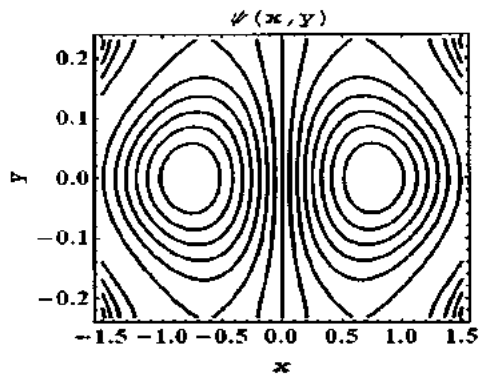
(c)



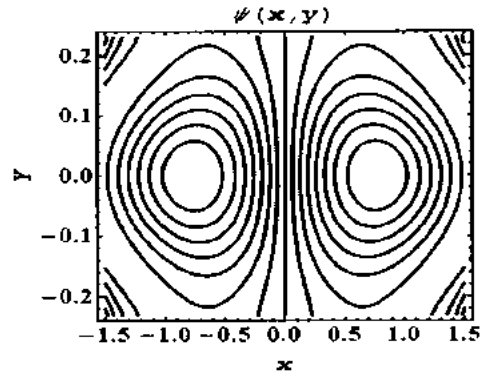
(d)

Figs. 5.10(a) – 5.10(d). Stream lines of MWCNT for different values of S_1 .

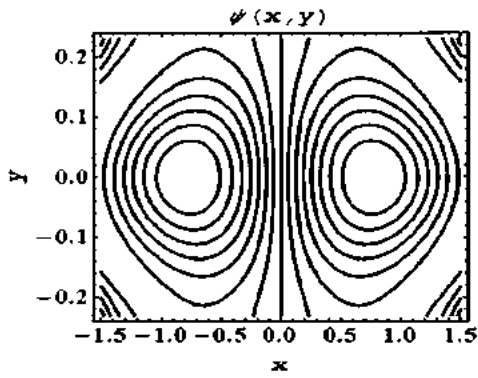
(a) for $S_1 = 1.0$, (b) for $S_1 = 2.0$, (c) for $S_1 = 3.0$, (d) for $S_1 = 4.0$. The other parameters are $Q = 2$, $\alpha = 2.0$, $a = 0.7$, $b = 0.8$, $S_1 = 1$, $N = 0.02$, $D_\alpha = 0.002$ and $Q_0 = 0.5$.



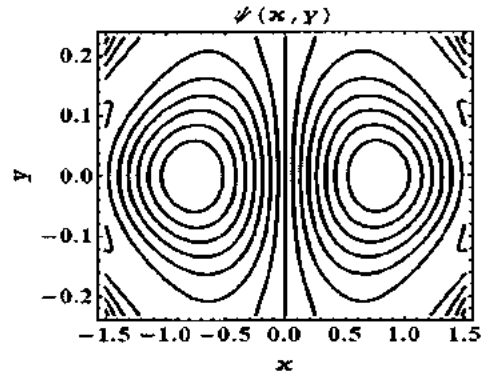
(a)



(b)



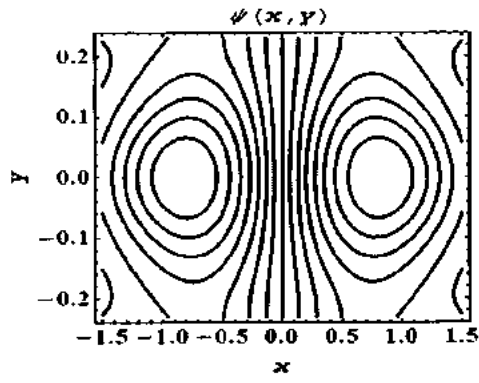
(c)



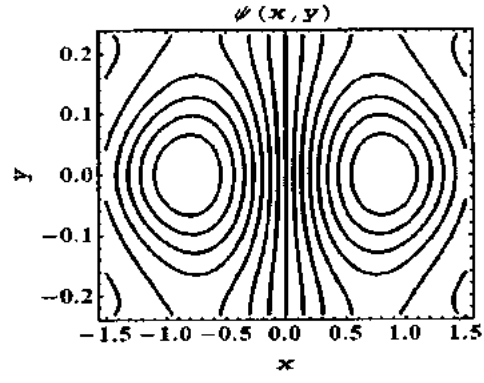
(d)

Figs. 5.11(a)- 5.11(d). Stream lines of SWCNT for different values of D_α .

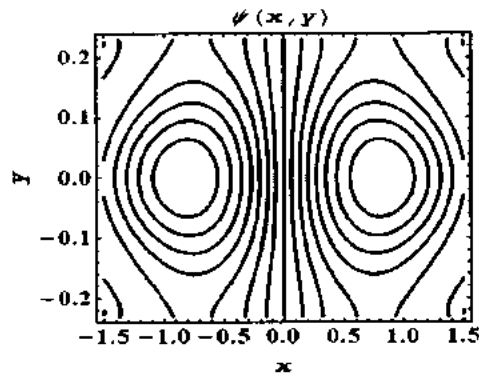
(a) for $D_\alpha = 0.1$, (b) for $D_\alpha = 0.2$, (c) for $D_\alpha = 0.3$, (d) for $D_\alpha = 0.4$. The other parameters are $Q = 2$, $\alpha = 2.0$, $a = 0.7$, $b = 0.8$, $S_1 = 1$, $N = 0.02$, $R_m = 1.0$ and $Q_0 = 0.5$.



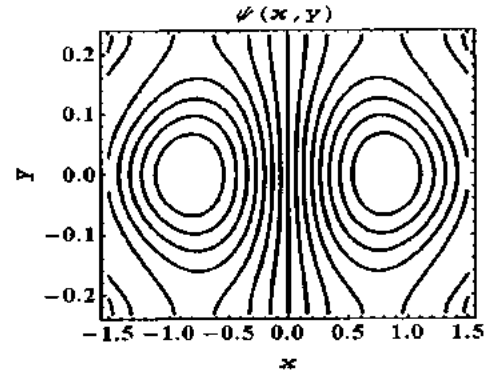
(a)



(b)



(c)



(d)

Figs. 5. 12(a)- 5. 12(d). Stream lines of MWCNT for different values of D_α .

(a) for $D_\alpha = 0.1$, (b) for $D_\alpha = 0.2$, (c) for $D_\alpha = 0.3$, (d) for $D_\alpha = 0.4$. The other parameters are $Q = 2$, $\alpha = 2.0$, $a = 0.7$, $b = 0.8$, $S_1 = 1$, $N = 0.02$, $R_m = 1.0$ and $Q_0 = 0.5$.

5.4 Concluding remarks

In this chapter the communication of carbon nanotubes for the peristaltic flow with induced magnetic field is considered, key points are seen as

- i. It is seen that the impact of nanoparticle volume fraction on pressure gradient is slightest if there should arise an occurrence of SWCNTs though the impact of volume fraction is generally bigger with MWCNTs.
- ii. It is found that pressure gradient diminishes with an expansion in heat generation parameter.
- iii. It is noticed that pressure rise diminishes by expansion in heat flux parameter for SWCNTs and MWCNTs.
- iv. It is observed that axial Induced magnetic field expanding pattern is seen in the inside to right wall of the channel keeping Strommer's number expanded.
- v. It is followed that current density increment as the estimations of magnetic Reynolds number increment.
- vi. It is watched that close to one side and right divider velocity profile is expanding by expansion of Darcy number.
- vii. It is seen that size, of bolus turns out to be small and number of bolus diminishes when we give more prominent qualities to the Strommer's number, for both SWCNTs and MWCNTs.

Chapter 6

Anti-Bacterial applications for new thermal conductivity model in arteries with CNT suspended nanofluid

In this chapter the peristaltic flow of a carbon nanotubes (CNTs) water fluid under the effects of heat generation and magnetic field in permeable vertical diverging tube is studied. The obtained expressions for pressure gradient, pressure rise, temperature, velocity profile are described through graphs for various pertinent parameters. The streamlines are drawn for some physical quantities to discuss the trapping phenomenon. It is observed that pressure gradient profile is decreasing with the increase of Darcy number D_a , because Darcy number is due to porous permeable walls of the tube and when walls are porous fluid cannot easily flow in tube, so that will decrease the pressure gradient.

6.1 Mathematical formulation

Considered peristaltic dynamics of an incompressible SWCNT and MWCNT suspended in water as base fluid through a distensible channel with permeable walls. The flow is generated by sinusoidal wave trains propagating with constant speed c_2 along the walls of the tube. Heat transfer along with nanoparticle phenomena has been taken into account. The wall of the tube is maintaining at temperature \bar{T}_0 and solid nanoparticle volume fraction \bar{C}_0 while at the center we have used symmetry condition on both temperature and solid nanoparticle volume fraction. The geometry of the wall surface is defined as

$$h = a''(Z) + \omega' \sin \frac{2\pi}{\lambda}(Z - c_2 t), \quad (6.1)$$

where $a''(Z) = a_0 + K_1 Z$ is the radius of the tube at any axial distance from inlet also

a_0 is the radius of the inlet, K_1 is a constant whose magnitude depends on the length of the tube, exit and inlet dimensions and ω^* is the wave amplitude. In the presence of MHD, the governing Eqs. (1.39), (1.41) and (1.45) in cylindrical coordinate with the velocity field is $V = (U, 0, W)$ in the component notation are as

$$\frac{1}{R} \frac{\partial(RU)}{\partial R} + \frac{\partial W}{\partial Z} = 0, \quad (6.2)$$

$$\rho_{nf} \left(\frac{\partial U}{\partial t} + U \frac{\partial U}{\partial R} + W \frac{\partial U}{\partial Z} \right) = -\frac{\partial P}{\partial R} + \mu_{nf} \left(\frac{1}{R} \frac{\partial}{\partial R} \left(R \frac{\partial U}{\partial R} \right) - \frac{U}{R^2} + \frac{\partial^2 U}{\partial Z^2} \right) + \rho_{nf} g_r, \quad (6.3)$$

$$\rho_{nf} \left(\frac{\partial W}{\partial t} + U \frac{\partial W}{\partial R} + W \frac{\partial W}{\partial Z} \right) = -\frac{\partial P}{\partial Z} + \mu_{nf} \left(\frac{1}{R} \frac{\partial}{\partial R} \left(R \frac{\partial W}{\partial R} \right) + \frac{\partial^2 W}{\partial Z^2} \right) + \rho_{nf} g_z, \quad (6.4)$$

$$(\rho C_p)_{nf} \left(U \frac{\partial T}{\partial R} + W \frac{\partial T}{\partial Z} \right) = k_{nf} \left(\frac{\partial^2 T}{\partial R^2} + \frac{1}{R} \frac{\partial T}{\partial R} + \frac{\partial^2 T}{\partial Z^2} \right) + Q_0^* (T - T_m). \quad (6.5)$$

The transformations between two frames and dimensionless are

$$\begin{aligned} r &= R, \quad z = Z - c_2 t, \quad u = U, \quad w = W - c_2, \\ \bar{p} &= \frac{a_0^2}{\mu_f c \lambda} p, \quad \bar{u} = \frac{\lambda u}{a_0 c_1}, \quad \bar{w} = \frac{w}{c_2}, \quad \bar{r} = \frac{r}{a_0}, \quad \bar{z} = \frac{z}{\lambda}, \quad t = \frac{c_1}{\lambda} \bar{t}, \quad Q_1 = Q_0^* a_0^2, \\ \text{Re} &= \frac{c_2 a_0}{\nu_f}, \quad \delta = \frac{a}{\lambda}, \quad \bar{\theta} = \frac{T - T_0}{T_1}, \quad \bar{\psi} = \frac{\psi}{c_2 a_0}, \quad \Gamma_1 = \frac{H_1}{a_0}, \quad h_2 = \frac{H_2}{a_0}, \\ Gr &= \frac{\beta^* g \alpha a_0^3}{\nu_f^2} (T_1 - T_0), \quad M = \frac{\sigma_0 B_0^2 a_0^2}{\mu_f}. \end{aligned} \quad (6.6)$$

After using the transformation Eq. (6.6) in Eqs. (6.1) – (6.4) reduce to the following form

$$\frac{1}{r} \frac{\partial(ru)}{\partial r} + \frac{\partial w}{\partial z} = 0, \quad (6.7)$$

$$0 = \frac{\partial p}{\partial r}, \quad (6.8)$$

$$\frac{\partial p}{\partial z} = A^* \frac{1}{r} \frac{\partial}{\partial r} \left[r \left(\frac{\partial w}{\partial r} \right) \right] - M(w+1) + Gr\theta, \quad (6.9)$$

$$0 = k_f \frac{1}{r} \frac{\partial}{\partial r} r \frac{\partial \theta}{\partial r} + Q_1. \quad (6.10)$$

The non-dimensional boundaries will take the form as

$$\frac{\partial w}{\partial r} = 0, \quad \frac{\partial \theta}{\partial r} = 0, \quad \text{at } r = 0. \quad (6.11)$$

$$w = -1 - \frac{\sqrt{D_\alpha}}{\alpha} \frac{\partial w}{\partial r}, \quad \theta = 0, \quad \text{at } r = 1 + \frac{\lambda K_1 z}{a_0} + \omega^* \sin(2\pi z). \quad (6.12)$$

In this chapter conductivity of nanofluid Eq. (1.18) and the effective viscosity of nanofluid Eq. (1.23) are considered. The thermophysical properties, for pure water, SWCNT and MWCNT are listed in table 5.1.

6.2 Solution of the problem

The exact solutions of the Eqs. (6.5) and (6.6) are found as follows:

$$\theta(y) = \left(\frac{\beta(h-r)(h+r)}{4Kf} \right), \quad (6.13)$$

$$w(r) = \frac{\frac{2\sqrt{A}I_0\left(\frac{M}{\sqrt{A}}\right)(\beta G_1(2\alpha A + D_a h M^2) + 2\alpha K f M^2 \frac{dp}{dz})}{D_a M I_1\left(\frac{hM}{\sqrt{A}}\right) + \alpha \sqrt{A} I_0\left(\frac{hM}{\sqrt{A}}\right)} - 4A\beta Gr + M^2 \left(\frac{\beta Gr(h-r)(h+r) -}{4Kf\left(M^2 + \frac{dp}{dz}\right)} \right)}{4KfM^4}, \quad (6.14)$$

$$\frac{dp}{dz} = \left(\frac{2\sqrt{A} \left(\frac{D_a M I_1\left(\frac{hM}{\sqrt{A}}\right) +}{\alpha \sqrt{A} I_0\left(\frac{hM}{\sqrt{A}}\right)} \right) \left(\frac{\beta Gr h^2 (8A - h^2 M^2) +}{8KfM^4 (2F + h^2)} \right) - \right)}{\frac{\beta Gr h^2 (8A + h^2 M^2) (2\alpha A + D_a h M^2)}{2h^2 KfM^2 \left(\frac{8\alpha A - 8\sqrt{A} D_a M I_1\left(\frac{hM}{\sqrt{A}}\right) -}{8\alpha A I_0\left(\frac{hM}{\sqrt{A}}\right) + \alpha h^2 M^2} \right)}} \right). \quad (6.15)$$

The corresponding stream function can be defined as

$$u = -\frac{1}{r} \frac{\partial \psi}{\partial z} \quad \text{and} \quad w = \frac{1}{r} \frac{\partial \psi}{\partial r}. \quad (6.16)$$

The pressure rise Δp is defined as follows

$$\Delta p = \int_0^1 \frac{dp}{dz} dr. \quad (6.17)$$

The flow rate F in non dimensionalized form is given as

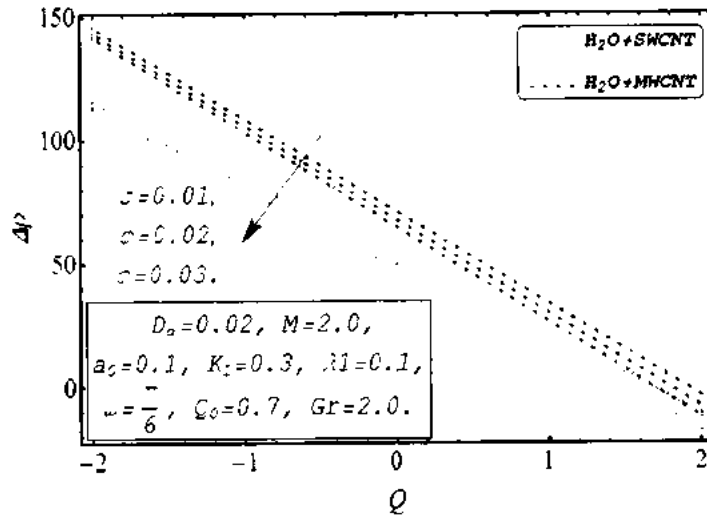
$$F = 2Q - \frac{\omega^2}{2} - 1. \quad (6.18)$$

6.3 Results and discussion

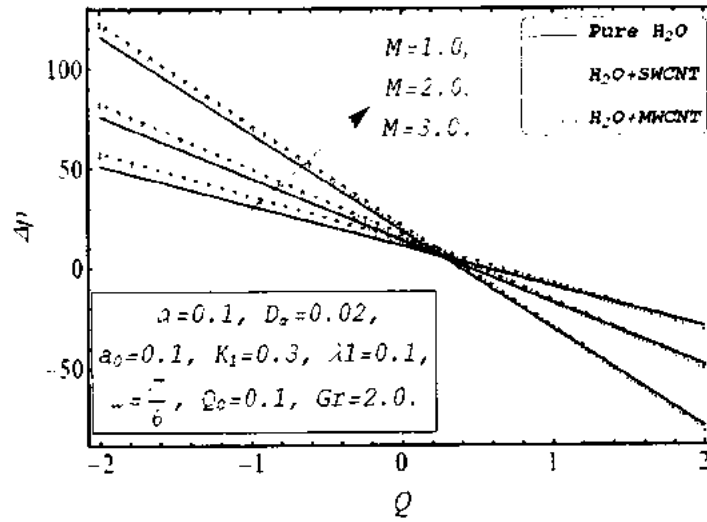
In this section role of Hartmann number, nano particle volume fraction, volume flow rate, Darcy number, heat generation parameter and slip parameter has been carried out for pure water, SWCNT and MWCNT.

Fig. 6.1(a) portrays that as increasing the value of ϕ pressure rise decreases, Fig.

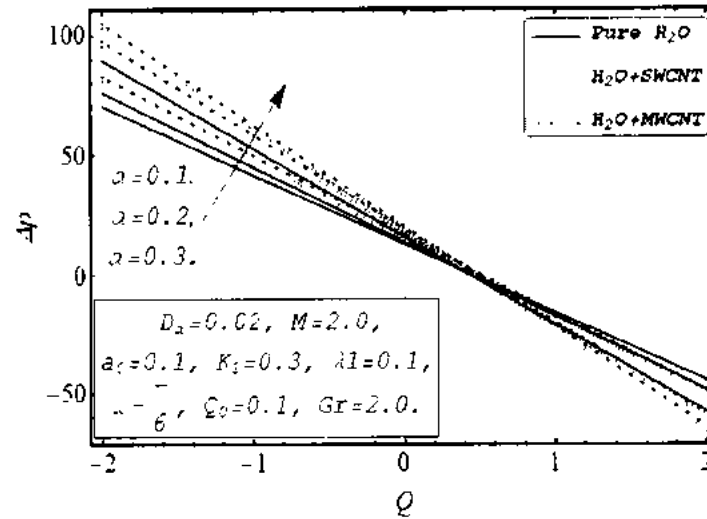
6.1(b) demonstrates that pressure rise increases by expansion in M in the pumping quarter while the inverse conduct is seen in the copumping area. Figs. 6.1(c) – 6.1(d) demonstrates the impact of slip parameter α and Darcy number D_α on pressure rise it is watched that pressure rise is increasing as increasing the value of slip parameter α while pressure rise decreases by increases of Darcy number in the locale retrograde pumping yet Δp appears inverse demeanor in the copumping area. Fig. 6.2(a). shows that increment in the value of ϕ has brought about the expansion of pressure gradient *i.e.*, increasingly the volume fraction more prominent the pressure gradient. The impact of M and α on pressure gradient is appeared in Figs 6.2(b) – 6.2(c), it demonstrates that pressure gradient is increasing on an increasing in M and α for a wide range of fluid it is additionally watched that pressure gradient is minimum in the event pure water where as the impact of M and α is generally bigger if there should arise an occurrence of *SWCNT* and *MWCNT*. Fig. 6.2(d) demonstrates the impact of Darcy number on dp/dz it is watched that pressure gradient is diminishing by expansion of D_α . Figs. 6.3(a) – 6.3(b) to comprehend the variation of temperature for various estimations of ϕ and Q_0 . Fig. 6.3(a) demonstrates that θ . increments as increment of ϕ for *SWCNT* and *MWCNT*. water based fluids. Figs. 6.3(b) have watched that by expanding Q_0 , temperature is expanding for all kind of fluids. It is seen from Fig. 6.4(a) that velocity profile increments with expanding the estimation of ϕ . From Fig. 6.4(b) it portrays that w is diminishing with expansion Hartmann number M . Exhibited the Figs. 6.4(c) – 6.4(d) to acquire the variation of velocity profile for differing the extent of the parameters α and D_α .for a wide range of liquid. It portrays that velocity is diminishing with expansion of α however inverse conduct is seen for D_α . The trapping for various estimation of M and D_α are appeared in the Figs. 6.5(a) – 6.8(d). Figs. 6.5(a) – 6.5(d) and Figs. 6.6(a) – 6.6(d) demonstrate the impact of Hartmann number M on streamlines for *SWCNT* and *MWCNT* respectively it is demonstrated that bolus turns out to be expansive as bigger estimations of M Figs. 6.7(a) – 6.7(d) and Figs. 6.8(a) – 6.8(d) show the effect of Darcy number D_α on streamlines for *SWCNT* and *MWCNT* respectively it is shown that boluses turn out to be small as bigger estimations of D_α .



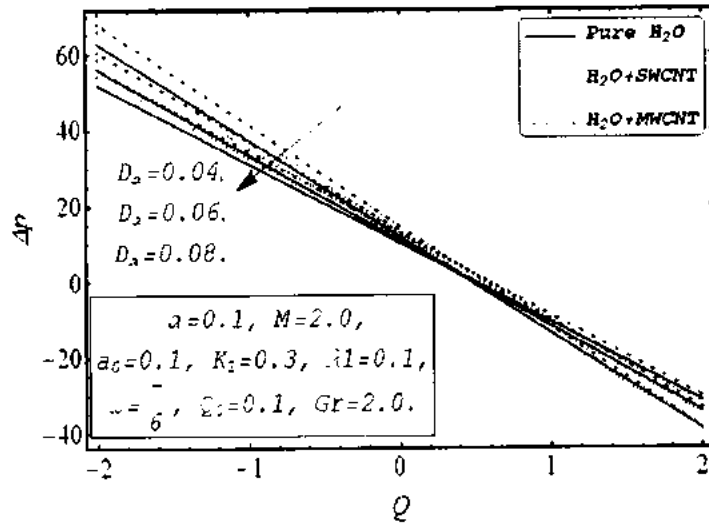
Figs. 6.1(a). Variation of pressure rise Δp for flow parameter ϕ .



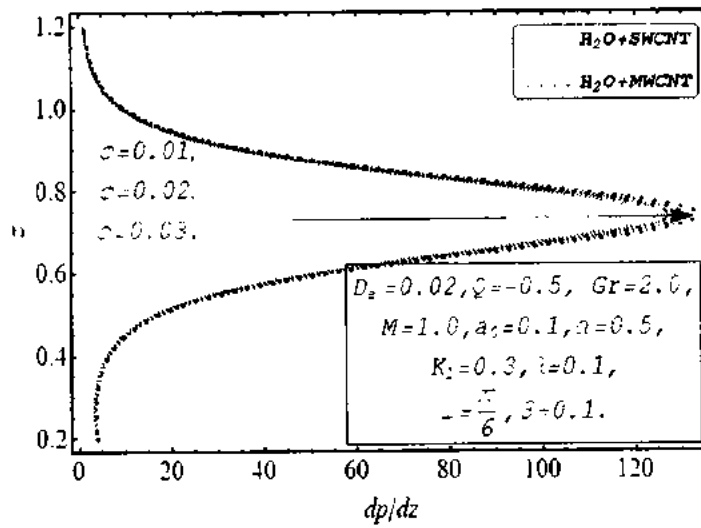
Figs. 6.1(b). Variation of pressure rise Δp for flow parameter M .



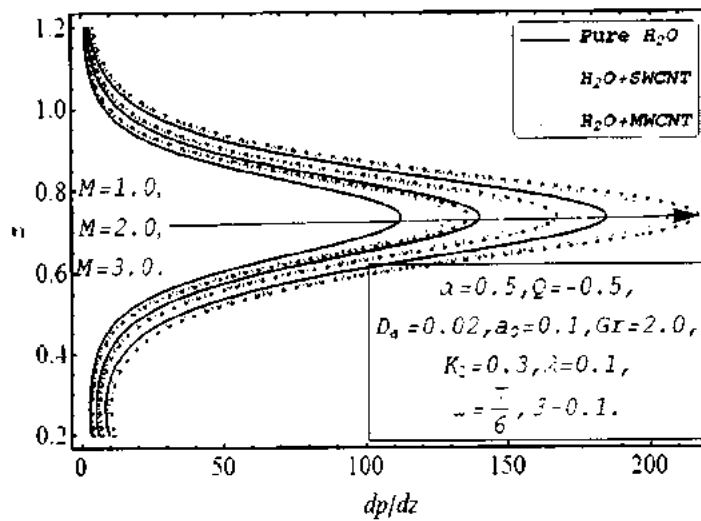
Figs. 6.1(c). Variation of pressure rise Δp for flow parameter α .



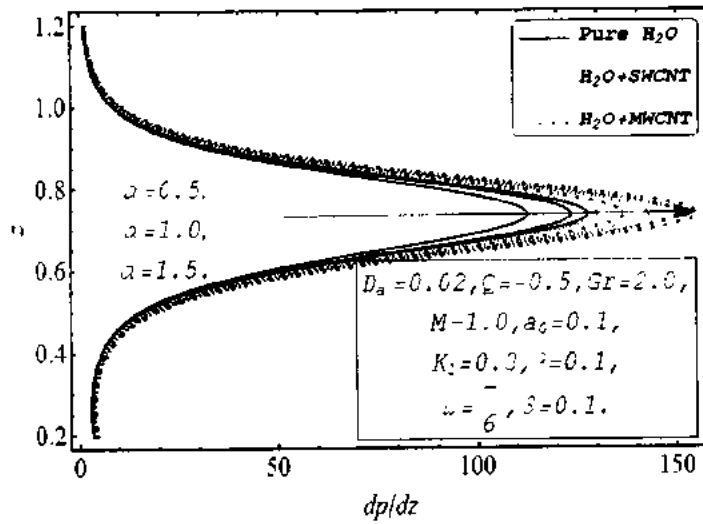
Figs. 6.1(d). Variation of pressure rise Δp for flow parameter D_a .



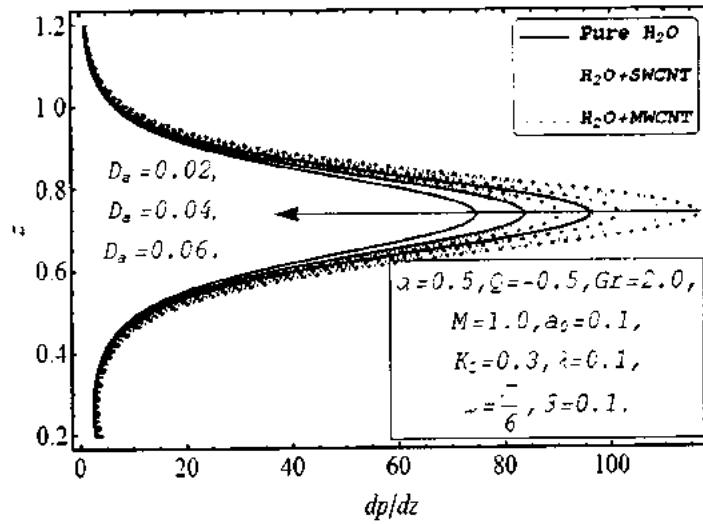
Figs. 6.2(a). Variation of pressure gradient dp/dx for flow parameter ϕ .



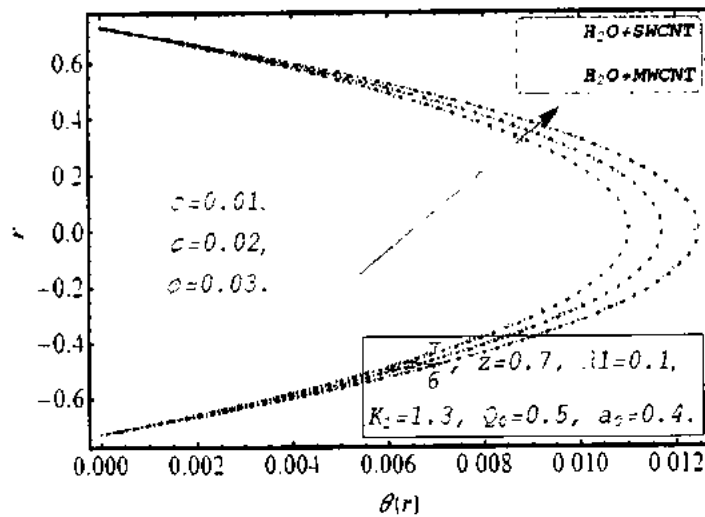
Figs. 6.2(b). Variation of pressure gradient dp/dx for flow parameter M .



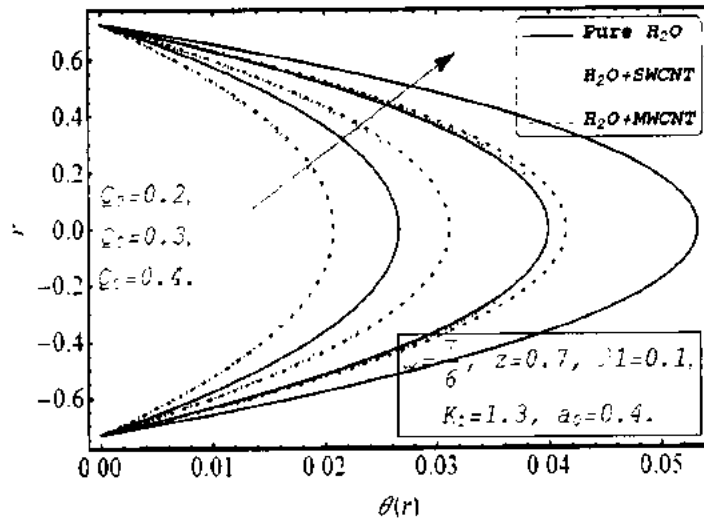
Figs. 6.2(c). Variation of pressure gradient dp/dx for flow parameter α .



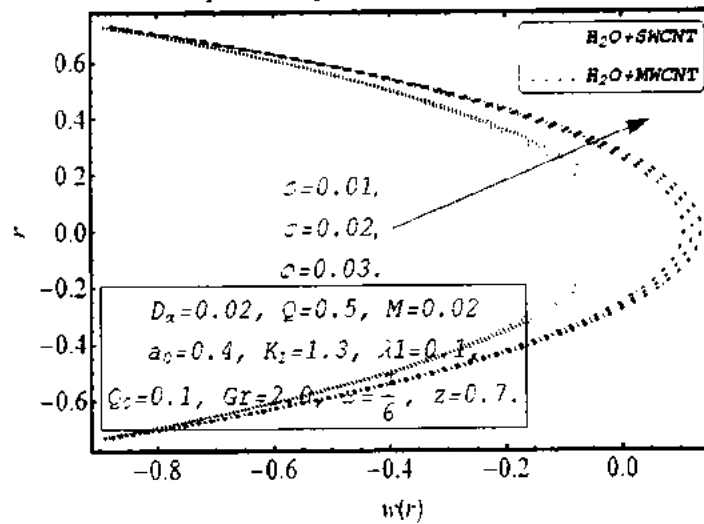
Figs. 6.2(d). Variation of pressure gradient dp/dx for flow parameter D_a .



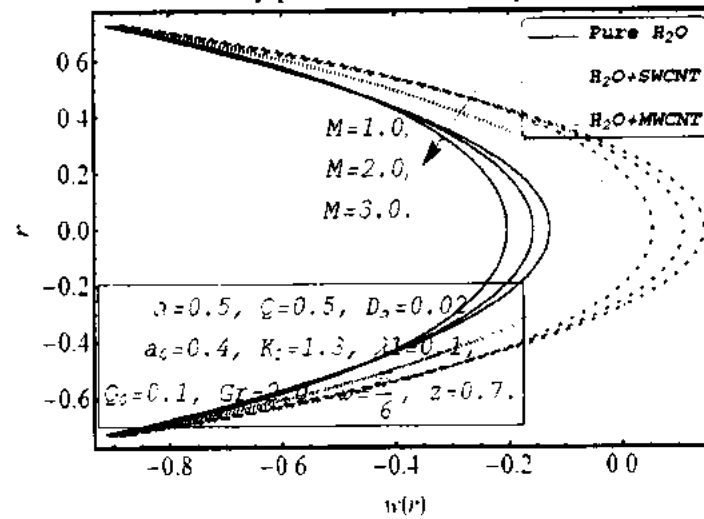
Figs. 6.3(a). Variation of temperature profile θ for flow parameter ϕ .



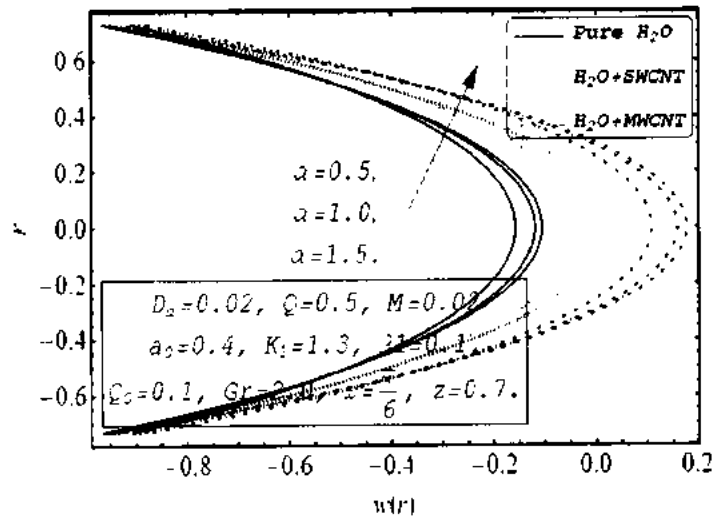
Figs. 6.3(b). Variation of temperature profile θ for flow parameter Q_0 .



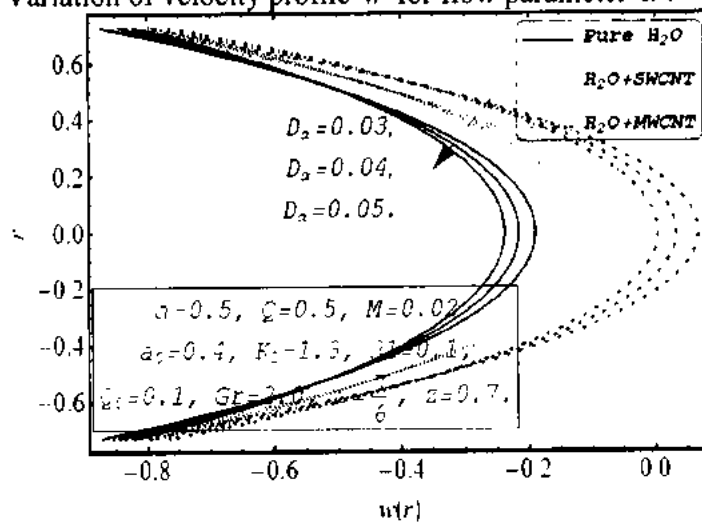
Figs. 6.4(a). Variation of velocity profile w for flow parameter ϕ .



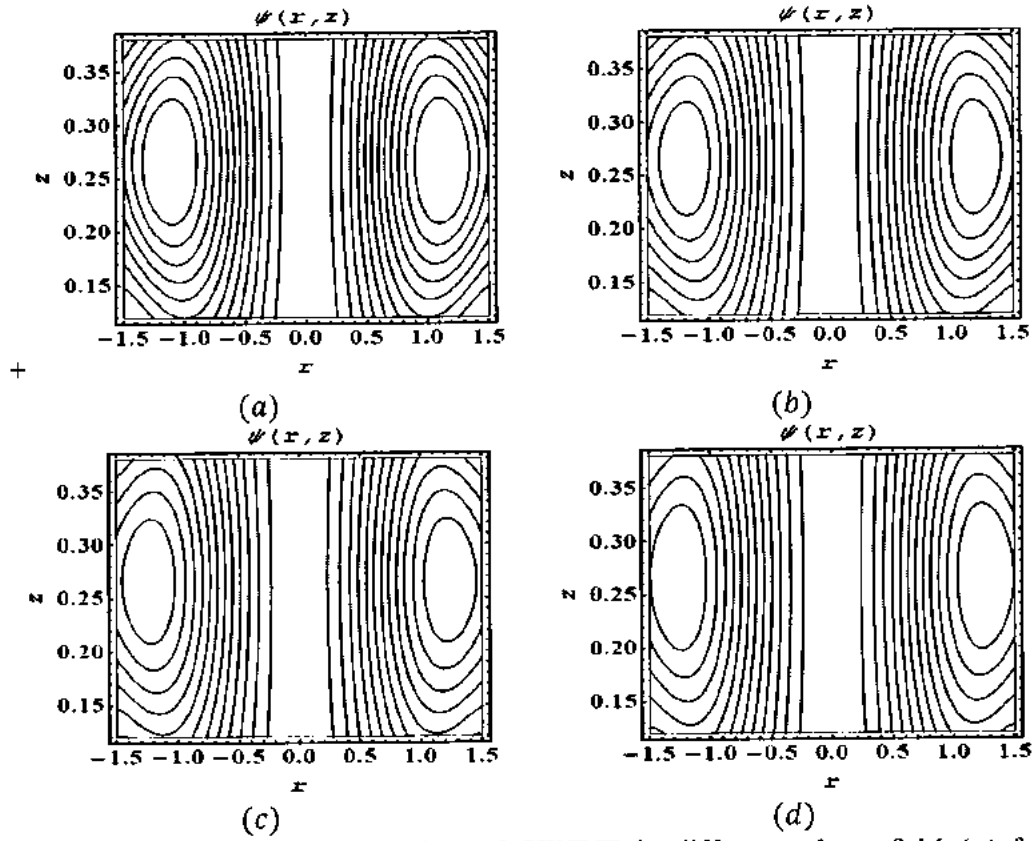
Figs. 6.4(b). Variation of velocity profile w for flow parameter M .



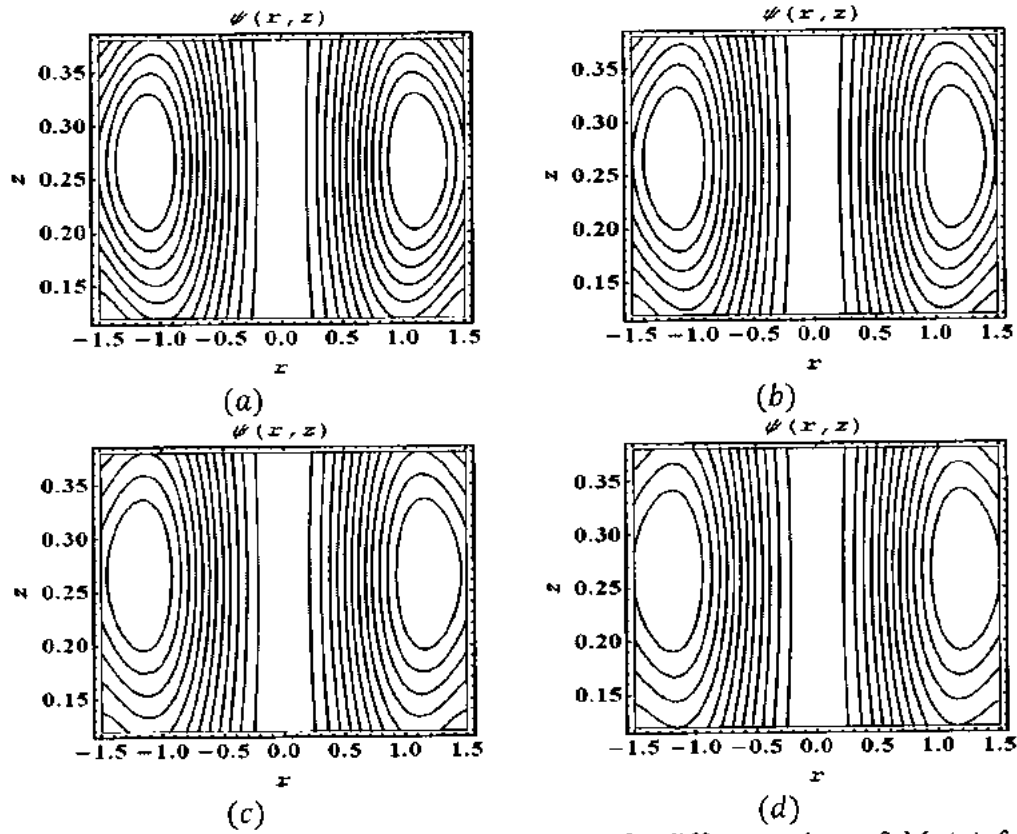
Figs. 6.4(c). Variation of velocity profile w for flow parameter α .



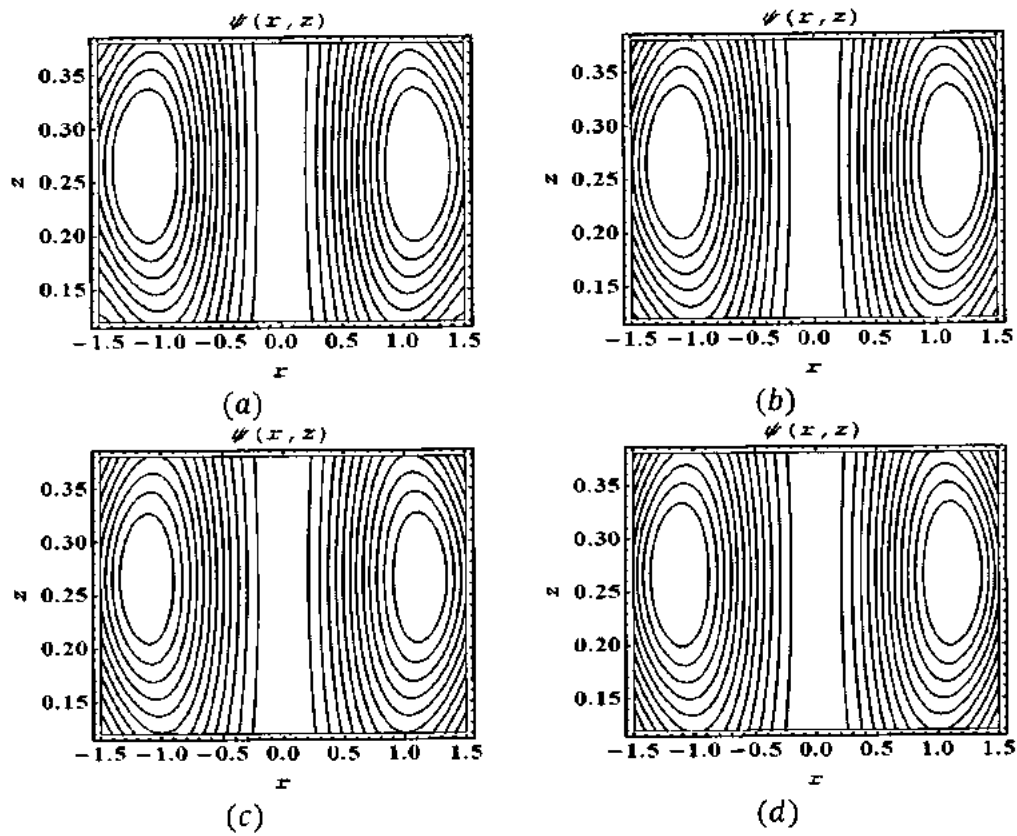
Figs. 6.4(d). Variation of velocity profile w for flow parameter D_α .



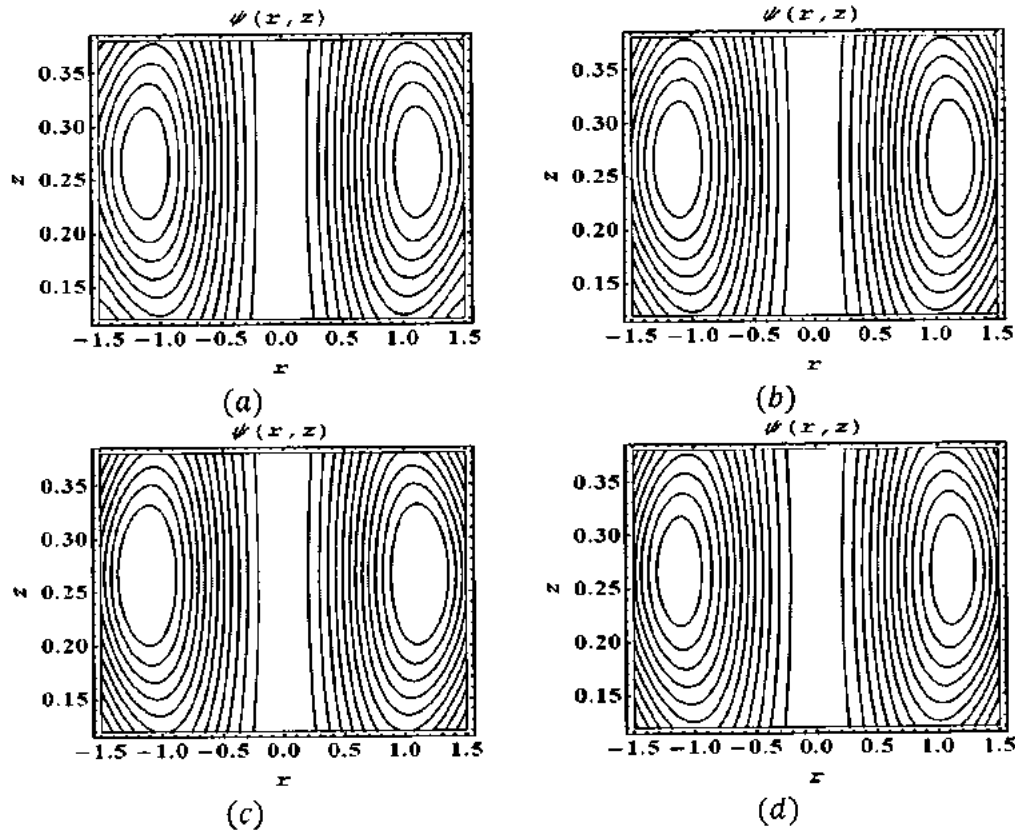
Figs. 6.5(a) – 6.5(d): Stream lines of *SWCNT* for different values of M . (a) for $M = 2.0$, (b) for $M = 3.0$, (c) for $M = 4.0$, (d) for $M = 5.0$. The other parameters are $Q = 2.0$, $\omega = \frac{\pi}{6}$, $D_a = 0.02$, $\alpha = 0.5$, $\phi = 0.05$.



Figs. 6. 6(a) - 6. 6(d): Stream lines of *MWCNT* for different values of M . (a) for $M = 2.0$, (b) for $M = 3.0$, (c) for $M = 4.0$, (d) for $M = 5.0$. The other parameters are $Q = 2.0$, $\omega = \frac{\pi}{6}$, $D_a = 0.02$, $\alpha = 0.5$, $\phi = 0.05$.



Figs. 6.7(a) - 6.7(d). Stream lines of SWCNT for different values of D_a . (a) for $D_a = 0.01$, (b) for $D_a = 0.03$, (c) for $D_a = 0.05$, (d) for $D_a = 0.07$. The other parameters are $Q = 2.0$, $\omega = \frac{\pi}{6}$, $M = 2.0$, $\alpha = 0.5$, $\phi = 0.05$.



Figs. 6.8(a) - 6.8(d). Stream lines of *MWCNT* for different values of D_a . (a) for $D_a = 0.01$, (b) for $D_a = 0.03$, (c) for $D_a = 0.05$, (d) for $D_a = 0.07$. The other parameters are $Q = 2.0$, $\omega = \frac{\pi}{6}$, $M = 2.0$, $\alpha = 0.5$, $\phi = 0.05$.

6.4 Concluding remarks

Association of SWCNT and MWCNT nanoparticles for the peristaltic flow in a penetrable vertical diverging tube with the magnetic field is examined in this chapter.

Key focuses are seen as

- i. It is observed that impact of nanoparticle part on weight angle impressive effect *i.e.*, progressively the volume fraction, more noteworthy the pressure gradient.
- ii. It is calculated that temperature increments as it is increment nanoparticle fraction for SWCNT and MWCNT nanofluid.
- iii. It is noticed that velocity is diminishing with expansion of Hartmann number.
- iv. Velocity is diminishing with expansion of Darcy's number.
- v. It is seen that boluses turn out to be small for bigger estimations of Darcy's number.

Chapter 7

Endoscopic effects with entropy generation analysis in peristalsis for the thermal conductivity of $H_2O + Cu$ nanofluid

In this chapter the peristaltic flow of a copper water fluid investigates the effects of entropy and magnetic field in an endoscope is studied. The obtained expressions for pressure gradient, pressure rise, temperature, velocity phenomenon entropy generation number and Bejan number are described through graphs for various pertinent parameters. The streamlines are drawn for some physical quantities to discuss the trapping phenomenon.

7.1 Mathematical formulation

An incompressible peristaltic flow of copper nanofluid in an endoscope is considered. The flow is generated by sinusoidal wave trains propagating with constant speed c along the walls of the tube. Heat transfer along with Entropy generation phenomena has been taken into account. The inner tube is rigid and maintained at temperature T_0 while the outer tube has a sinusoidal wave traveling down its walls and maintained at temperature T_1 . The geometry of the wall surfaces is defined as

$$\bar{R}_1 = a_1, \quad (7.1)$$

$$\bar{R}_2 = a_2 + b \sin \left[\frac{2\pi}{\lambda} (\bar{Z} - c\bar{t}) \right]. \quad (7.2)$$

In the above equations a_1 is the radius of the inner tube, a_2 is the radius of the outer tube at inlet.

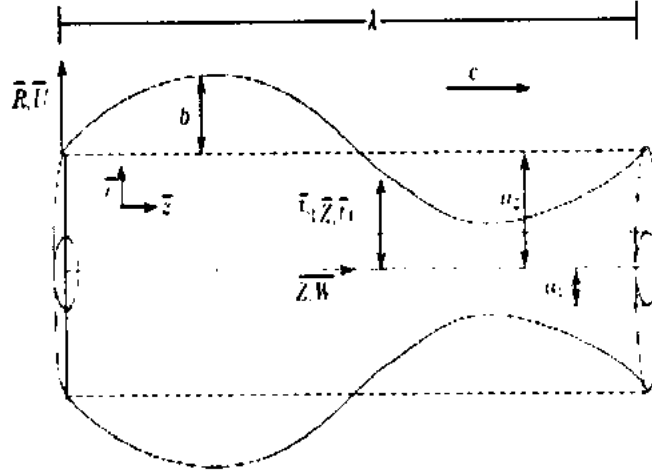


Fig 7.1. Geometry of the problem

In the presence of MHD and entropy, the governing Eqs. (1.19), (1.21) and (1.25) in cylindrical coordinate with the velocity field is $V = (U, 0, W)$ in the component notation can be written as

$$\frac{1}{R} \frac{\partial(RU)}{\partial R} + \frac{\partial W}{\partial Z} = 0, \quad (7.3)$$

$$\rho_{nf} \left(\frac{\partial U}{\partial t} + U \frac{\partial U}{\partial R} + W \frac{\partial U}{\partial Z} \right) = -\frac{\partial P}{\partial R} + \mu_{nf} \left(\frac{1}{R} \frac{\partial}{\partial R} \left(R \frac{\partial U}{\partial R} \right) - \frac{U}{R^2} + \frac{\partial^2 U}{\partial Z^2} \right) + \rho_{nf} g_r, \quad (7.4)$$

$$\rho_{nf} \left(\frac{\partial W}{\partial t} + U \frac{\partial W}{\partial R} + W \frac{\partial W}{\partial Z} \right) = -\frac{\partial P}{\partial Z} + \mu_{nf} \left(\frac{1}{R} \frac{\partial}{\partial R} \left(R \frac{\partial W}{\partial R} \right) + \frac{\partial^2 W}{\partial Z^2} \right) + \rho_{nf} g_z, \quad (7.5)$$

$$(\rho C_p)_{nf} \left(U \frac{\partial T}{\partial R} + W \frac{\partial T}{\partial Z} \right) = k_{nf} \left(\frac{\partial^2 T}{\partial R^2} + \frac{1}{R} \frac{\partial T}{\partial R} + \frac{\partial^2 T}{\partial Z^2} \right) + \frac{\mu_{nf}}{(\rho c_p)_{nf}} \left(\frac{\partial U}{\partial R} + \frac{\partial W}{\partial R} \right)^2. \quad (7.6)$$

After using the transformation Eq. (6.5) in Eqs. (7.3)–(7.6), we have

$$\frac{\partial u}{\partial r} + \frac{u + \partial w}{r \partial z} = 0, \quad (7.7)$$

$$\frac{\partial p}{\partial r} = 0, \quad (7.8)$$

$$\frac{dp}{dz} = A * \frac{1}{r} \frac{\partial}{\partial r} \left(r \frac{\partial w}{\partial r} \right) - M^2 (w+1), \quad (7.9)$$

$$Kf * \frac{1}{r} \frac{\partial}{\partial r} \left(r \frac{\partial \theta}{\partial r} \right) + B, A * \left(\frac{\partial w}{\partial r} \right)^2 = 0. \quad (7.10)$$

The non-dimensional boundaries will take the following form

$$w = -1, \text{ at } r = r_1, \quad (7.11)$$

$$w = -1, \text{ at } y = r_2 = 1 + \omega \sin(2\pi z). \quad (7.12)$$

$$\theta = 0 \text{ at } r = r_1, \quad \theta = 1 \text{ at } r = r_2. \quad (7.13)$$

The thermophysical properties, for pure water, copper is listed in table 3.1.

Entropy generation in cylindrical form can be defined as

$$S_G = \frac{k_{nf}}{T_0} \left(\left(\frac{\partial T}{\partial R} \right)^2 + \left(\frac{\partial T}{\partial z} \right)^2 \right) + \frac{\mu_{nf}}{T_0} \left(2 \left(\left(\frac{\partial U}{\partial R} \right)^2 + \frac{1}{R^2} U^2 + \left(\frac{\partial W}{\partial Z} \right)^2 \right) + \left(\frac{\partial W}{\partial R} + \frac{\partial U}{\partial Z} \right)^2 \right). \quad (7.14)$$

Dimensionless form of the entropy generation with the help of Eq. (10) due to fluid friction and magnetic field is given as:

$$N_s = \frac{S_G}{S_{G_0}} = \frac{k_{nf}}{k_f} \left(\frac{\partial \theta}{\partial r} \right)^2 + \Lambda Br \left(\frac{\partial w}{\partial r} \right)^2. \quad (7.15)$$

The dimensionless form of S_G is known as entropy generation number N_s which is the ratio of actual entropy generation rate to the characteristic entropy transfer rate S_{G_0} , which is defined as follows

$$S_{G_0} = \frac{k_f (T_1 - T_0)^2}{T_0 a_2^2}, \quad B_r = \frac{\mu_f c^2}{k_f (T_1 - T_0)}, \quad \Lambda = \frac{T_0}{(T_1 - T_0)}. \quad (7.16)$$

Eq. (7.14) consists of two parts. The first part is the entropy generation due to finite temperature difference (N_{scond}) and the second part is the entropy generation due to viscous effects (N_{svisc}). The Bejan number is defined as

$$B_e = \frac{N_{scond}}{N_{scond} + N_{svisc}}. \quad (7.17)$$

7.2 Solution of the problem

The exact solutions of the Eqs. (7.14) and (7.15), are found as

$$w(r) = C_{53} J_0 \left(\frac{iMr}{\sqrt{A}} \right) + C_{54} Y_0 \left(-\frac{iMr}{\sqrt{A}} \right) - \frac{M^2 + \frac{dp}{dz}}{M^2}, \quad (7.18)$$

where

$$C_{53} = \frac{\frac{dp}{dz} \left(Y_0 \left(-\frac{iMr}{\sqrt{A}} \right) - Y_0 \left(-\frac{iMr_2}{\sqrt{A}} \right) \right)}{M^2 \left(\begin{array}{l} Y_0 \left(-\frac{iMr_1}{\sqrt{A}} \right) J_0 \left(\frac{iMr_2}{\sqrt{A}} \right) - J_0 \left(\frac{iMr_1}{\sqrt{A}} \right) \\ Y_0 \left(-\frac{iMr_2}{\sqrt{A}} \right) \end{array} \right)}, \quad (7.19)$$

$$C_{s4} = \frac{\frac{dp}{dz} \left(J_0 \left(\frac{iMr1}{\sqrt{A}} \right) - J_0 \left(\frac{iMr2}{\sqrt{A}} \right) \right)}{M^2 \left(\begin{array}{l} J_0 \left(\frac{iMr1}{\sqrt{A}} \right) Y_0 \left(-\frac{iMr2}{\sqrt{A}} \right) - Y_0 \left(-\frac{iMr1}{\sqrt{A}} \right) \\ J_0 \left(\frac{iMr2}{\sqrt{A}} \right) \end{array} \right)}, \quad (7.20)$$

$$\left. \begin{array}{l} M \left(\begin{array}{l} C_{s3} Mr1^2 {}_0\tilde{F}_1 \left(2, \frac{Mr1^2}{4} \right) - C_{s4} Mr2^2 {}_0\tilde{F}_1 \left(2, \frac{Mr2^2}{4} \right) + 2F * M - \\ Mr1^2 + Mr2^2 \end{array} \right) + \\ \frac{dp}{dz} = \frac{2iM \left(\sqrt{A} C_{s4} r1 Y_1 \left(-\frac{iMr1}{\sqrt{A}} \right) - \sqrt{A} C_{s4} r2 Y_1 \left(-\frac{iMr2}{\sqrt{A}} \right) \right)}{r1^2 - r2^2} \end{array} \right\} \quad (7.21)$$

The corresponding stream function be defined in Eq.(6.19) and pressure rise Δp is defined in Eq. (6.20)

The flow rate F in non dimensionalized form is given as

$$F = 2Q - \frac{\omega^2}{2} - 1. \quad (7.22)$$

7.3 Results and discussion

In this section the conduct of the arrangements is talked about as graphs, for a few estimations of correlated parameter did for both pure water and copper water. Fig. 7.2(a) shows that as increasing the values of ϕ pressure rise increases in the retrograde district, however Δp increases in the co-pumping locale, Fig. 7.2(b) demonstrates the impact of M on pressure rise, it is watched that pressure rise increases by increasin in M in the retrograde region while the inverse conduct is seen in the co-pumping region. From Fig. 7.3(a). It is seen, that increment in the estimation of ϕ has brought about the diminishing of dp/dz i.e., increasingly the volume fraction lesser the pressure gradient, additionally, it is likewise watched that the impact of ϕ other than the tube divider is not impressive. The variation of flow rate and M on pressure gradient is appeared in Figs. 7.3(b) – 7.3(c), it demonstrates that dp/dz is diminishing on an expansion in Q and M for both sorts of fluid, it is likewise watched that pressure gradient is minimum if there should be an occurrence of copper water where as the impact of Q and M is moderately bigger if there should be an occurrence of pure water. Fig. 7.4(a) demonstrates that θ increments as expansion ϕ for copper water liquid.

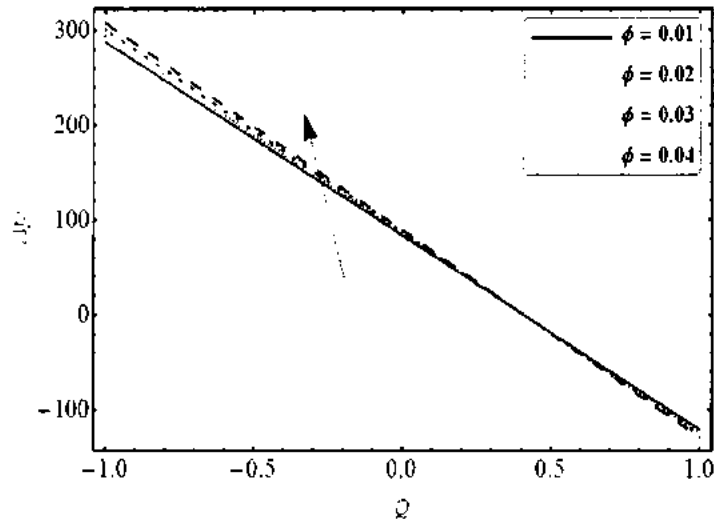
From Figs. 7.4(b) – 7.4(c) same pattern is watched for Hartmann number and Brinkman number separately, it has watched that by expanding M and Br temperature is also expanding.

It is seen from Fig. 7.5(a) that velocity profile increments with expansion in the estimation of ϕ close to the wall of external tube. In any case, inverse conduct is appeared close to the divider internal, *i.e.*, alongside the sinusoidal divider, volume fraction builds the velocity of fluid. It has introduced the Figs. 7.5(b) to get the variation of velocity profile w for differing the extent of the parameters M for both sorts of fluid. It portrays that velocity is diminishing with expansion of M along the external tube's divider, yet inverse conduct is appeared along the unbending barrel's divider. Fig. 7.5(c) demonstrates the variation of average flow rate Q on velocity profile it portrays that velocity increments with an expansion in Q , it is additionally watched that there is minimal impact of Q on velocity on account of copper water as contrast with unadulterated water.

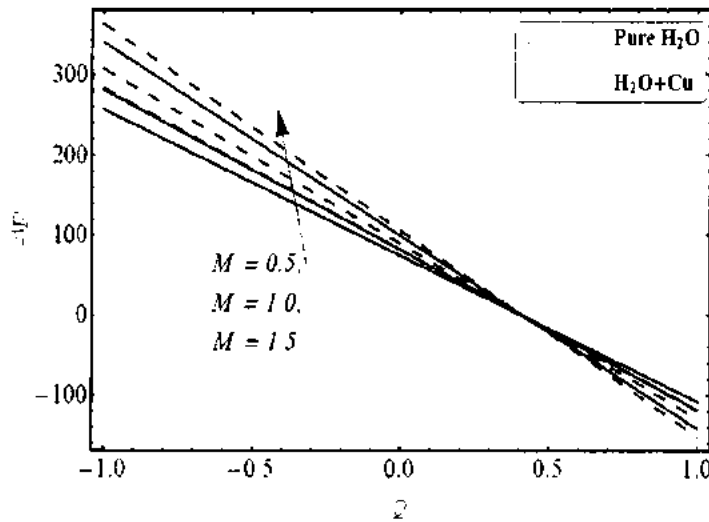
From Fig. 7.6(a) it delineates that entropy generation is expanding with expansion nanoparticle volume fraction parameter ϕ . Figs. 7.6(b) – 7.6(c) demonstrates that N_s is straightforwardly relative to the M and Br all through the channel yet impressive effect is not saw along the dividers for both sorts of fluid in the event of Hartmann number and the effect of copper water is watched more than pure water. In any case Fig. 7.6(d) demonstrates the higher estimation of Λ presentations minimum entropy. Fig. 7.7(a) portrays that with the expansion in ϕ there is an expansion in Bejan number. Fig. 7.7(b) demonstrates the variation of Bejan number for various estimations of M one can see that close to the external divider Bejan number is not affected to significant degree while close to the internal wall of geometry Bejan number is diminishing by expansion in the estimations of M . Fig. 7.7(c) demonstrates that there is an inverse conduct for Br as seen for M . It has seen in Fig. 7.7(d) that B_e is expanding by expansion in Λ yet the effect on copper water is more prominent than the effect of unadulterated water.

Fig. 7.8(a) – 7.7(d) show form contour maps for the streamlines with four estimations of ϕ for copper water. It is seen that bolus gets to be smaller when it given the more noteworthy estimations of ϕ , Figs. 7.9(a) – 7.10(d) demonstrate the impact

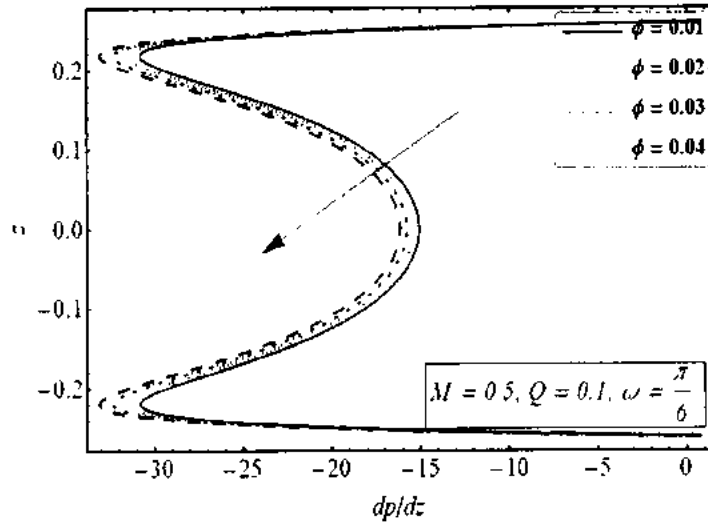
of Hartmann number on streamlines for unadulterated water and copper water separately it is demonstrated that bolus turns out to be expansive as bigger estimations of M . Figs. 7.11(a) – 7.12(d) demonstrate the impact of flow rate Q on streamlines for pure water and copper water separately it is demonstrated that bolus turns out to be huge as bigger estimations of Q .



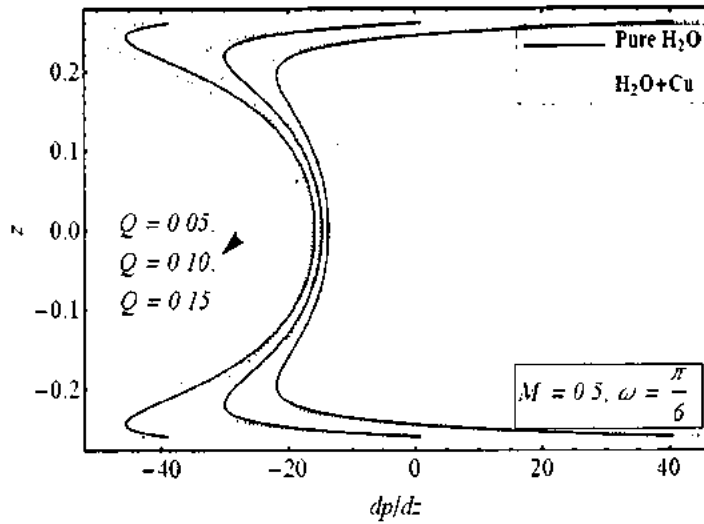
Figs. 7.2(a). Variation of pressure rise Δp for different flow parameter ϕ .



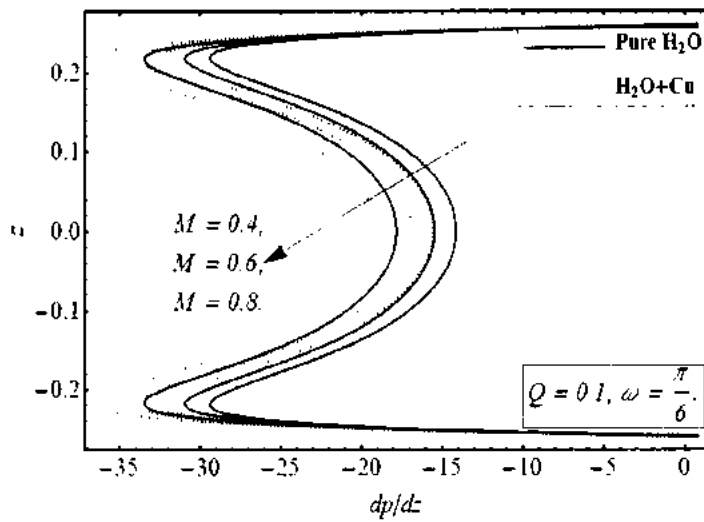
Figs. 7.2(b). Variation of pressure rise Δp for different flow parameter M .



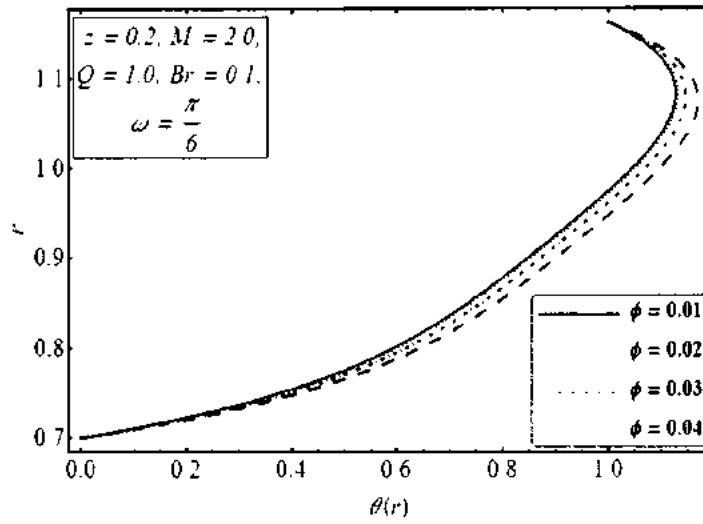
Figs. 7.3(a). Variation of pressure gradient dp/dz for flow parameter ϕ .



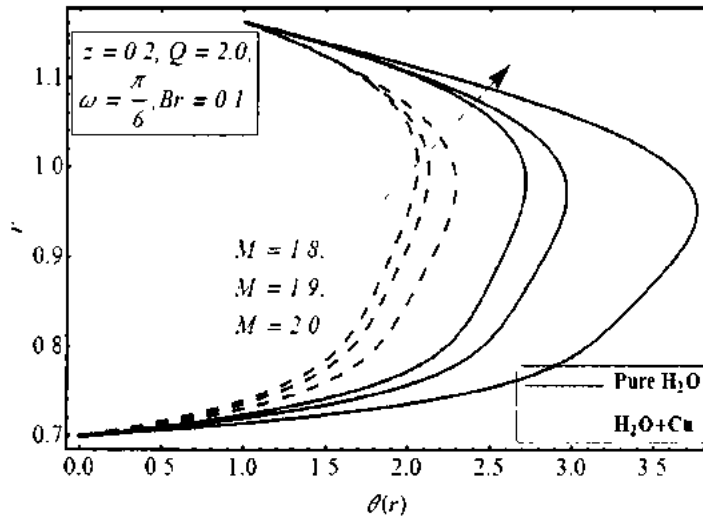
Figs. 7.3(b). Variation of pressure gradient dp/dz for flow parameter Q .



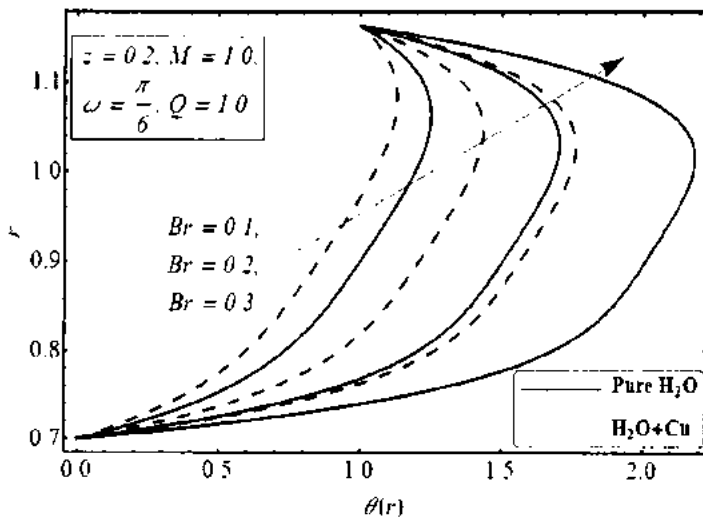
Figs. 7.3(c). Variation of pressure gradient dp/dz for flow parameter M .



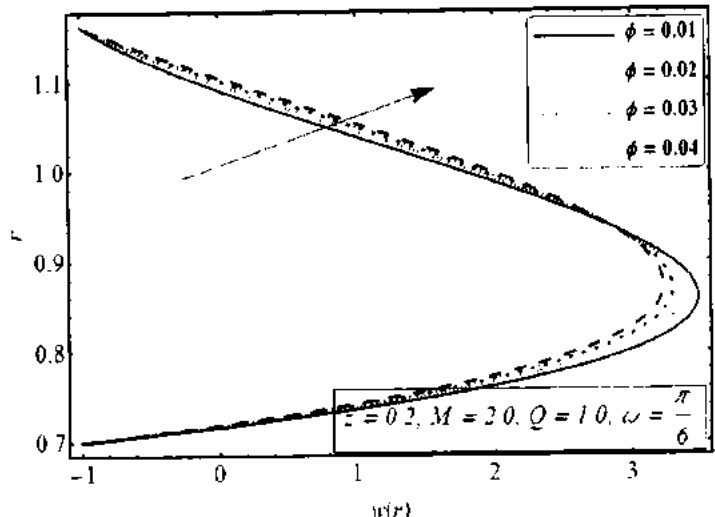
Figs. 7.4(a). Variation of temperature profile θ flow parameter ϕ .



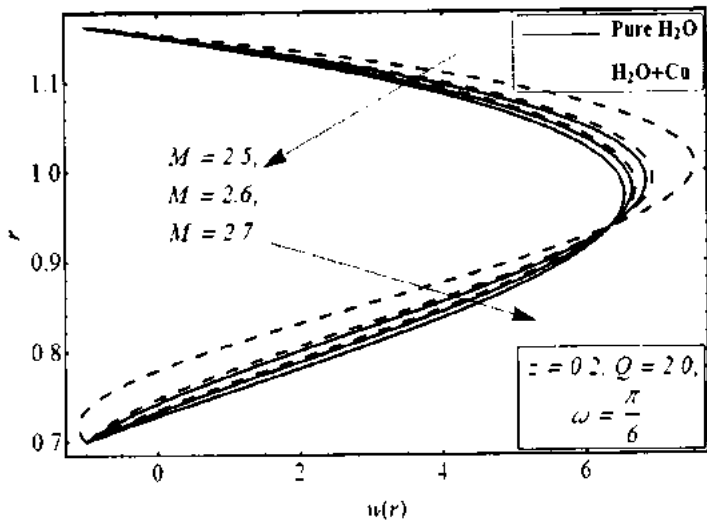
Figs. 7.4(b). Variation of temperature profile θ flow parameter M .



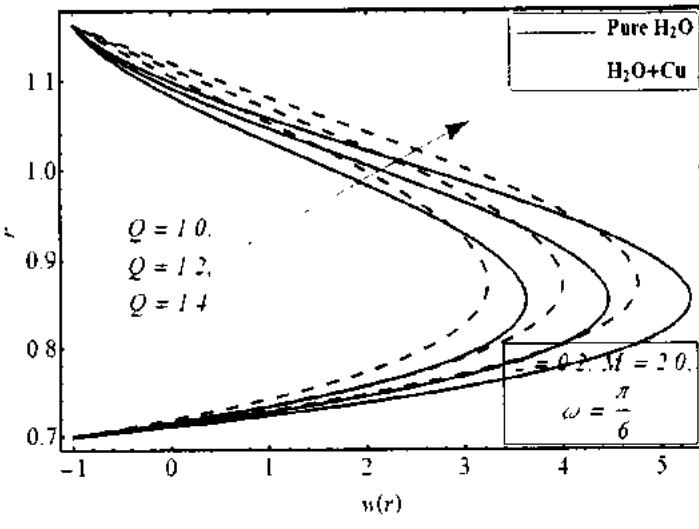
Figs. 7.4(c). Variation of temperature profile θ flow parameter Br .



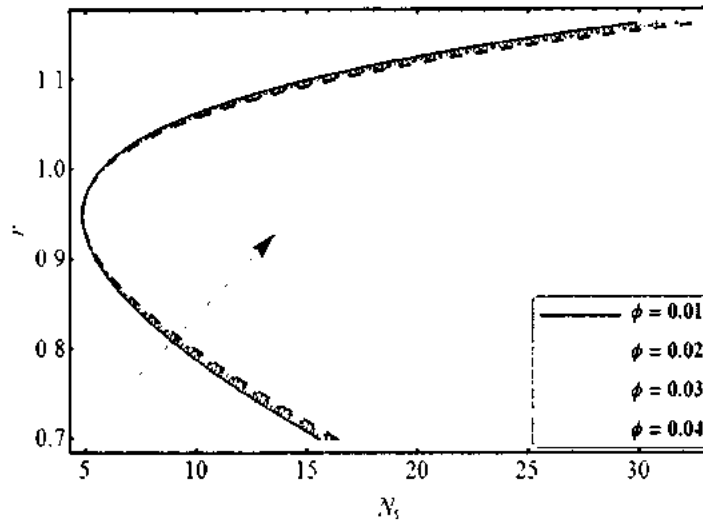
Figs. 7.5(a). Variation of velocity profile w for flow parameter ϕ .



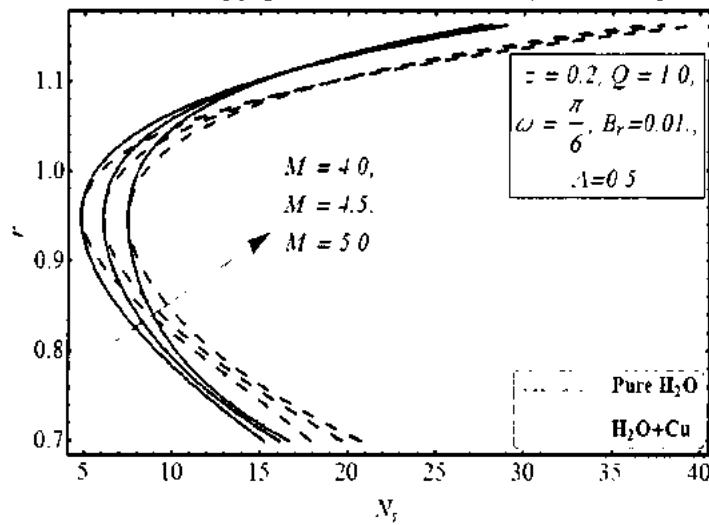
Figs. 7.5(b). Variation of velocity profile w for flow parameter M .



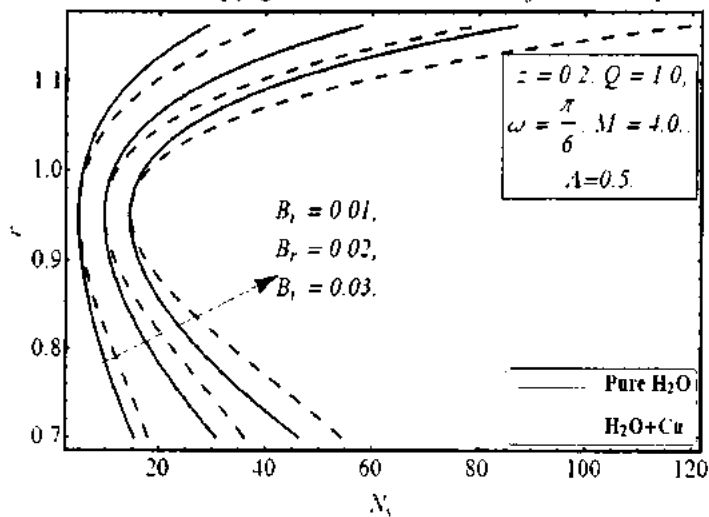
Figs. 7.5(c). Variation of velocity profile w for flow parameter Q .



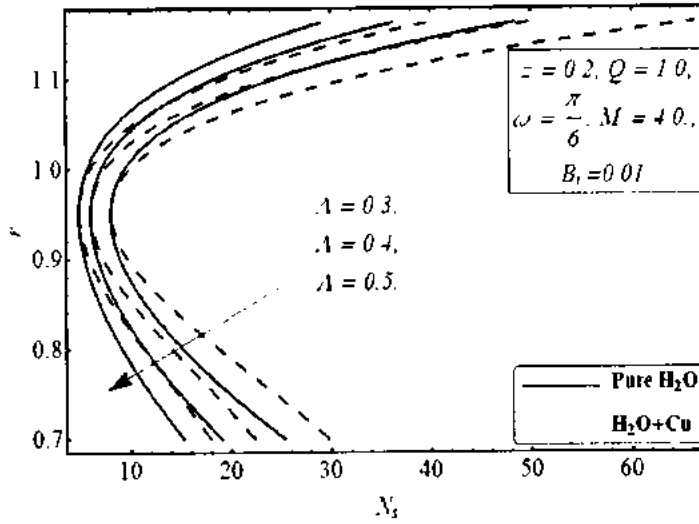
Figs. 7.6(a). Variation of entropy generation number N_s for flow parameter ϕ .



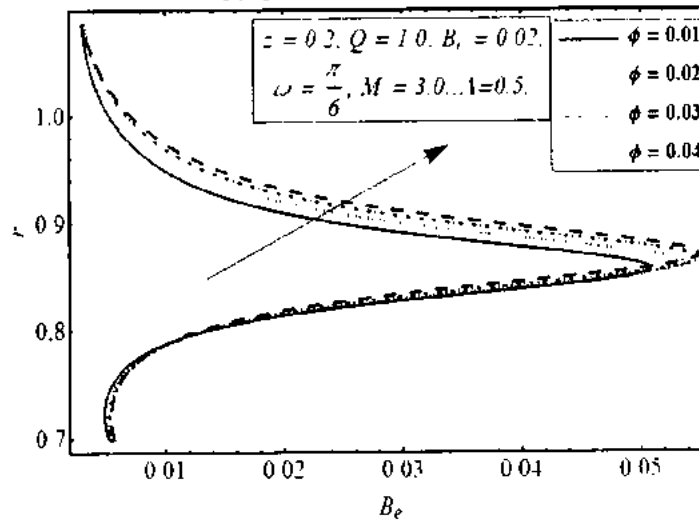
Figs. 7.6(b). Variation of entropy generation number N_s for flow parameter M .



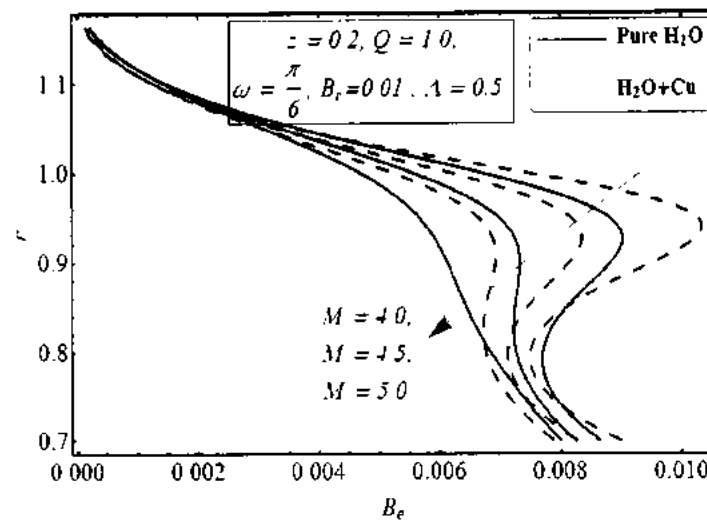
Figs. 7.6(c). Variation of entropy generation number N_s for flow parameter B_r .



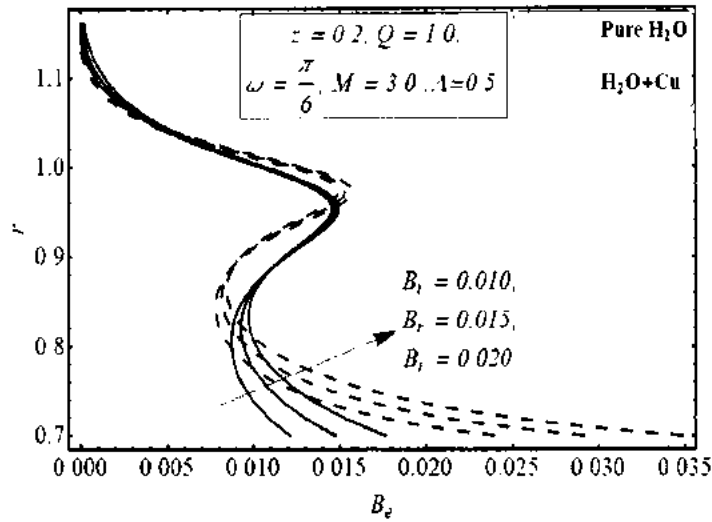
Figs. 7.6(d). Variation of entropy generation number N_s for flow parameter Λ .



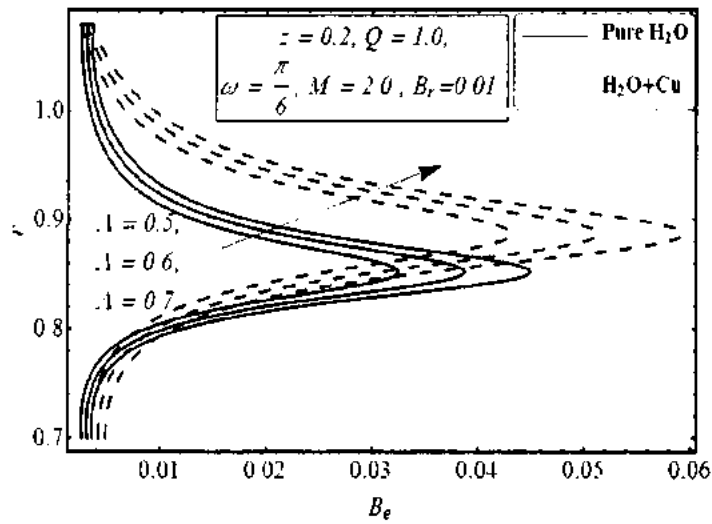
Figs. 7.7(a). Variation of Bejan number B_e for flow parameter ϕ .



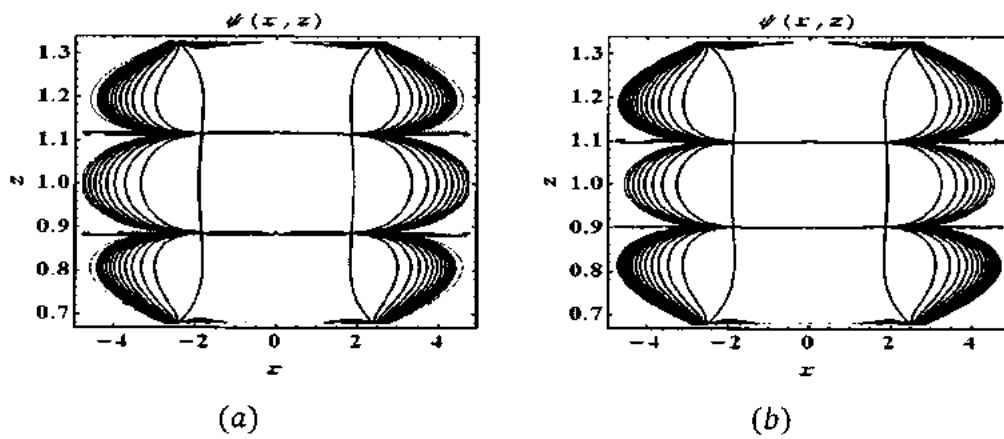
Figs. 7.7(b). Variation of Bejan number B_e for flow parameter M .

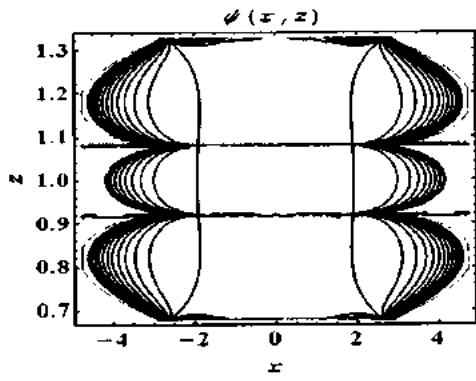


Figs. 7.7(c). Variation of Bejan number B_e for flow parameter B_r .

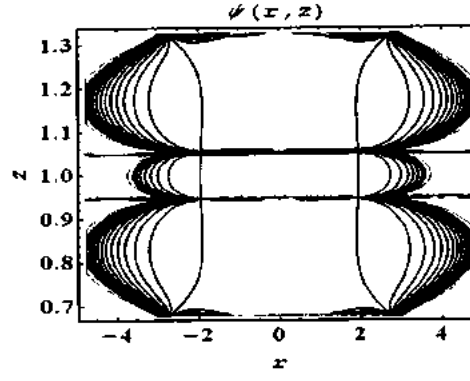


Figs. 7.7(d). Variation of Bejan number B_e for flow parameter Λ .



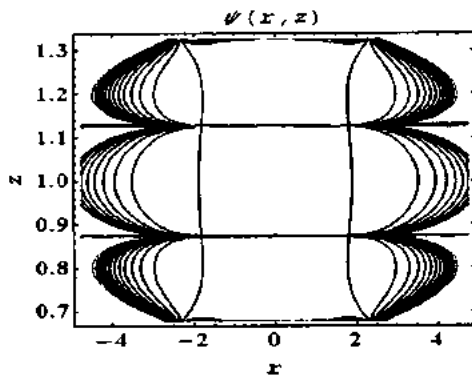


(c)

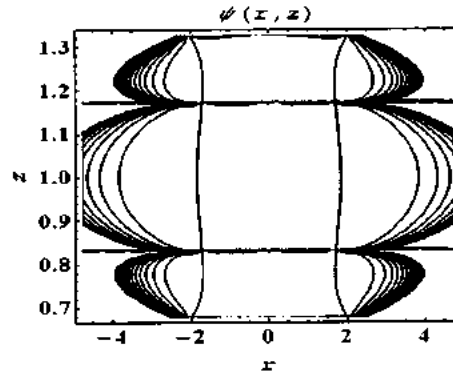


(d)

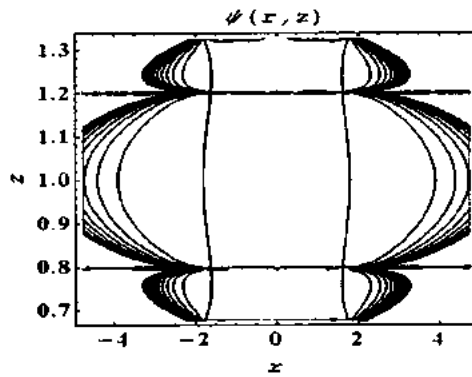
Figs. 7.8(a) - 7.8(d). Stream lines of $H_2O + Cu$ for different values of ϕ . (a) for $\phi = 0.01$, (b) for $\phi = 0.02$, (c) for $\phi = 0.03$, (d) for $\phi = 0.04$. The other parameters are $Q = 1.0$, $M = 2.0$, $\omega = \frac{\pi}{6}$.



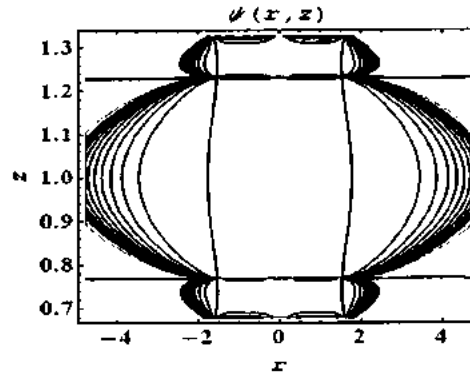
(a)



(b)

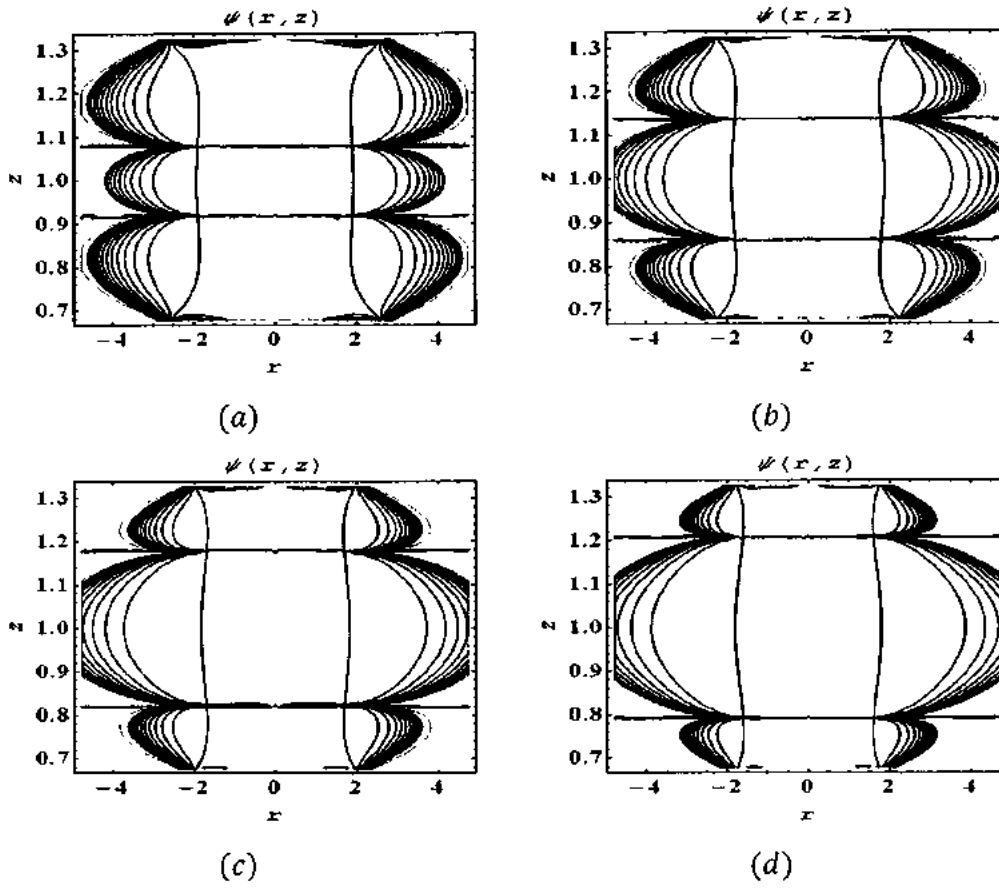


(c)

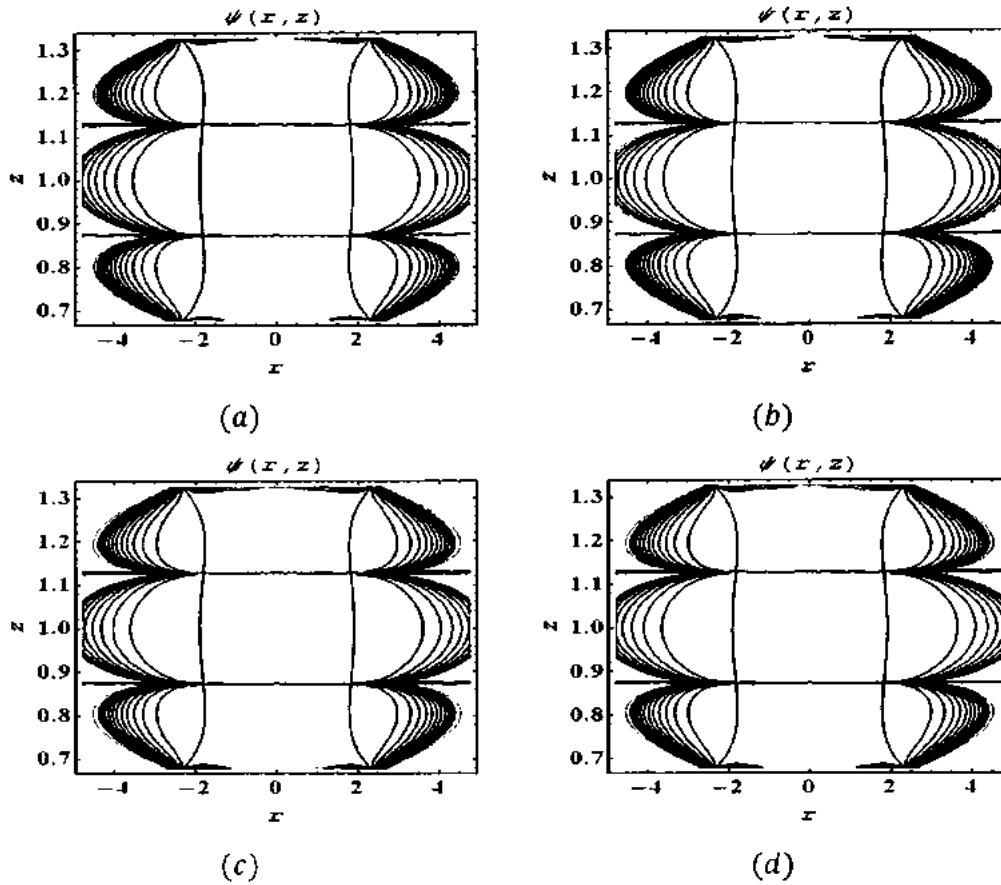


(d)

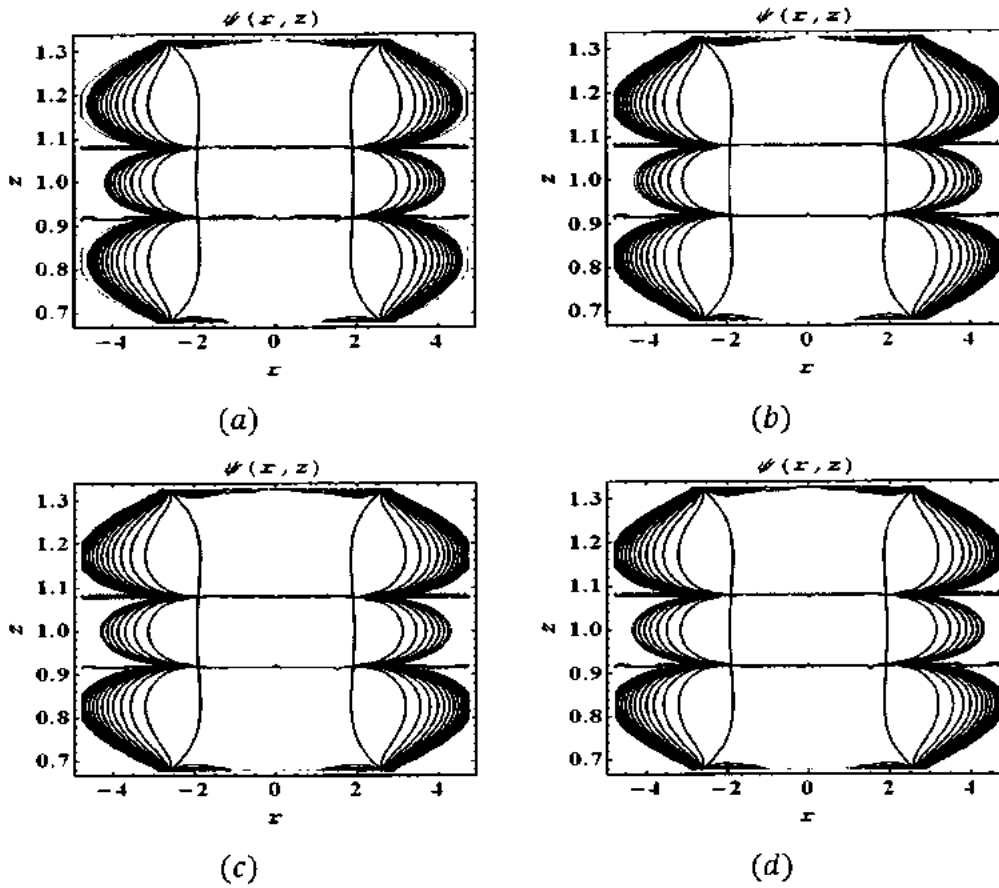
Figs. 7.9(a) - 7.9(d). Stream lines of Pure H_2O for different values of M . (a) for $M = 2.0$, (b) for $M = 2.1$, (c) for $M = 2.2$, (d) for $M = 2.2$. The other parameters are $Q = 1.0$, $\omega = \frac{\pi}{6}$.



Figs. 7.10(a)- 7.10(d). Stream lines of H_2O+Cu for different values of M . (a) for $M = 2.0$, (b) for $M = 2.1$, (c) for $M = 2.2$, (d) for $M = 2.2$. The other parameters are $Q = 1.0$, $\omega = \frac{\pi}{6}$.



Figs. 7.11(a) - 7.11(d). Stream lines of pure H_2O for different values of Q . (a) for $Q = 1.0$, (b) for $Q = 1.5$, (c) for $Q = 2.0$, (d) for $Q = 2.5$. The other parameters are $M = 2.0$ $\omega = \frac{\pi}{6}$.



Figs. 7.12(a) - 7.12(d). Stream lines of $H_2O + Cu$ for different values of Q . (a) for $Q = 1.0$, (b) for $Q = 1.5$, (c) for $Q = 2.0$, (d) for $Q = 2.5$. The other parameters are $M = 2.0$, $\omega = \frac{\pi}{6}$.

7.4 Concluding remarks

Interaction of copper nanoparticles for the peristaltic flow in endoscope with the magnetic field are discussed. Key points are as follows:

- i. It is seen that impact of nanoparticle fraction on pressure gradient extensive effect *i.e.*, progressively the volume fraction, lesser the pressure gradient.
- ii. It is calculated that temperature increments as it has build Brinkman number and Hartmann number for both sorts of fluid.
- iii. Velocity is diminishing with expansion of M along the sinusoidal divider, yet inverse conduct is appeared along the inflexible tube's divider.
- iv. It is noticed that Entropy generation number are expanding with expansion of Brinkman number.
- v. It is noticed that close to the sinusoidal divider Bejan number is not impacted to significant degree while close to the inflexible divider Bejan number is diminishing by expansion in the estimations of Hartmann number.
- vi. It is seen that size, of bolus gets to be smaller when it has given more prominent estimations of nanoparticle volume fraction for copper water.

References

- [1]. T.W, Latham, Fluid Motion in a Peristaltic Pump, Massachusetts Institute of Technology. Dept. of Mechanical Engineering. Cambridge, Msc. Thesis, (1966).
- [2]. A. H. Shapiro, Pumping and retrograde diffusion in peristaltic waves, Proc. Workshop in Ureteral Reflux in Children, Washington DC, (1967) 09 – 126.
- [3]. Y. C. Fung, C. S. Yih, Peristaltic transport, Journal of Applied Mechanics, 35 (1968) 669 – 675.
- [4]. G. Radhakrishnamacharya, Long wave length approximation to peristaltic motion of power law fluid, Rheologica Acta, 21 (1982) 30 – 35.
- [5]. M. Mishra, A. R. Ramachandra, Peristaltic transport of a Newtonian fluid in an Asymmetric channel, Zeitschrift für angewandte Mathematik und Physik, 54 (2003) 532 – 550.
- [6]. S.U.S. Choi, Developments and applications of non-Newtonian flows, ASME FED, 66 (1995) 99 – 105.
- [7]. K. Khanafer, K.Vafai, L. Marilyn, Buoyancy-driven heat transfer enhancement in a two-dimensional enclosure utilizing nanofluids, International Journal of Heat and Mass Transfer, 46 (2003) 3639 – 3656,
- [8]. S. K. Das, S. U. S. Choi, W. Yu, T. Pradeep, Nanofluids Science and Technology, John Wiley, 396 (2008).
- [9]. D. C. Tretheway, C. D. Meinhart, Apparent fluid slip at hydrophobic microchannel walls, Physics of Fluids, 14 (2002) 9 – 12.
- [10]. E. F. El-Shehawy, N. T. El-Dabe, I. M. El-Desoky, Slip effects on the peristaltic flow of a non-Newtonian Maxwellian fluid, Journal of Acta Mechanica, 186 (2006) 141-159.
- [11]. C. H. Choi, K. Johan, A. Westin, K. S. Breuer , Apparent slip flows in hydrophilic and hydrophobic microchannels, Physics of Fluid 15 (2003) 2897 - 2903.
- [12]. E. Lauga, C. Cossu, A note on the stability of slip channel flows, Physics of Fluids 17 (2005) 1 – 4.

- [13]. I. M. Eldesoky, Influence of slip condition on peristaltic transport of a compressible Maxwell fluid through porous medium in a tube, *International Journal of Applied Mathematics and Mechanics*, 8 (2012) 99 – 117.
- [14]. W. Kwang-Hua Chu, J. Fang, Peristaltic transport in a slip flow, *The European Physical Journal B*, 16 (2000) 543 – 547.
- [15]. D. A Nield, A. Bejan. *Convection in Porous Media*, Springer, 2 (1999).
- [16]. K. Vafai, *Handbook of Porous Media*, Marcel Dekker, 2 (2002).
- [17]. I. Pop, D. B. Ingham, *Convective Heat Transfer: Computational and Mathematical of Modeling Viscous Fluids and Porous Media*, Oxford, (2001).
- [18]. A. Bejan, A. D. Kraus. *Heat Transfer Handbook*, Wiley, (2003).
- [19]. S. Srinivas, R. Gayathri, M. Kothandapani, The influence of slip conditions, wall properties and heat transfer on MHD peristaltic transport, *Computer Physics Communications*, 180 (2009) 2115 – 2122.
- [20]. Kh. S. Mekheimer, T. H. AL-Arabi, Non-linear peristaltic transport of MHD flow through a porous medium., *International Journal of Mathematics and Mathematical Sciences*, 2003 (2003) 1663 – 1682.
- [21]. C. Fetecau, C. Fetecau, A new exact solution for the flow of a Maxwell fluid past an infinite plate, *International Journal of Non-Linear Mechanics*, 38 (2003) 423 – 427.
- [22]. C Fetecau, I Khan, F Ali, S Shafie, Radiation and porosity effects on the magnetohydrodynamic flow past an oscillating vertical plate with uniform heat flux, *Zeitschrift für Naturforschung A*, 67 (2012) 572 – 580.
- [23]. C. Pozrikidis, A study of peristaltic flow, *Journal of Fluid Mechanics*, 180 (1987) 515 – 527.
- [24]. H. C. Brinkman, The viscosity of concentrated suspensions and solution, *Journal of Chemistry and Physics*, 20 (1952).
- [25]. Y. Xuan, W. Roetzel Conceptions for heat transfer correlation of nanofluids, *International Journal of Heat and Mass Transfer*, 43 (2000) 3701 – 3707.
- [26]. R. L. Hamilton. O. K. Crosser, Thermal conductivity of heterogeneous two component systems, *Industrial and Engineering Chemistry Fundamentals*, 1 (1962) 187 - 191.

- [27]. A. Bejan, A study of entropy generation in fundamental convective heat transfer. *Journal of Heat Transfer*, 101 (1979) 718 – 725.
- [28]. A. Bejan, Entropy generation through heat and fluid flow. Wiley, (1994).
- [29]. R. Ellahi, M. Hassan, A. Zeeshan, Shape effects of nano size particles in Cu- H_2O nanofluid on entropy generation, *International Journal of Heat and Mass Transfer*, 81 (2015) 449 – 456.
- [30]. H. L. Agarwal, B. Anwaruddin, Peristaltic flow of blood in a branch, *Ranchi University Mathematics Journal*, 15 (1984) 111 – 121.
- [31]. A. Li, N. I. Nesterov, S. N. Malikova, V. A. Kiiatkin, The use of an impulsive magnetic field in the combined therapy of patients with stone fragments in the upper urinary tract, *Vopr. Kurortol Fizioter Lech Fiz Kult*, 3 (1994) 22 – 24.
- [32]. M. Elashahed, M. H. Harun, Peristaltic transport of Johnson-Segalman fluid under effect of a magnetic field, *Mathematical Problems in Engineering*, 2005 (2005) 663 – 677.
- [33]. V. I. Vishnyakov, K. B. Pavlov, Peristaltic flow of a conductive liquid in a transverse magnetic field., *Magnetohydrodynamics*, 8 (1972) 174 – 178.
- [34]. Kh. S. Mckheimer, Effect of the induced magnetic field on peristaltic flow of a couple stress fluid., *Physics Letters A*, 372 (2008) 4271 – 4278.
- [35]. Kh. S. Mekheimer, Peristaltic Flow of a magneto – micropolar fluid: effect of induced magnetic field, *Journal of Applied Mathematics*, 2008 (2008) 1 – 23.
- [36]. D. F. Young, Effect of a Time dependent stenosis on flow through a tube, *Journal of Engineering for Industry*, 90 (1968) 248 – 254.
- [37]. W. F. Langlois, Creeping viscous flow through a two dimensional channel of varying gap, *Proceeding Third U.S. Nat. Gong. Applied Mechanics*, 777 (1964).
- [38]. J. S. Lee, Y. C. Fung, Flow in Locally constricted tubes at low Reynolds numbers, *Journal of Applied Mechanics*, 37 (1970) 9 – 16.
- [39]. J. C. F. Chow, K. Soda, Laminar flow in tubes with constriction, *Physics of fluids*, 15 (1972) 1700 – 1706.

- [40]. B. C Chandrasekhara, N. Rudraiah, MHD flow through a channel of varying gap, *Indian Journal of Pure and Applied Mathematics*, 11 (1980) 1105 – 1123.
- [41]. G. S. Beavers, D. D. Joseph, Boundary conditions at a naturally permeable wall. 1967, *Journal of Fluid Mechanics*, 30 (1967) 197 - 207.
- [42]. S. Iijima, Helical microtubules of graphitic carbon, *Nature*, 354 (1991) 56 – 58.
- [43]. R. H. Baughman, A. A. Zakhidov, W. A. de Heer, Carbon nanotubes - the route toward applications, *Science*, 297 (2002) 787 – 792.
- [44]. M. J. O. Connell, *Carbon Nanotubes: Properties and Applications*, CRC Press, 1 (2006).
- [45]. G. D. Zhan, J. D. Kuntz, J. Wan, A. K. Mukherjee, Single-wall carbon nanotubes as attractive toughening agents in alumina-based nanocomposites, *Nature Materials*, 2 (2003) 38 – 42.
- [46]. C. H. Liu, H. Huang, Y. Wu, S. S. Fan, Thermal conductivity improvement of silicone elastomer with carbon nanotube loading, *Applied Physics Letters*, 84 (2004) 4248 – 4250.
- [47]. R. Sivakumar, S. Q. Guo, T. Nishimura, Y. Kagawa. Thermal conductivity in multi-wall carbon nanotube/silica-based nanocomposites, *Scripta Materialia*, 56 (2007) 265 – 268.
- [48]. K. Chu, Q. Wu, C. Jia, X. Liang, J. Nie, W. Tian, G. Gai, H. Guo, Fabrication and effective thermal conductivity of multi-walled carbon nanotubes reinforced Cu matrix composites for heat sink applications, *Composites Science and Technology*, 70 (2010) 298 - 304.
- [49]. H. Xie, H. Lee, W. Youn, M. Choi, Nanofluids containing multiwalled carbon nanotubes and their enhanced thermal conductivities, *Journal of Applied physics*, 94 (2003) 4967 – 4971.
- [50]. L. Chen, H. Xie, Y. Li, W. Yu, Nanofluids containing carbon nanotubes treated by mechanochemical reaction, *Thermochimica Acta*, 477 (2008) 21 – 24.
- [51]. P. Garg, J. L. Alvarado, C. Marsh, T. A. Carlson, D. A. Kessler, K. Annamalai, An experimental study on the effect of ultrasonication on viscosity and heat transfer performance of multi-wall carbon nanotube-based

- aqueous nanofluids, *International Journal of Heat and Mass Transfer*, 52 (2009) 5090 – 5101.
- [52]. T. X. Phuoc, M. Massoudi, R. H. Chen, Viscosity and thermal conductivity of nanofluids containing multi-walled carbon nanotubes stabilized by chitosan, *International Journal of Thermal Sciences*, 50 (2011) 12 – 18.
- [53]. S. U. S. Choi, Z. G. Zang, W. Yu, F. E. Lookwood, E. A. Grulke, Anomalous thermal conductivity enhancement in nanotube suspensions, *Applied Physics Letters*, 79 (2001) 2252 – 2254.
- [54]. B. C. Pak, Y. I. Cho, Hydrodynamic and heat transfer study of dispersed fluids with submicron metallic oxide particles, *Experimental Heat Transfer*, 11(1998) 151 – 170.
- [55]. C. J. Ho, W. K. Liu, Y. S. Chang, C. C. Lin, Natural convection heat transfer of alumina–water nanofluid in vertical square enclosures: an experimental study, *International Journal of Thermal Sciences*, 49 (2010) 1345 – 1353.
- [56]. S. Q. Zhou, R. Ni, Measurement of the specific heat capacity of water-based nanofluid, *Applied Physics Letters*, 92 (2008) 1 – 3.
- [57]. K. Khanafer, K. Vafai, A critical synthesis of thermophysical characteristics of nanofluids, *International Journal of Heat and Mass Transfer*, 54 (2011) 4410 – 4428.
- [58]. S. Halefadi, P. Estelle, B. Aladag, N. Doner, T. Mare, Viscosity of carbon nanotubes water based nanofluids: Influence of concentration and temperature, *International Journal of Thermal Sciences*, 71 (2013) 111 – 117.
- [59]. V. Y. Rudyak, Viscosity of nanofluids-Why it is not described by the classical theories, *Advances in Nanoparticles*, 2 (2013) 266 – 279.
- [60]. N. Jamshidi, M. Farhadi, D. D. Ganji, K. Sedighi, Experimental Investigation on the viscosity of nanofluids, *International Journal of Engineering*, 25 (2012) 201 – 209.
- [61]. Einstein, Albert. *Investigations on the Theory of the Brownian Movement*, Dover Publications, (1956).
- [62]. H. C. Brinkman, The viscosity of concentrated suspensions and solutions., *Journal of Chemical Physics*, 20 (1952) 571 – 581.
- [63]. G. Batchelor, The effect of Brownian motion on the bulk stress in a suspension of spherical particles, *Journal of Fluid Mechanics*, 83 (1977) 97 – 117.

- [64]. H. Brenner, D. W. Condiff, Transport mechanics in systems of orientable particles, Convective transport, *Journal of Colloid and Interface Science*, 47 (1974) 199 - 264.
- [65]. M. Kole, D. Tripathi, T. K. Dey, Percolation based enhancement in effective thermal conductivity of HDPE/LBSMO composites, *Bulletin of Materials Science*, 35 (2012) 601 - 609.
- [66]. J. A. Eastman, S. U. S. Choi, L. J. Thompson, S. Lee, Anomalously increasing effective thermal conductivities of ethylene glycol-based nanofluids containing copper nanoparticles, *Applied Physics Letters*, 78 (2001) 718 - 720.
- [67]. J. Garg, B. Poudel, M. Chiesa, J. B. Gordon, J. J. Ma, J. B. Wang, Z. F. Ren, Y. T. Kang, H. Ohtani, J. Nanda, G. H. McKinley, G. Chen, Enhanced thermal conductivity and viscosity of copper nanoparticles in ethylene glycol nanofluid., *Journal of Applied Physics*, 103 (2008) 743011 - 743016.
- [68]. J. C. Maxwell, *A Treatise on Electricity and Magnetism*, Clarendon Press, 1 (1873).
- [69]. J. Koo, C. Kleinstreuer, A new thermal conductivity model for nanofluids, *Journal of Nanoparticle Research*, 6 (2004) 577 - 588.
- [70]. J. Koo, C. Kleinstreuer, Laminar nanofluid flow in microheat-sinks , *International Journal of Heat and Mass Transfer*, 48 (2005) 2652 - 2661.
- [71]. B. Ghasemi, S. M. Aminossadati, Brownian motion of nanoparticles in a triangular enclosure with natural convection, *International Journal of Thermal Sciences*, 49 (2010) 931 - 940.
- [72]. M. Corcione, Rayleigh-Bénard convection heat transfer in nanoparticle suspensions, *International Journal of Heat and Fluid Flow*, 32 (2011) 65 - 77.
- [73]. C. H. Chon, K. D. Kihm, S. P. Lee, S. U. S. Choi, empirical correlation finding the role of temperature and particle size for nanofluid (Al_2O_3) thermal conductivity enhancement, *Applied Physics Letter*, 87 (2005) 153107.
- [74]. N. Wakao, S. Kaguei, *Heat and Mass Transfer in Packed Beds*, Gordon and Breach Science Publishers, New York, U.S.A., (1982) 175 - 205.

- [75]. W. Yu, S.U.S. Choi, The role of interfacial layers in the enhanced thermal conductivity of nanofluids: A renovated Hamilton – Crosser model, *Journal of Nanoparticle Research*, 6 (2004) 355 – 361.
- [76]. R. R. Bilboul, A note on the permittivity of a double layer ellipsoid. *British Journal of Applied Physics*, 2 (1969) 921 – 923.
- [77]. L. D. Landau, E. M. Lifshitz, L. P. Pitaevskii, *Electrodynamics of Continuous Media*, 2nd edition. Butterworth- Heinenann Ltd, Oxford, Great Britain (1984).
- [78]. Y. Zhao, S. Liao, HAM-based package BVPh 2.0 for nonlinear boundary value problems, in: S. Liao (Ed.), *Advances in Homotopy Analysis Method*, World Scientific Press, (2013).
- [79]. R. W. Fox, A. T. McDonald, P. J. Pritchard, *Introduction to Fluid Mechanics*, John Wiley & Sons, 2004.
- [80]. L. Godson, B. Raja, D. Mohan Lal, L. Wongwises, Experimental Investigation on the Thermal Conductivity and Viscosity of Silver-Deionized Water Nanofluid, *Experimental Heat Transfer*, 23 (2010) 317 – 332.

Nomenclature

M^*	Mass	V^*	Volume
u, v, w	Velocity components	k	Thermal conductivity
x, y, z	Cartesian coordinates	C_p	Specific heat
\mathbf{V}	Velocity	K	Porosity parameter
a_1, b_1	Wave amplitude	c_1	Wave speed
t	Time	B_0	Magnetic field strength
D	Fractal index	M^{**}	Molecular weight
C^*	Empirical constant	Pr^*	Specific Prandtl number
Re^*	Specific Reynolds number	\tilde{a}, \tilde{b} and \tilde{c}	Semixis directions of CNTs
d_s	Diameter of nanoparticles	k_d	Thermal conductivity due to thermal dispersion
N	Heat flux parameter	B_c	Bejan number
h_{layer}	Nanolayer thickness	p	Pressure
K_1	Permeability	Nu	Nusselt number
Br	Brinkman number	S_G	Entropy generation per unit length
r^*	Nanoparticles volume ratio	T	Fluid temperature
Pr	Prandtl number	n^*	Shape factor
R_m	Magnetic Reynolds number	S_1	Stommer's number
Q	Volume flow rate	Q_0'	Time-average flux
Q_0	Heat generated / absorbed	l_f	Mean free path
q	Radioactive heat flux	N^*	Avogadro number
Ec	Eckert number	h_{layer}^*	Nanolayer thickness
Gr	Grashof number	A_1^*	Intrinsic viscosity

d_f	Fractal dimensions	d_c	Chemical dimensions
g	Gravitational acceleration vector	A_2^*	Huggins' coefficient
Re	Reynolds number	R_p	Particle radius
a_a	Aggregate nanoparticles radius	k^*	Mean absorption coefficient
a^*	Primary nanoparticles radius	A_1	Rivlin Ericksen tensor.
$\mathcal{L}_i, i = 1, 2$	Linear operators	$C_i, i = 1, \dots, 54$	Constants
M	Hartmann number	\dot{K}	Boltzmann constant

Greek symbols

ρ	Density	ξ	Magnetic diffusivity
γ_1	function of the volume fraction	ϕ	Volume fraction
μ	Viscosity	σ	Electric conductivity
ω	Phase difference	δ	Dimensionless wave number
ν	Kinematic viscosity	β^*	Thermal expansion coefficient
α_{nf}	thermal diffusivity of nanofluid	Ψ	Stream function
θ	Dimensionless temperature	Λ	Dimensionless temperature difference
Φ^*	Dissipation function	σ^*	Stefan-Boltzmann constant
β_1^*	Ratio of the nanolayer thickness to particle radius	β	Slip parameter
λ	Wave length	Ψ	Sphericity
γ	Thermal slip parameter	ϕ_a	Effective volume fraction
δ	Dimensionless wave number		

Subscripts

nf	Nanofluid	f	Base fluid
------	-----------	-----	------------

<i>s</i>	Solid particle	<i>layer</i>	Nanolayer
<i>int</i>	Cluster	<i>a</i>	Aggregation
<i>max</i>	Maximum	<i>env</i>	Environment